UNIVERSITY OF JYVÄSKYLÄ
DEPARTMENT OF PHYSICS

PRO GRADU THESIS

NONLINEAR DYNAMICS AND CHAOS IN CLASSICAL COULOMB-INTERACTING MANY-BODY BILLIARDS

Janne Samuli Solanpää

July 29, 2013

Supervisor: Prof. Esa Räsänen
Tampere University of Technology

Abstract

Chaos and nonlinear dynamics of single-particle Hamiltonian systems have been extensively studied in the past; however, less is known about interacting many-body systems in this respect even though *all* physical systems include particle-particle interactions in one way or another. To study Hamiltonian chaos, two-dimensional billiards are usually employed, and due to the realization of billiards in semiconductor quantum dots, the electrostatic Coulomb interaction is the natural choice for the interparticle interaction. Yet, surprisingly little is known about chaos and nonlinear dynamics of Coulomb-interacting many-body billiards.

To address the challenging problems of interacting many-body billiards, we have developed a flexible and expandable code implementing methods previously used in molecular dynamics simulations. The code is *generic* in sense that it is readily applicable to most two-dimensional billiards – including periodic systems – with different types of interparticle interactions. In this work, insights into Coulomb-interacting billiards are gained by applying the methods to two relevant systems: a two-particle circular billiards and a few-particle diffusion, the latter of which is studied only as a closed system. Also general implications of the results for other systems are discussed.

The circular billiards is studied with the interaction strength varying from the weak to the strong-interaction limit. Bouncing maps show quasi-regular features in the weak and strong-interacting limits. In the strong-interaction regime an analytical model for the phase space trajectory is derived, and the model is found to agree with the simulated data. At intermediate interaction strengths the bouncing maps get filled.

To obtain a quantitative view on the hyperbolicity and stickiness of the circular billiards, we calculate escape-time distributions of open circular billiards. At weak interactions the escape-time distributions show a power-law tail owing to the quasi-regular dynamics arising from the integrable non-interacting limit. At intermediate interaction strengths the distributions are exponential implying hyperbolicity within the studied time-scales.

As the second application, the diffusion process between two square containers connected by a short channel is studied under a homogeneous magnetic field perpendicular to the table. During the propagation, over half of the particles – all initially in the same container – travel from one container to the other. The time this process takes is defined here as the relaxation time.

The average relaxation times $\langle t_{\text{rel}} \rangle$ are calculated as a function of the effective Larmor radius r_{ELR}, which describes the average effect of the magnetic field on the particles. The behavior of the r_{ELR}-$\langle t_{\text{rel}} \rangle$ graphs is studied thoroughly for different interaction strengths and channel widths. Interestingly, the graphs show a universal minimum for all interaction strengths, and in the weak-interaction limit also other extrema appear. The new extrema in the weak-interaction limit are explained by calculating properties of open single-particle magnetic square billiards for different Larmor radii.

Tiivistelmä

Hamiltonisten yksihiukkasjärjestelmien kaoottisuus ja dynaaminen epälineaarisuus tunnetaan suhteellisen hyvin. Vuorovaikuttavien monihiukkasjärjestelmien kaoottisuus puolestaan tunnetaan suhteellisen heikosti, vaikka kaikki fysikaaliset järjestelmät ovat tavalla tai toisella vuorovaikuttavia. Hamiltonisen kaaoksen tutkimiseen käytetään tyypillisesti biljardijärjestelmiä. Biljardeissa sähköstaattinen Coulomb-vuorovaikutus on luonnollinen valinta hiukkasten väliselle vuorovaikutukselle, sillä biljardit toimivat myös malleina kokeellisesti toteutettaville puolijohdekvanttipisteille. Kuitenkin erityisesti Coulomb-vuorovaikuttavien biljardien kaoottisuus tunnetaan yllättävän huonosti.

Päästäksemme käsiksi vuorovaikuttavien monihiukkasjärjestelmien haastaviin kaaosongelmiin kehitimme joustavan ja laajennettavan laskentakoodin, joka käyttää aiemmin molekyylidynamiikan simuloinnissa käytettyjä menetelmiä. Koodi on yleispätevä siinä mielessä, että sitä voi käyttää suoraan useimpien biljardijärjestelmien – mukaanlukien periodisten järjestelmien – simulointiin erilaisilla hiukkasten välisillä vuorovaikutuksilla. Menetelmiä sovellettiin kahteen kaaostutkimuksen kannalta oleelliseen järjestelmään: kahden hiukkasen ympyräbiljardiin ja muutaman hiukkasen diffuusioon suljetussa järjestelmässä. Tuloksilla saatiin uutta tietoa Coulomb-vuorovaikuttavien järjestelmien kaoottisuudesta ja dynamiikasta. Lisäksi työssä arvioitiin tuloksista saatujen johtopäätösten soveltuvuutta muihin järjestelmiin.

Ympyräbiljardia tutkittiin eri vuorovaikutusvoimakkuuksilla heikon vuorovaikutuksen rajalta vahvan vuorovaikutuksen rajalle. Törmäyskartoissa nähtiin näennäisesti säännöllisiä rakenteita sekä heikoilla että vahvoilla vuorovaikutuksilla. Lisäksi vahvasti vuorovaikuttavan järjestelmän faasiavaruusradoille johdettiin analyyttinen malli, joka täsmäsi numeerisesti laskettujen ratojen kanssa. Keskivahvoilla vuorovaikutuksilla törmäyskartat täyttyivät.

Ympyräbiljardin hyperbolisuuden ja tahmaisuuden kvantitatiiviseen tutkimiseen käytettiin avointa ympyräbiljardia, jonka pakoaikajakaumia laskettiin eri vuorovaikutusvoimakkuuksille. Heikon vuorovaikutuksen rajalla pakoaikajakaumat noudattivat asymptoottisesti potenssilakia, mikä johtui näennäisesti säännöllisistä radoista pienillä vuorovaikutusvoimakkuuksilla. Keskivahvoilla vuorovaikutusvoimakkuuksilla jakaumat olivat eksponentiaalisia, mihin perustuen järjestelmän pääteltiin olevan hyperbolinen tutkitulla aikaskaalalla.

Toinen tutkittava ilmiö oli muutaman hiukkasen diffuusioprosessi kahden kanavalla yhdistetyn neliösäiliön välillä magneettikentässä. Aluksi hiukkaset olivat samassa säiliössä, mutta ajan kuluessa ne liikkuivat kohti tilannetta, jossa yli puolet hiukkasista oli siirtynyt toiseen säiliöön. Prosessiin kuluva aika nimettiin relaksaatioajaksi.

Relaksaatioaikojen ensemble-keskiarvot $\langle t_{rel} \rangle$ laskettiin hiukkasten tehollisen syklotronisäteen r_{ELR} (magneettikentän keskimääräinen vaikutus hiukkasten ratoihin) funktiona useille eri vuorovaikutusvoimakkuuksille ja kanavan leveyksille. r_{ELR}-$\langle t_{rel} \rangle$-kuvaajissa havaittiin universaali minimi kaikille vuorovaikutusvoimakkuuksille. Lisäksi heikon vuorovaikutuksen rajalla r_{ELR}-$\langle t_{rel} \rangle$-kuvaajiin ilmestyi myös

muita ääriarvoja, jotka selitettiin laskemalla avoimen magneettisen neliöbiljardin ominaisuuksia eri syklotronisäteille.

v

Acknowledgements

Contents

List of Figures

X

1 Introduction

1.1 Towards many-body billiards

Chaos is a phenomenon where *deterministic* systems – even simple ones – exhibit complex dynamics that appear *random* from all practical points of view [1–3]. The random-like behavior is the result of predictability of chaotic systems being inherently unstable to any uncertainty in our knowledge of the current state of the system. In practice we never know the current state precisely, and hence the long-term evolution seems random.

There are several different phenomena grouped under chaos theory. What distinguishes chaos from other physical theories is its universality: the same phenomena can be found in several systems throughout nature and different sciences including, e.g., nonlinear differential equations, electrical circuits, chemical reactions, and biological systems [1–10].

Chaos is also inherently included in classical mechanics, especially in Hamiltonian mechanics [1,3,5,11]. Hamiltonian chaos is usually studied within two-dimensional billiards, where a point particle moves typically in a straight line or a circular arc between elastic collisions with the boundary. Popularity of billiards is due to easy visualization combined with their ability to produce the chaotic phenomena found in Hamiltonian systems. Furthermore, billiards are the easiest route to study correspondence between classical and quantum chaos.

Instead of being only mathematical idealizations, nanoscale billiards can also be manufactured in experiments by confining electrons in semiconductor quantum dots and quantum point contacts [12, 13], where the electron motion can be made ballistic, i.e., fully determined by the confining potential [13]. In these structures, the number of electrons can be controlled precisely, and the confining potential can be made extremely steep so that hard wall billiards form natural models for them [14]. Furthermore, even though the systems are inherently quantum mechanical, it is possible – at least in theory – to produce billiards where classically explainable phenomena can be observed before quantum mechanical effects become important [15].

Single-particle billiards have been extensively studied with varying shapes of billiard tables ranging from simple rectangles to, e.g., fractal-like *honey mushrooms*,[1] where one takes a mushroom-shaped billiard table and attaches yet another mushroom to its foot and so on [16]. Also open single-particle billiards, where the particle can escape the system through a hole, have been addressed in, e.g., mushroom [17], stadium [18], drivebelt [19], and circular billiards [20].

Interacting many-body billiards, however, have attracted less attention even though all physical systems are interacting in one way or another. Two-particle billiards have been studied with hard-sphere interactions in two dimensions [21–23] and with Yukawa interactions in both one-dimensional [24–26] and two-dimensional

---

[1]Honey mushrooms are fractals only in the limit where the described process is repeated infinitely many times.

systems [27, 28]. Due to the realization of billiards in confined semiconductor structures [12, 29, 30], the natural choice for the interaction would, however, be the Coulomb interaction [31, 32]. Most studies on Coulomb-interacting billiards have been restricted to soft potentials [33–37], but also periodic systems have been addressed [38–40]. In addition, some studies on Yukawa-interacting billiards have also included a few remarks in the Coulombic limit for one-dimensional [24–26] and two-dimensional systems [28]. Recently, also the Coulomb-interacting two-particle rectangular billiards in magnetic fields has been studied [41]. For a more detailed review on these recent advances in many-body billiards, see Sec. 3.7.

To study chaos and nonlinear dynamics of Coulomb-interacting billiards, we have developed a flexible and extensible C++ code that implements methods previously used in molecular dynamics simulations. The author of this thesis wishes to acknowledge Perttu Luukko for significant initial development of the code. The code is *generic* in sense that it is readily applicable to most billiard systems from one to a few hundred particles with varying interaction types. In this thesis we detail the methods and the implementation of our code and apply it to two systems relevant to the study of Coulomb-interacting billiards. The results give novel insights into the effects of the Coulomb interaction in billiards in general, not just in these systems.

First, we study the Coulomb-interacting two-particle circular billiards with the focus on its chaotic properties for different interaction strengths. The circular table was chosen since

- it is geometrically simple, and thus the effects of the Coulomb-interaction are easier to interpret,

- the single-particle limit of the system is well known [42], and

- the circular table represents a simple model for two-dimensional quantum dots.

Chaoticity of the system is addressed by calculating bouncing maps of closed circular billiards and escape-time distributions of open circular billiards.

Our second study is about a few-particle diffusion process in a two-container billiard table in a magnetic field. The choice of the system draws motivation from quantum-Hall devices, especially from quantum point contacts [43] and their classical limit. We focus on the behavior of average relaxation times as a function of the magnetic field, but also open single-particle magnetic square billiards is studied to explain the behavior of average relaxation times at weak interactions.

This thesis is organized as follows. In Sec. 1.2, we further illustrate the meaning of chaos with several examples. The theoretical framework of the Hamiltonian formalism is introduced in Sec. 2. In Sec. 3, we give a brief introduction to chaos in closed and open Hamiltonian systems. Section 4 details the numerical methods. The results on the circular billiards are given in Sec. 5.1 and the results on the diffusion process in Sec. 5.2. Summaries of the results are presented in Secs. 5.1.5 and 5.2.5. Finally, in Sec. 6, we conclude this thesis with a discussion and outlook.

1.2 What is chaos?

Intuitively, chaos is imagined as unpredictable, random-like behavior. There is no strict definition of *chaos*, but we think the following extract captures the essentials.

> *Chaos is aperiodic long-term behavior in a deterministic system*
> *that exhibits sensitive dependence on initial conditions.*
>
> — Strogatz [1]

According the the above definition, in order for motion to be considered chaotic it needs to satisfy the following criteria:

- Aperiodicity. This is a natural requirement in the sense that periodic movement would imply predictability of trajectories.

- Determinism. The unpredictability must arise not from randomness of time evolution as in stochastic processes but from some other dynamical reason.

- Sensitive dependence on initial conditions. The dynamical structure of chaotic systems results in exponential separation of two initially nearby trajectories. This idea is used when we introduce a quantitative measure for chaos in Sec. 3.1.

Chaotic behavior is schematically visualized in Fig. 1, where two initially (t_0) nearby orbits start to separate and at some time t_λ, the separation blows up exponentially. To further familiarize the reader with the concept of chaoticity, we briefly review a few classic examples of chaotic systems in the following.

The motion of a regular pendulum, a stiff massless rod with a weight attached to one end and a rotating axis to the other end, is governed in the small angle approximation by the ordinary differential equation (ODE)

$$\frac{d^2\theta}{dt^2} = -\omega^2\theta, \tag{1.1}$$

where θ is the angle from the equilibrium position and ω is the angular velocity determined by the system parameters. This ODE can be solved analytically to

t_λ: Exponential
separation visible

t_0: Two initially
nearby orbits
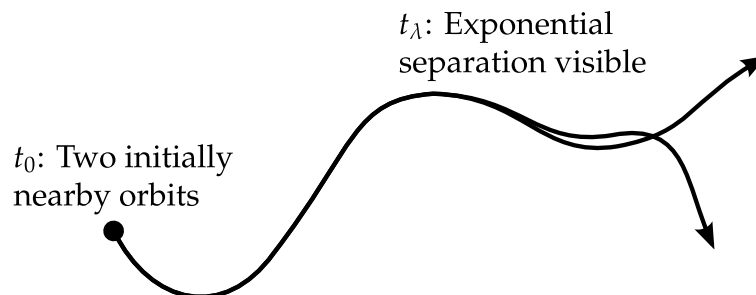
Figure 1: Chaoticity is seen as exponential separation of initially nearby orbits.
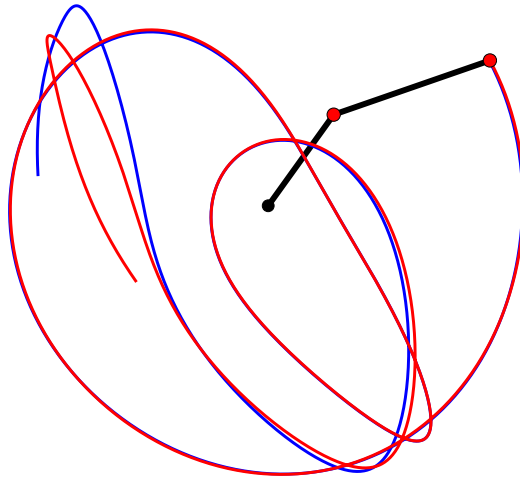
Figure 2: Two trajectories of the far end of the double pendulum. The trajectories are initially close in phase space (i.e., nearly same positions and velocities of the rods) but diverge fast away from each other. This is characteristic behavior for chaotic systems.
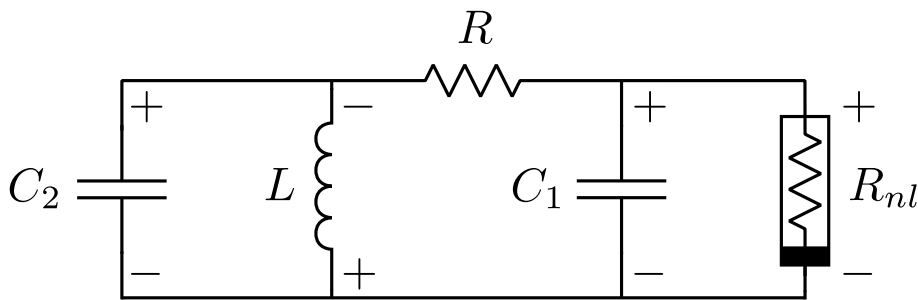
Figure 3: Circuit diagram of Chua's circuit.[2]

obtain the solution $\theta = \theta_{\max} \sin(\omega t + \phi)$. The system is regular (not chaotic) in sense that all perturbations to initial conditions result in only slight changes in the system trajectory. Also the nonlinear pendulum, i.e., without the small angle approximation, is regular, but numerical methods would be required to demonstrate this.

The idea of the pendulum can be extended to the double pendulum, where there is yet another rod attached to the end of the first rod (with a weight). The double pendulum exhibits chaotic motion as shown in Fig. 2, where two initially close positions of rods diverge after a short period of time.

Also chemical reactions can exhibit chaotic behavior as demonstrated by the Belousov-Zhabotinsky reaction [6,7]. The reaction takes place, for example, in a mixture of $KBrO_3$, $Ce(SO_4)_2$, $CH_2(COOH)_2$, H_2SO_4, and water [44]. In the solution, a series of chemical reactions occur causing the catalysts of the reactions, Ce ions, to oscillate between two states, Ce^{4+} and Ce^{3+} [8]. In essence, the relative

---

[2]Figures of components from Wikimedia Commons. User Eadthem is to be attributed for the inductor symbol.

4
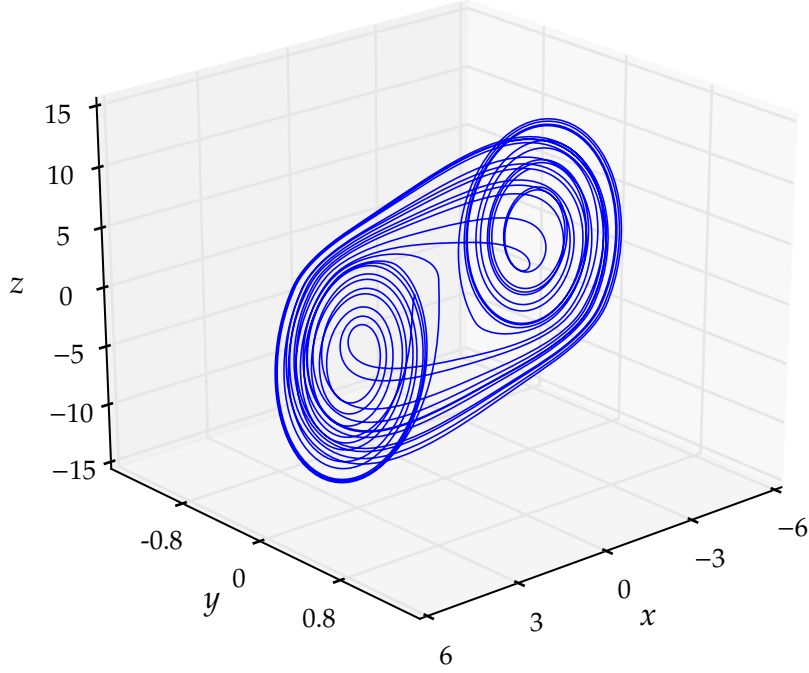
Figure 4: One trajectory of Chua's circuit with parameters $a = 15.6$, $b = 28$, $m_0 = -1.143$, and $m_1 = -0.714$ [see Eqs. (1.2) – (1.4)]. The trajectory reveals the strange attractor of Chua's circuit.

concentration of these two ions oscillates in a chaotic fashion. The oscillation can also be seen with bare eyes since Ce^{4+} gives the solution a yellowish color and Ce^{3+} is colorless [45].

Chaos can also be seen and, more importantly, measured in some electrical circuits such as Chua's circuit shown in Fig. 3. The essential part of Chua's circuit and the cause of the chaotic behavior is the nonlinear resistor R_{nl} [9]. The system can be described by the (dimensionless) coupled differential equations [10]

$$\frac{dx}{dt} = \alpha \left[y - x - f(x) \right] \tag{1.2}$$

$$\frac{dy}{dt} = x - y + z \tag{1.3}$$

$$\frac{dz}{dt} = -\beta y, \tag{1.4}$$

where α and β are system parameters and $f(x) = m_1 x + (m_0 - m_1)(|x + 1| - |x - 1|)$ describes the electric response of the nonlinear resistor with parameters m_0 and m_1. The variables x, y, and z essentially describe the voltages across the capacitors C_1 and C_2, and the current in the inductor L_1, respectively [9]. The circuit demonstrates chaotic oscillating behavior in the variables, and when visualizing the system trajectory in xyz-coordinates as in Fig. 4, the plot reveals the strange attractor of Chua's circuit [9].

As last example, we introduce perhaps the best known chaotic system, the Lorenz
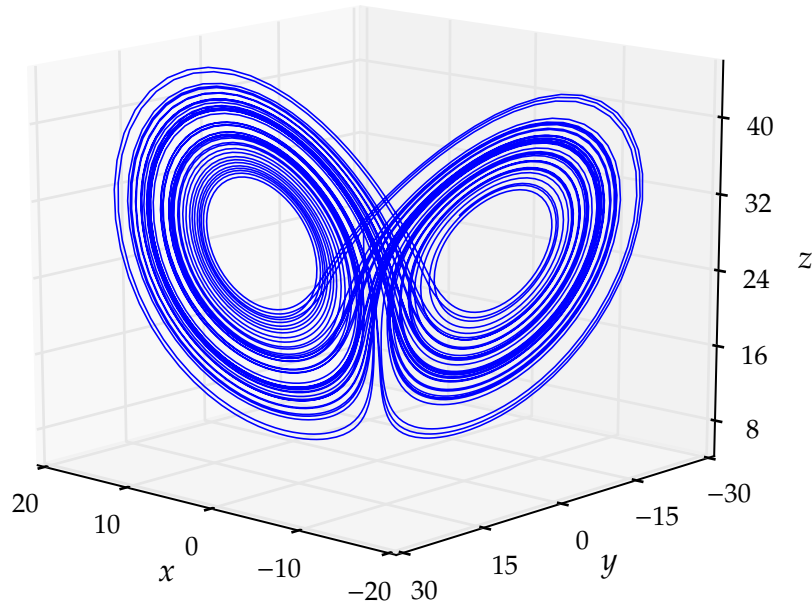
Figure 5: One trajectory of the Lorenz system with parameters $\rho = 28$, $\sigma = 10$, and $\beta = 8/3$ [see Eqs. (1.5) – (1.7)]. The trajectory draws the pattern of the strange attractor, which is often called the Lorenz butterfly [1].

system, which was originally invented to describe convection in the atmosphere [46]. The system can be described by the coupled differential equations [46]

$$\frac{dx}{dt} = \sigma y - \sigma x \tag{1.5}$$

$$\frac{dy}{dt} = \rho x - xz - y \tag{1.6}$$

$$\frac{dz}{dt} = xy - \beta z, \tag{1.7}$$

where ρ, σ, and β are system parameters. At certain parameter ranges the Lorenz system has a strange attractor,[3] also called the Lorenz Butterfly, which is shown in Fig. 5. As Lorenz correctly observed from his model [4], weather can not be predicted far in the future due to sensitive dependence on initial conditions.

One can already see from the previous examples that even very simple systems might exhibit chaotic motion, not to speak of more complex dynamical systems. This emphasizes how chaos is a fundamental part of natural phenomena.

---

[3]Strictly speaking, the Lorenz attractor has not been proven to be a strange attractor despite numerous attempts.

2 Hamiltonian systems

2.1 Principle of stationary action and Lagrangian formalism

The most conventional way to describe classical mechanics is via Newton's laws of motion. However, if the system has constraints, the Lagrangian formulation often turns out to be more useful in practice. In the Lagrangian formulation the constraints are incorporated either by using the Lagrange multipliers or by a transformation to a new set of coordinates called the *generalized coordinates*, which take the constraints into account.

Suppose that our system is d-dimensional and has k particles. This means that the positions of the particles can be described by vectors $r_1, \ldots, r_k$ of a d-dimensional Euclidean space $\mathbb{R}^d$. If there exists p holonomic constraints $f_i(\{r_i\}, t) = 0$ on the system, the number of coordinates needed to describe the configuration space is reduced to $kd - p$ [47]. We can then describe the system with just $N = kd - p$ *generalized coordinates* q^a in such a way that

$$r_1 = r_1(\{q^a\})$$
$$\vdots \tag{2.1}$$
$$r_N = r_N(\{q^a\}).$$

From now on we denote the set of generalized coordinates $\{q^1, \ldots, q^N\}$ by just q^a and similarly for other variables. It will be clear from the context whether by q^a we mean the set of coordinates or just one of them. Also, to shorten the notation, we will often use the notation $\dot{f}$ to denote the time derivative of a function f.

The basic idea behind the Lagrangian formulation, in addition to the use of generalized coordinates, is to introduce the *action* functional

$$S\left[q^a(t)\right] = \int_{t_A}^{t_B} L\left[q^a(t), \dot{q}^a(t), t\right] dt, \tag{2.2}$$

where $L\left(q^a(t), \dot{q}^a(t), t\right)$ is the *Lagrangian* (function) and the integral is taken over some path $\{q^1(t), \ldots, q^N(t)\} \doteq q^a(t)$. Later we will deduce the form of the Lagrangian.

The Hamilton's principle is the cornerstone of the Lagrangian formulation. It postulates that the path $q^a(t)$ the system follows is the one for which the action S is stationary,[4] i.e.,

$$0 = \delta S = \int_{t_A}^{t_B} \left(\frac{\partial L}{\partial q^a} \delta q^a + \frac{\partial L}{\partial \dot{q}^a} \delta \dot{q}^a \right) dt. \tag{2.3}$$

Here we begin to use the Einstein summation convention, i.e., if the same index

---

[4]The original idea was formulated by Pierre-Louis de Maupertuis [48, 49] despite Sir William Rowan Hamilton often being credited for the idea.

appears in a term twice,[5] it is understood that we sum over that index (from 1 to N). We proceed by integration by parts and use $\delta \dot{q}^a = \frac{d}{dt}\delta q^a$ to obtain

$$0 = \delta S = \int_{t_A}^{t_B} \left[\frac{\partial L}{\partial q^a}\delta q^a - \frac{d}{dt}\left(\frac{\partial L}{\partial \dot{q}^a}\right)\delta q^a \right] dt + \left. \frac{\partial L}{\partial \dot{q}^a}\delta q^a \right|_{t_A}^{t_B}. \tag{2.4}$$

With fixed endpoints $\delta q^a(t_A) = \delta q^a(t_B) = 0$, the substitution term goes to zero, and we get

$$0 = \delta S = \int_{t_A}^{t_B} \left[\frac{\partial L}{\partial q^a} - \frac{d}{dt}\left(\frac{\partial L}{\partial \dot{q}^a}\right) \right]\delta q^a \, dt. \tag{2.5}$$

The stationarity requirement must hold for all perturbations $\delta q^a(t)$, and therefore, we get the *Euler-Lagrange* equations

$$\frac{\partial L}{\partial q^a} - \frac{d}{dt}\left(\frac{\partial L}{\partial \dot{q}^a}\right) = 0 \; \forall a = 1,\dots,N. \tag{2.6}$$

Should one wonder why there are no Lagrange multipliers here, we remind that the constraints have already been incorporated in the generalized coordinates.

All we need to do now is to connect the Euler-Lagrange equations to the Newtonian mechanics so that they yield the same results. To do this, we require that Newton's second law is obeyed. For simplicity, we do this only in a single-particle case with $\{q^a\} = \{r^1, r^2, r^3\}$. Newton's second law with external potential $V(\boldsymbol{r}, t)$ yields then

$$m\ddot{\boldsymbol{r}} = -\nabla V(\boldsymbol{r}, t) \tag{2.7}$$

$$\Leftrightarrow \frac{d}{dt}(m\dot{r}^a) = -\frac{\partial}{\partial r^a}V(\boldsymbol{r}, t) \tag{2.8}$$

$$\Leftrightarrow \frac{d}{dt}\left[\frac{\partial}{\partial \dot{r}^a}\left(\frac{m}{2}\dot{r}^{a2}\right)\right] = \frac{\partial}{\partial r^a}[-V(\boldsymbol{r}, t)]. \tag{2.9}$$

If we compare this with the Euler-Lagrange equations (2.6), we see that they are equivalent if

$$\frac{\partial L}{\partial \dot{r}^a} = \frac{\partial}{\partial \dot{r}^a}\left(\frac{m}{2}\dot{r}^{a2}\right) \tag{2.10}$$

and

$$\frac{\partial L}{\partial r^a} = \frac{\partial}{\partial r^a}[-V(\boldsymbol{r}, t)]. \tag{2.11}$$

From these relations we conclude that the form of the Lagrangian should be (up to a constant)

$$L = \frac{m}{2}\|\dot{\boldsymbol{r}}\|^2 - V(\boldsymbol{r}, t) = T - V, \tag{2.12}$$

where T is the kinetic energy of the system and V the potential energy. This form

---

[5]Once in a co index (lower index) and once in a contra index (upper index).

of the Lagrangian, $L = T - V$, is completely general [47] although we only deduced it for a simple unconstrained system.

2.2 Hamiltonian formalism

To go even further, we next reformulate the Lagrangian mechanics by doing a Legendre transformation $\{q^a, \dot{q}^a, t\} \rightarrow \{q^a, p_a, t\}$. First, we define the generalized momenta

$$p_a = \frac{\partial L}{\partial \dot{q}^a} \tag{2.13}$$

and the *Hamiltonian* (function)

$$H(q^a, p_a, t) = \dot{q}^a p_a - L. \tag{2.14}$$

To get the Hamiltonian equations of motion, we look at the differential of the Hamiltonian,

$$dH = \frac{\partial H}{\partial p_a} dp_a + \frac{\partial H}{\partial q^a} dq^a + \frac{\partial H}{\partial t} dt. \tag{2.15}$$

On the other hand, the definition of the Hamiltonian in Eq. (2.14) gives

$$
\begin{aligned}
dH &= \dot{q}^a dp_a + p_a d\dot{q}^a - dL \\
&= \dot{q}^a dp_a + \frac{\partial L}{\partial \dot{q}^a} d\dot{q}^a - \frac{\partial L}{\partial \dot{q}^a} d\dot{q}^a - \frac{\partial L}{\partial q^a} dq^a - \frac{\partial L}{\partial t} dt \\
&= \dot{q}^a dp_a - \frac{\partial L}{\partial q^a} dq^a - \frac{\partial L}{\partial t} dt.
\end{aligned} \tag{2.16}
$$

By comparing Eqs. (2.15) and (2.16), we get the Hamiltonian equations of motion (HEOM)

$$\dot{q}^a = \frac{\partial H}{\partial p_a} \tag{2.17}$$

and

$$\frac{\partial H}{\partial q^a} = -\frac{\partial L}{\partial q^a} \stackrel{(2.6)\ \&\ (2.13)}{=} -\dot{p}_a. \tag{2.18}$$

Also note that

$$
\begin{aligned}
\frac{dH}{dt} &= \frac{\partial H}{\partial q^a} \dot{q}^a + \frac{\partial H}{\partial p_a} \dot{p}^a + \frac{\partial H}{\partial t} \\
&\stackrel{(2.17)\ \&\ (2.18)}{=} \frac{\partial H}{\partial q^a} \frac{\partial H}{\partial p_a} - \frac{\partial H}{\partial p_a} \frac{\partial H}{\partial q^a} + \frac{\partial H}{\partial t} = \frac{\partial H}{\partial t},
\end{aligned} \tag{2.19}
$$

which gives – together with Eqs. (2.15) and (2.16) – the last of the Hamiltonian equations of motion,

$$\frac{dH}{dt} = -\frac{\partial L}{\partial t}. \tag{2.20}$$

In the Hamiltonian formalism we work in the phase space $(q^a, p_a) \in \mathbb{P}$ rather than in the configuration space as in the Lagrangian formalism. This means that q^a and p_a are treated on equal footing. Furthermore, one could wonder if it is possible to develop a variational principle in the phase space.

To find the variational principle, remember that we defined the Hamiltonian as the Legendre transformation of the Lagrangian,

$$H(q^a, p_a, t) = \dot{q}^a p_a - L.$$

This can be inverted to get L in terms of the phase space variables. By using the obtained Lagrangian, the action integral in Eq. (2.2) becomes

$$S = \int_{t_A}^{t_B} \left[\dot{q}^a p_a - H(q^a, p_a, t) \right] dt. \tag{2.21}$$

By requiring S to be stationary on the phase-space path $(q^a(t), p_a(t))$, we get a variational equation

$$0 = \delta S = \int_{t_A}^{t_B} \left(p_a \delta \dot{q}^a + \dot{q}^a \delta p_a - \frac{\partial H}{\partial q^a} \delta q^a - \frac{\partial H}{\partial p_a} \delta p_a \right) dt. \tag{2.22}$$

As before, we use $\delta \dot{q}^a = \frac{d}{dt} \delta q^a$ and integrate the first term of the integrand by parts to get

$$0 = \delta S = \int_{t_A}^{t_B} \left(-\dot{p}_a \delta q^a + \dot{q}^a \delta p_a - \frac{\partial H}{\partial q^a} \delta q^a - \frac{\partial H}{\partial p_a} \delta p_a \right) dt + \left. p_a \delta q^a \right|_{t_A}^{t_B}. \tag{2.23}$$

By fixing the end points $q^a(t_A)$ and $q^a(t_B)$, the substitution term vanishes, and since the variations in q^a and p_a are independent and arbitrary, they must vanish independently. As a result we get the Hamiltonian equations of motion from a variational principle,

$$\dot{q}^a = \frac{\partial H}{\partial p_a} \tag{2.24}$$

$$\dot{p}_a = -\frac{\partial H}{\partial q^a}. \tag{2.25}$$

There are major differences between the variational principles of the Lagrangian and Hamiltonian formalisms. First and foremost, the Lagrangian action is an integral in the configuration space whereas the Hamiltonian action is an integral in the phase space. This also means that in the Lagrangian formulation the variation in the coordinate variables q^a also determines the variation in the derivative variables $\dot{q}^a$, but in the Hamiltonian formulation the coordinate variables q^a and their conjugate momenta p_a are allowed to vary independently. This also gives us (in principle) the freedom not to fix the momenta at the end points.

One can deduce from the Hamiltonian formulation, e.g., that there are no attractors, which were discussed in the introduction, in Hamiltonian systems. This is a result of Liouville's phase-space theorem, which states that the Liouville measure $d\mu = dp_a dq^a$ is invariant under Hamiltonian dynamics [11].

From now on we will only work in Hamiltonian formulation and use the phase space variables (q^a, p_a) unless otherwise stated.

2.3 Poisson brackets

It is often useful to introduce new mathematical operators in order to simplify the treatment of the problem and to emphasize some aspects of the theory. With this in mind, let us consider how a general function of phase space variables and time evolves:

$$
\begin{aligned}
\frac{df}{dt} &= \frac{\partial f}{\partial q^a}\dot{q}^a + \frac{\partial f}{\partial p_a}\dot{p}_a + \frac{\partial f}{\partial t} \\
&\stackrel{\text{HEOM}}{=} \frac{\partial f}{\partial q^a}\frac{\partial H}{\partial p_a} - \frac{\partial f}{\partial p_a}\frac{\partial H}{\partial q^a} + \frac{\partial f}{\partial t} \\
&= \{f, H\} + \frac{\partial f}{\partial t}.
\end{aligned}
\tag{2.26}
$$

Here $\{\cdot, \cdot\}$ is the Poisson bracket, a bilinear operator defined for two functions f and g of the phase space variables (and time) as

$$
\{f, g\} = \frac{\partial f}{\partial q^a}\frac{\partial g}{\partial p_a} - \frac{\partial f}{\partial p_a}\frac{\partial g}{\partial q^a}.
\tag{2.27}
$$

By using Eq. (2.26), we can easily write the Hamiltonian equations of motion as

$$
\dot{q}^a = \{q^a, H\}
\tag{2.28}
$$

$$
\dot{p}_a = \{p_a, H\}.
\tag{2.29}
$$

The result emphasizes that in the Hamiltonian formalism q^a and p_a are treated on an equal footing and that the equations of motion are actually symmetrical.

It is important to note that for the canonical coordinates q^a and p_a we have the fundamental Poisson brackets

$$
\{q^a, q^b\} = 0
\tag{2.30}
$$

$$
\{p_a, p_b\} = 0
\tag{2.31}
$$

$$
\{q^a, p_b\} = \delta^a_b,
\tag{2.32}
$$

where δ^a_b is the Kroenecker delta tensor. This classical formulation should be compared with the canonical commutation relations in quantum mechanics.

2.4 Canonical transformations

The canonical coordinates q^a and p_a are naturally not the only coordinates the system can be described with. It is often useful to consider some other variables that, e.g., make use of symmetries of the system.

Under a coordinate transformation $(q^a, p_b) \rightarrow (Q^a, P_a)$, we would like the form of the Hamiltonian equations of motion to remain the same, i.e., there would exist a function $K(Q^a, P_a, t)$ to act as the Hamiltonian for the new coordinates by

$$\dot{Q}^a = \frac{\partial K}{\partial P_a} \tag{2.33}$$

$$\dot{P}_a = -\frac{\partial K}{\partial Q^a}. \tag{2.34}$$

These transformations that keep the form of the Hamiltonian equations of motion the same are called *canonical transformations*.

To find a way to generate canonical transformations, we proceed as in Ref. [47]. First, we observe that the Hamiltonian equations of motion for the new coordinates must also be obtainable from the principle of a stationary action, i.e.,

$$\delta \int_{t_A}^{t_B} \left[\dot{q}^a p_a - H(q^a, p_a, t) \right] dt = 0 = \delta \int_{t_A}^{t_B} \left[\dot{Q}^a P_a - K(Q^a, P_a, t) \right] dt. \tag{2.35}$$

This means that there is a relation between $\dot{q}^a p_a - H(q^a, p_a, t)$ and $\dot{Q}^a P_a - K(Q^a, P_a, t)$. The most general form of the relation is [47]

$$\dot{q}^a p_a - H(q^a, p_a, t) = \lambda \left[\dot{Q}^a P_a - K(Q^a, P_a, t) + \frac{dG(q^a, p_a, Q^a, P_a, t)}{dt} \right], \tag{2.36}$$

where we can add the function

$$\frac{dG(q^a, p_a, Q^a, P_a, t)}{dt}$$

since the value of its integral is independent of the path.

Multiplication with λ is somewhat trivial as we can always make a scale transformation to variables for which $\lambda = 1$ [47]. To see this, suppose we make a scale transformation

$$Q^a = \mu q^a \tag{2.37}$$

$$P_a = \nu p_a. \tag{2.38}$$

The equations of motion for the new coordinates (Q^a, P_a) can be directly calculated:

$$\dot{Q}^a = \mu \dot{q}^a = \mu \frac{\partial H(q^a, p_a, t)}{\partial p_a} = \mu \frac{\partial H(q^i(Q^i), p_i(P_i), t)}{\partial P_b} \frac{\partial P_b}{\partial p_a}$$
$$= \frac{\partial \left[\mu \nu H(q^i(Q^i), p_i(P_i), t) \right]}{\partial P_a} \equiv \frac{\partial K(Q^i, P_i, t)}{\partial P_a} \tag{2.39}$$

and

$$\dot{P}^a = \nu \dot{p}_a = -\nu \frac{\partial H(q^i, p_i, t)}{\partial q^a} = -\nu \frac{\partial H((q^i(Q^i), p_i(P_i), t)}{\partial Q^b} \frac{\partial Q^b}{\partial q^a}$$
$$= -\frac{\partial \left[\mu \nu H(q^i(Q^i), p_i(P_i), t) \right]}{\partial Q^a} \equiv -\frac{\partial K(Q^i, P_i, t)}{\partial Q^a}, \tag{2.40}$$

where

$$K(Q^a, P_a, t) = \mu \nu H(q^i(Q^i), p_i(P_i), t) \tag{2.41}$$

is the Hamiltonian for the new coordinates (Q^a, P_a). Here $\lambda = \mu \nu$ when comparing to Eq. (2.36).

In the following, we will discuss canonical transformations for which $\lambda = 1$. This is justified since we can always couple a canonical transformation with a scale transformation if we have $\lambda \neq 1$. The relation between the old and the new coordinates for canonical transformations is

$$\dot{q}^a p_a - H(q^a, p_a, t) = \dot{Q}^a P_a - K(Q^a, P_a, t) + \frac{dG(q^a, p_a, Q^a, P_a, t)}{dt}. \tag{2.42}$$

The function G acts as a *generating function* for the transformation and can be used to specify the transformation at hand.

Example 1
Let the generating function be $G = G_2(q^a, P_a, t) - Q^a P_a$. The relationship between the old and the new variables can be calculated from Eq. (2.42):

$$\dot{q}^a p_a - H = \dot{Q}^a P_a - K + \frac{\partial G_2}{\partial q^a} \dot{q}^a + \frac{\partial G_2}{\partial P_a} \dot{P}_a + \frac{\partial G_2}{\partial t} - \dot{Q}^a P_a - Q^a \dot{P}_a.$$

Since $\dot{q}^a$ and $\dot{P}_a$ are independent, we get

$$p_a = \frac{G_2}{\partial q^a}, \tag{2.43}$$

$$Q^a = \frac{\partial G_2}{\partial P_a}, \tag{2.44}$$

$$H = K - \frac{\partial G_2}{\partial t}. \tag{2.45}$$

From this class of transformations we can obtain, for example, the identity transformation $p_a = P_a$ and $q^a = Q^a$ by setting $G_2 = q^a P_a$.

We would still need some additional conditions to check whether a given transformation is canonical or not. First, we derive the so called *direct conditions* following Refs. [47, 50].

Suppose that the generator has no no explicit time-dependence, i.e.,

$$\frac{\partial G}{\partial t} = 0.$$

This means that $K(Q^a, P_a) = H(Q^a, P_a)$, and the Hamiltonian equations of motion yield

$$\dot{p}_a = -\frac{\partial H}{\partial q^a} = -\frac{\partial H}{\partial Q^b}\frac{\partial Q^b}{\partial q^a} - \frac{\partial H}{\partial P_b}\frac{\partial P_b}{\partial q^a} \overset{\text{HEOM}}{=} \dot{P}_b\frac{\partial Q^b}{\partial q^a} - \dot{Q}^b\frac{\partial P_b}{\partial q^a}. \tag{2.46}$$

On the other hand, we have

$$\dot{p}_a = \frac{\partial p_a}{\partial P_b}\dot{P}_b + \frac{\partial p_a}{\partial Q^b}\dot{Q}^b. \tag{2.47}$$

Since these two forms must be equal and $\dot{Q}^a$ and $\dot{P}_a$ are independent (because Q^a and P_a are), we get the first set of direct conditions

$$\frac{\partial p_a(Q, P)}{\partial Q^b} = -\frac{\partial P_b(q, p)}{\partial q^a}, \tag{2.48}$$

$$\frac{\partial p_a(Q, P)}{\partial P_b} = \frac{\partial Q^b(q, p)}{\partial q^a}. \tag{2.49}$$

Here it is easy to get confused with what is a function and what is a variable. To clarify, let us consider the first equation. On the left hand side, $p_a = p_a(Q, P)$ is a function of $2N$ variables and $\frac{\partial p_a(Q,P)}{\partial Q^b}$ is the partial derivative of the function p_a with respect to its bth variable. On the right hand side, $P_b = P_b(q, p)$ is a function of $2N$ variables and the partial derivative is taken with respect to its ath variable.

Other two direct conditions can be obtained by writing the Hamiltonian equations of motion for the coordinate variables, i.e.,

$$\dot{q}^a = \frac{\partial H}{\partial p_a} = \frac{\partial H}{\partial Q^b}\frac{\partial Q^b}{\partial p_a} + \frac{\partial H}{\partial P_b}\frac{\partial P_b}{\partial p_a} \overset{\text{HEOM}}{=} -\dot{P}_b\frac{\partial Q^b}{\partial p_a} + \dot{Q}_b\frac{\partial P_b}{\partial p_a}. \tag{2.50}$$

We also have

$$\dot{q}^a = \frac{\partial q^a}{\partial P_b}\dot{P}_b + \frac{\partial q^a}{\partial Q^b}\dot{Q}^b. \tag{2.51}$$

Again, since $\dot{Q}^a$ and $\dot{P}_a$ are independent, we get

$$\frac{\partial q^a(Q, P)}{\partial Q^b} = \frac{\partial P_b(q, p)}{\partial p_a}, \tag{2.52}$$

$$\frac{\partial q^a(Q, P)}{\partial P_b} = -\frac{\partial Q^b(q, p)}{\partial p_a}. \tag{2.53}$$

To sum up, the direct conditions are

$$\frac{\partial q^a(Q,P)}{\partial Q^b} = \frac{\partial P_b(q,p)}{\partial p_a}, \tag{2.54}$$

$$\frac{\partial q^a(Q,P)}{\partial P_b} = -\frac{\partial Q^b(q,p)}{\partial p_a}, \tag{2.55}$$

$$\frac{\partial p_a(Q,P)}{\partial Q^b} = -\frac{\partial P_b(q,p)}{\partial q^a}, \tag{2.56}$$

$$\frac{\partial p_a(Q,P)}{\partial P_b} = \frac{\partial Q^b(q,p)}{\partial q^a}. \tag{2.57}$$

The above derivation was done for time-independent transformations, but the direct conditions hold also for time-dependent transformations [47]. The proof, however, is rather technical and we omit it here.

Now, by using the direct conditions, we can easily verify that the fundamental Poisson brackets (2.30), (2.31), and (2.32) also hold for the new variables Q^a and P_a:

$$\{Q^a, Q^b\}_{qp} = \frac{\partial Q^a}{\partial q^c}\frac{\partial Q^b}{\partial p_c} - \frac{\partial Q^a}{\partial p_c}\frac{\partial Q^b}{\partial q^c} \stackrel{(2.55)\ \&\ (2.57)}{=} -\frac{\partial Q^a}{\partial q^c}\frac{\partial q^c}{\partial P_b} - \frac{\partial Q^a}{\partial p_c}\frac{\partial p_c}{\partial P_b}$$

$$= -\frac{\partial Q^a}{\partial P_b} = 0, \tag{2.58}$$

$$\{P_a, P_b\}_{qp} = \frac{\partial P_a}{\partial q^c}\frac{\partial P_b}{\partial p_c} - \frac{\partial P_a}{\partial p_c}\frac{\partial P_b}{\partial q^c} \stackrel{(2.54)\ \&\ (2.56)}{=} \frac{\partial P_a}{\partial q^c}\frac{\partial q^c}{\partial Q^b} + \frac{\partial P_a}{\partial p_c}\frac{\partial p_c}{\partial Q^b}$$

$$= \frac{\partial P_a}{\partial Q^b} = 0, \tag{2.59}$$

$$\{Q^a, P_b\}_{qp} = \frac{\partial Q^a}{\partial q^c}\frac{\partial P_b}{\partial p_c} - \frac{\partial Q^a}{\partial p_c}\frac{\partial P_b}{\partial q^c} \stackrel{(2.55)\ \&\ (2.57)}{=} \frac{\partial p_c}{\partial P_a}\frac{\partial P_b}{\partial p_c} + \frac{\partial q^c}{\partial P_a}\frac{\partial P_b}{\partial q^c}$$

$$= \frac{\partial P_b}{\partial P_a} = \delta^a_b, \tag{2.60}$$

Here we have used the chain rule in the second-to-last step for each of the fundamental Poisson brackets.

This, in fact, allows us to use the fundamental Poisson brackets to check whether a transformation is canonical or not: a transformation is canonical if, and only if, the new variables obey the fundamental Poisson brackets [50].

Furthermore, all the Poisson brackets $\{f, g\}$ are invariant (often called canonical invariants) under canonical transformations. This can be verified by a direct

calculation:

$$
\begin{aligned}
\{f,g\}_{qp} &\equiv \frac{\partial f}{\partial q^a}\frac{\partial g}{\partial p_a} - \frac{\partial f}{\partial p_a}\frac{\partial g}{\partial q^a} \\
&= \left(\frac{\partial f}{\partial Q^b}\frac{\partial Q^b}{\partial q^a} + \frac{\partial f}{\partial P_b}\frac{\partial P_b}{\partial q^a}\right)\left(\frac{\partial g}{\partial Q^c}\frac{\partial Q^c}{\partial p_a} + \frac{\partial g}{\partial P_c}\frac{\partial P_c}{\partial p_a}\right) \\
&\quad - \left(\frac{\partial f}{\partial Q^b}\frac{\partial Q^b}{\partial p_a} + \frac{\partial f}{\partial P_b}\frac{\partial P_b}{\partial p_a}\right)\left(\frac{\partial g}{\partial Q^c}\frac{\partial Q^c}{\partial q^a} + \frac{\partial g}{\partial P_c}\frac{\partial P_c}{\partial q^a}\right) \\
&= \frac{\partial f}{\partial Q^b}\frac{\partial g}{\partial Q^c}\underbrace{\{Q^b,Q^c\}}_{=0} + \frac{\partial f}{\partial P_b}\frac{\partial g}{\partial Q^c}\underbrace{\{P_b,Q^c\}}_{=-\delta^c_b} \\
&\quad + \frac{\partial f}{\partial Q^b}\frac{\partial g}{\partial P_c}\underbrace{\{Q^b,P_c\}}_{=\delta^b_c} - \frac{\partial f}{\partial P_b}\frac{g}{\partial P_c}\underbrace{\{P_b,P_c\}}_{=0} \\
&= \frac{\partial f}{\partial Q^b}\frac{\partial g}{\partial P_b} - \frac{\partial f}{\partial P_b}\frac{\partial g}{\partial Q^b} \\
&\equiv \{f,g\}_{QP}.
\end{aligned}
\tag{2.61}
$$

2.5   Relationship between symmetries and conserved quantities

One would expect to find a relationship between symmetries of the system (which, in this case, mean the symmetries of the Hamiltonian) and conserved quantities. For example, a system of one particle in a central potential is spherically symmetric, and for this reason, the angular momentum is conserved.

Following Refs. [47,50], let us consider a transformation induced by the generator

$$
G = q^a P_a + \epsilon F(q^a, P_a, t) - Q^a P_a
\tag{2.62}
$$

when ϵ is infinitesimal. Notice that this is just one possible type of a generator. From Eqs. (2.43) and (2.44) we get

$$
Q^a = q^a + \epsilon \frac{\partial F}{\partial P_a},
\tag{2.63}
$$

$$
p_a = P_a + \epsilon \frac{\partial F}{\partial q^a}.
\tag{2.64}
$$

Since ϵ is infinitesimal, we can replace $\frac{\partial}{\partial P_a} \approx \frac{\partial}{\partial p_a} + O(\epsilon)$ and keep only the first term (since further expansions yields final terms of order ϵ^2 and higher) to get

$$
Q^a \doteq q^a + \delta q^a = q^a + \epsilon \frac{\partial F}{\partial p_a},
\tag{2.65}
$$

$$
P_a \doteq p_a + \delta p_a = p_a - \epsilon \frac{\partial F}{\partial q^a}.
\tag{2.66}
$$

In general, a time-independent generator[6] F creates a change in a phase space function $A(q^a, p_a)$ such that

$$A \to A + \delta A, \tag{2.67}$$

where using Eqs. (2.65) and (2.66) we get

$$\delta A = \frac{\partial A}{\partial q^a} \delta q^a + \frac{\partial A}{\partial p_a} \delta p_a = \epsilon \frac{\partial A}{\partial q^a} \frac{\partial F}{\partial p_a} - \epsilon \frac{\partial A}{\partial p_a} \frac{\partial F}{\partial q^a} = \epsilon \{A, F\}. \tag{2.68}$$

Here, A can naturally denote also q^a or p_a. These kinds of transformations are called *infinitesimal canonical transformations* (ICT) [47].

Now we have the tools to understand how a continuous symmetry of the Hamiltonian relates to conservation laws. Consider a change in the Hamiltonian under an ICT generated by F,

$$\delta H = H(q^a + \delta q^a, p_a + \delta p_a) - H(q^a, p_a) \overset{(2.68)}{=} \epsilon \{H, F\}. \tag{2.69}$$

If F has no explicit time dependence, then by Eq. (2.26) we have

$$\dot{F} = \{F, H\} = -\{H, F\}. \tag{2.70}$$

In other words, if $\dot{F} = 0$, i.e., F is a constant of motion, then H is invariant, i.e., symmetric, under transformations generated by F. The reverse is also true: If H has a continuous symmetry with the generator F, then F is a constant of motion.

Here continuity is implied by the infinitesimality of the transformations. The information content of the above statement is the same as in *Nöther's theorem*. Let us now consider a few examples.

Example 2 Momentum as a generator of translation

Let us use the generator

$$G = q^a P_a + \epsilon F(q^a, p_a) - Q^a P_a, \tag{2.71}$$

where we set $F = p_i$ for some i. From Eqs. (2.32) and (2.68) we get

$$Q^a = q^a + \delta_i^a \epsilon, \tag{2.72}$$

where δ_i^a is the Kroenecker delta tensor, and

$$P_a = p_a. \tag{2.73}$$

Hence, momentum p_i generates translation in q^i. Similarly, $-q^i$ generates translation in p_i.

---

[6]In these kinds of infinitesimal transformations, we often call F the generator even if G is the actual generator.

Example 3 Hamiltonian as a generator of time evolution

Take

$$G = q^a P_a + \epsilon F(q^a, p_a) - Q^a P_a, \tag{2.74}$$

where $F = H(q^a, p_a)$, as the generator. From Eq. (2.68) we see that a general function A of q^a and p_a transforms as

$$
\begin{aligned}
A \to A + \delta A &= A(q^a, p_a) + \epsilon\{A(q^a, p_a), H\} \\
&= A(q^a, p_a) + \epsilon\left(\frac{\partial A}{\partial q^c}\frac{\partial H}{\partial p_c} - \frac{\partial A}{\partial p_c}\frac{\partial H}{\partial q^c}\right) \\
&\stackrel{\text{HEOM}}{=} A(q^a, p_a) + \epsilon\left(\frac{\partial A}{\partial q^c}\dot{q}^c + \frac{\partial A}{\partial p_c}\dot{p}^c\right) \\
&= A(q^a, p_a) + \epsilon\frac{dA}{dt} = A(q^a(t + \epsilon), p_a(t + \epsilon)).
\end{aligned}
\tag{2.75}
$$

Thus, the Hamiltonian generates time evolution.

For completeness, let us see how to construct a finite canonical transformation from ICTs. Previously, we have seen that under an ICT generated by F the quantities A transform as

$$A \to A + \delta A = (1 + \epsilon\{\cdot, F\})A,$$

where $\{\cdot, F\}A = \{A, F\}$. Suppose that ϵ is no longer infinitesimal. We could then divide the transformation into n smaller transformations,[7] each of which would approach an ICT as $n \to \infty$:

$$A + \Delta A = \lim_{n\to\infty}\left(1 + \frac{\epsilon}{n}\{\cdot, F\}\right)^n A = e^{\epsilon\{\cdot, F\}}A, \tag{2.76}$$

where in the last step we have used the limit definition of the exponential function. We see that these canonical transformations can be expressed as exponential operators by using the Poisson brackets.

Example 4 Time evolution as a canonical transformation

From Example 3 above we know that the Hamiltonian is the generator of time evolution. According to the above derivation for finite canonical transformations, we can write the time evolution of the system in the form

$$q^a(t) = e^{t\{\cdot, H\}}q^a(t = 0), \tag{2.77}$$

$$p_a(t) = e^{t\{\cdot, H\}}p_a(t = 0). \tag{2.78}$$

---

[7]We can do this since the canonical transformations form a group [47].

2.6 Billiards

Hamiltonian systems are often studied using *billiards* as model systems. A billiards is a deterministic Hamiltonian system where a point particle (the billiard ball) moves in a deterministic way described by the Hamiltonian H between elastic collisions with the billiard boundary (billiard table) as in Fig. 14(a).

Typically, the trajectory is a straight line between the collisions, but also, e.g., billiards in magnetic fields, where the trajectory is a circular arc between the collisions, have been studied [41, 51, 52]. Despite the popularity of hard-wall billiards, also soft billiards, i.e., billiards with no infinite potentials, have been studied, e.g., in Ref. [53].

Billiards offer geometrically simple (in configuration space) Hamiltonian systems suitable for the study of Hamiltonian chaos. By changing the geometry of the billiard table, dimensionality, and the form of the trajectories (straight line, circular arc, etc.), we can generate different Hamiltonian systems that can exhibit a vast variety of different kinds of dynamics. In addition, often most chaotic phenomena of Hamiltonian systems can be obtained already in two-dimensional billiards so that the configuration space geometry of the trajectory is easy to visualize.

We can also give a more rigorous definition for a billiard system

> **Definition 1** *A billiard table Q is an n-dimensional compact, connected subset of $\mathbb{R}^n$ with a piecewise smooth boundary ∂Q.*

> **Definition 2** *A billiards* is a dynamical system where a point described by the generalized coordinates $q^a \in Q$ moves according to some Hamiltonian H inside the *billiard table Q* between elastic collisions with the boundary ∂Q. The collisions result in a transformation
>
> $$
> \begin{aligned}
> q &\to q \\
> p &\to p - 2(n \cdot p)n,
> \end{aligned}
> \tag{2.79}
> $$
>
> where n is the unit normal of the boundary pointing towards the interior of Q.[8]

This definition has one obvious flaw: What happens when the trajectory collides with the boundary at a point where the boundary curve is not differentiable, i.e., n is not well defined? These trajectories are, however, very rare, and we need not consider them at all.

The trajectories in the phase space constitute to the *billiard flow*, whereas the mapping $T : \partial Q \to \partial Q$ from one collision with the boundary to next defines the so called *collision map*. Properties of the collision map are analyzed in Sec. 3.2.1.

---

[8]Here we have $q = (q^1, \ldots, q^n)$ and $p = (p_1, \ldots, p_n)$.

3 Chaos in Hamiltonian systems

3.1 Lyapunov exponent

In the introduction in Sec. 1.2 we gave a definition for chaotic dynamics, the most important part of which was the sensitivity to initial conditions. In this section we develop, following Ref. [11], a quantitative measure for the sensitivity to initial conditions.

Quantitative measure for chaoticity of a system trajectory is given by the separation rate of two initially infinitesimally nearby trajectories. This divergence (or convergence) rate is typically asymptotically exponential, and the exponent – called the *Lyapunov exponent* – characterizes the stability of the trajectory as described in detail in the following.

The Lyapunov exponent can be defined both for flows and maps. Here we focus on the latter since it is most easily applicable to billiards.

In discrete systems, trajectories can be described by a numerable set of points $\{x_0, x_1, x_2, \dots\}$ where each point x_i is an element of the phase space of the system $\mathbb{P} \subset \mathbb{R}^N$. Although the points of the trajectory are labeled here by natural numbers i, it is sometimes useful also to consider a discrete time variable t_i corresponding to each discrete label i as is done later in Sec. 3.2.1.

Let us consider a system where the system trajectory can be generated from the initial point x_0 by a C^1-mapping $T : \mathbb{P} \to \mathbb{P}$ in such way that $x_1 = Tx_0$, $x_2 = Tx_1$, and so on.

We shall now see how a small perturbation ξ_0 of the initial point x_0 evolves. In the first iteration we get

$$x_1 + \xi_1 = T(x_0 + \xi_0) \approx DT\big|_{x_0} \xi_0 + Tx_0, \tag{3.1}$$

where in the last step we have made a linear approximation justified by the small perturbation. Since $x_1 = Tx_0$, we get $\xi_1 = DT\big|_{x_0} \xi_0$, where $DT\big|_{x_0} \xi_0$ is the derivative of T evaluated at x_0 acting on ξ_0. Similarly for the next iteration,

$$\begin{aligned} x_2 + \xi_2 = T(x_1 + \xi_1) &\approx DT\big|_{x_1} \xi_1 + Tx_1 \\ &= DT\big|_{x_1} DT\big|_{x_0} \xi_0 + T^2 x_0, \end{aligned} \tag{3.2}$$

where in the last step we have used the result for the perturbation from the previous iteration. Here $T^2 x_0 \equiv T(Tx_0)$. Thus, we get

$$\xi_2 \approx DT\big|_{x_1} DT\big|_{x_0} \xi_0. \tag{3.3}$$

Following this procedure, we get for the $(n + 1)$th iteration

$$\begin{aligned} x_{n+1} + \xi_{n+1} = T(x_n + \xi_n) &\approx DT\big|_{x_n} \xi_n + Tx_n \\ &= DT\big|_{x_n} \cdots DT\big|_{x_0} \xi_0 + T^{n+1} x_0, \end{aligned} \tag{3.4}$$

20

which gives us

$$\xi_{n+1} \approx DT\big|_{x_n} \cdots DT\big|_{x_0} \xi_0 \equiv D^{n+1}T(x_0)\xi_0. \tag{3.5}$$

We see that the evolution of an infinitesimally small perturbation ξ is governed by the derivative (Jacobian) DT of the evolution mapping T. We now define the Lyapunov exponents as

$$\lambda\left(x_0, \frac{\xi_0}{\|\xi_0\|}\right) \equiv \lim_{n\to\infty} \frac{1}{n} \log\left(\frac{\|\xi_n\|}{\|\xi_0\|}\right)$$
$$= \lim_{n\to\infty} \frac{1}{n} \log \|D^n T(x_0)u_0\| . \tag{3.6}$$

From this definition we see that the Lyapunov exponents depend on (i) the initial state[9] x_0 and (ii) the direction of the perturbation $u_0 = \xi_0/\|\xi_0\|$. The existence of the limit has been proven by Lyapunov [54] and Osedelet [55].

Actually, we can only get N (or fewer) distinct values for the limit (3.6) for a given x_0 in a phase space of dimension N. To give an in-depth explanation of this, we define a finite-time Lyapunov exponent

$$\lambda_n (x_0, u_0) \equiv \frac{1}{n} \log \|D^n T(x_0)u_0\| , \tag{3.7}$$

which can easily be rewritten as

$$\lambda_n (x_0, u_0) = \frac{1}{2n} \log |[D^n T(x_0)u_0]^\top D^n T(x_0)u_0|$$
$$= \frac{1}{2n} \log \left|u_0^\top [D^n T(x_0)]^\top D^n T(x_0)u_0\right|$$
$$= \frac{1}{2n} \log \left|u_0^\top H^n(x_0)u_0\right|. \tag{3.8}$$

The matrix $H^n(x_0)$ is real and symmetric since it is of the form $H^n(x_0) = A^\top A$, where A is a square matrix. Furthermore, due to its form $H^n(x_0)$ is positive semi-definite, i.e.,

$$u^\top H^n(x_0)u = u^\top A^\top A u = (Au)^\top (Au) \geq 0 \ \forall u \in \mathbb{R}^N.$$

All eigenvalues of a positive semi-definite matrix are real and nonnegative, and since $H^n(x_0)$ is also symmetric, it is possible to choose a complete set of orthonormal eigenvectors e_i with eigenvalues $h_{i,n}$. The direction of the initial perturbation u_0 can be expanded in this basis,

$$u_0 = \sum_i a_i e_i. \tag{3.9}$$

---

[9]In ergodic systems the Lyapunov exponents are independent of the initial state x_0. This is addressed later in Sec. 3.2.4

This gives us

$$\lambda_n(\boldsymbol{x}_0, \boldsymbol{u}_0) = \frac{1}{2n} \log \left| \sum_{i,j} a_i a_j \boldsymbol{e}_i^\mathsf{T} \boldsymbol{e}_j h_{j,n} \right|$$

$$= \frac{1}{2n} \log \left| \sum_i a_i^2 h_{i,n} \right|, \tag{3.10}$$

where in the last step we used the orthonormality of the basis. Each eigenvector of H^n corresponds to one finite-time Lyapunov exponent

$$\lambda_{i,n} = \frac{1}{2n} \log(h_{i,n}), \tag{3.11}$$

where i labels the eigenvectors of H^n.

We can order these finite-time exponents $\lambda_{1,n} \geq \lambda_{2,n} \geq \cdots \geq \lambda_{N,n}$. As we let $n \to \infty$, we get N (or fewer) different *Lyapunov exponents* (denoting $\lambda_{i,\infty} \doteq \lambda_i$)

$$\lambda_1 \geq \cdots \geq \lambda_N. \tag{3.12}$$

Let us now see how a perturbation in a random direction evolves. The existence of the limit (3.6) implies that for large n we have an approximate relation

$$\|\xi_n\| \approx \|\xi_0\| \exp(\lambda n). \tag{3.13}$$

Furthermore, the exponent λ can be approximated as

$$\lambda \approx \lambda_n = \frac{1}{2n} \log \left| \sum_i a_i^2 h_{i,n} \right| = \frac{1}{2n} \log \left| \sum_i a_i^2 \exp(2n\lambda_{i,n}) \right|. \tag{3.14}$$

When n is large, the sum is dominated by $\lambda_{1,n}$, which in the limit $n \to \infty$ corresponds to the largest Lyapunov exponent $\lambda = \lambda_1$. This is also called the *maximal Lyapunov exponent*.

When at least one of the Lyapunov exponents is positive, the trajectory in question is unstable to most small perturbations, and the larger the maximal Lyapunov exponent the more unstable the trajectory is. On the other hand, when all Lyapunov exponents are zero or negative, the trajectory is stable to small perturbations, i.e., the trajectory is regular. In this sense, we now have a quantitative measure for the sensitivity to initial conditions, which was one requirement of chaotic motion in Sec. 1.2.

Hamiltonian systems and their maps (defined in the next section) are symplectic [11]. As a result, all the Lyapunov exponents of the flow and the maps come in pairs $\pm\lambda_1, \pm\lambda_2, \ldots, \pm\lambda_{n/2}$ [11]. Therefore, there can be no attracting trajectories in Hamiltonian systems, and all regular trajectories in Hamiltonian systems have all Lyapunov exponents equal to zero.

As the term "chaotic" is used in different contexts, we define more rigorous terminology as in the literature [56]. We call a trajectory *hyperbolic* if one of its

Lyapunov exponents is positive. Furthermore, an invariant (under the dynamics) set is called hyperbolic if almost all its trajectories are hyperbolic.[10] Hyperbolic sets are often called *chaotic seas*.

As an example, let us now calculate the Lyapunov exponent of the tent map.

Example 5   Lyapunov exponent of the tent map

Consider the one-dimensional tent map

$$T_\mu : [0,1] \rightarrow [0,1] : x \mapsto \mu \min\{x, 1-x\}, \; \mu \in [0,2]. \tag{3.15}$$

One dimensional maps T_μ have only one Lyapunov exponent, for which the formula reduces to

$$\begin{aligned}
\lambda &= \lim_{n\to\infty} \frac{1}{n} \log \left| T'_\mu(x_{n-1}) \frac{\xi_n}{\xi_0} \right| \\
&= \lim_{n\to\infty} \frac{1}{n} \log \left| T'_\mu(x_{n-1}) \cdots T'_\mu(x_0) \frac{\xi_0}{\xi_0} \right| \\
&= \lim_{n\to\infty} \frac{1}{n} \sum_{i=0}^{n-1} \log \left| T'_\mu(x_i) \right|
\end{aligned} \tag{3.16}$$

If we apply this to the tent map, for which $|T'_\mu(x)| = |\mu|$, we get

$$\lambda = \log |\mu|, \tag{3.17}$$

which means that for $\mu \leq 1$ the tent map is regular and for $\mu > 1$ it is hyperbolic.

The Lyapunov exponent of the tent map with $\mu = 1.2$ is illustrated in Fig. 6, where the solid (blue) curve corresponds to true evolution of the absolute value of the perturbation and the dashed (red) line corresponds to exponential evolution with Lyapunov exponent $\lambda = \log 1.2$. We see that for low iteration numbers the curves are equal which is due to the linearization being accurate. For larger iteration numbers, the actual perturbation saturates due to boundedness of the system coordinates.

---

[10]The requirement, that almost all trajectories of the set are hyperbolic, means that (possible) nonhyperbolic trajectories of the set form a subset of zero measure.
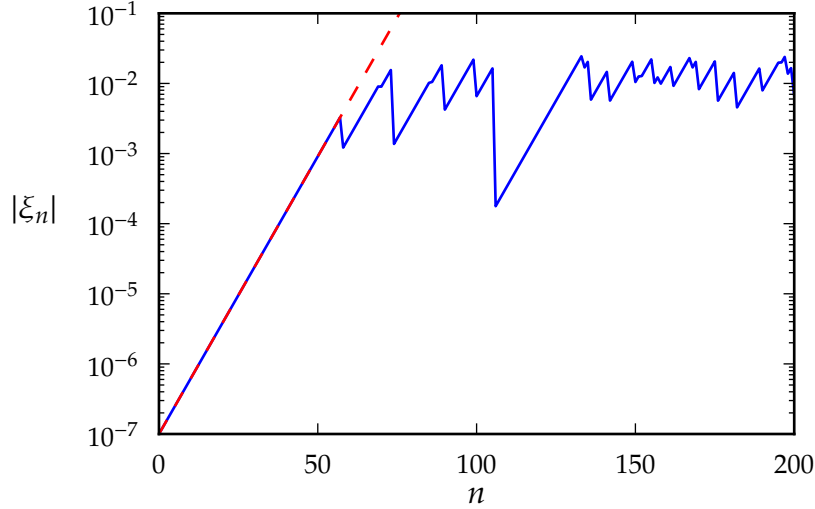
Figure 6: Evolution of a small perturbation for the tent map with $\mu = 1.3$ and the initial condition $x = 0.3$ (blue) and the exponential separation rate calculated from the Lyapunov exponent (red).

As a final note, let us give a geometrical interpretation for the meaning of Lyapunov exponents. An infinitesimal N-sphere centered at x_0 in phase space evolves to an N-ellipsoid after n iterations under the linearized dynamics given by DT^n [11]. The situation is illustrated with a two-dimensional ball in Fig. 7. We give the proof [57] for two dimensional case to convince the reader. Notice, however, that this holds only in the infinitesimal neighborhood of x_0 since the Jacobian DT changes as we move from x_0 to its neighborhood.

Example 6   Evolution of a sphere under a linear map

Let $\mathbf{T} : \mathbb{R}^2 \to \mathbb{R}^2$ be an invertible linear map with the corresponding matrix

$$A \doteq \mathrm{mat}\, \mathbf{T} = \begin{bmatrix} a & b \\ c & d \end{bmatrix}. \tag{3.18}$$

The boundary circle of a ball $B_2(0)$ centered at $[0,0]^\mathsf{T}$ can be parameterized by

$$R \begin{bmatrix} \cos t \\ \sin t \end{bmatrix}. \tag{3.19}$$

Let us now consider how the boundary circle transforms under $\mathbf{T}$:

$$\begin{bmatrix} x \\ y \end{bmatrix} = \mathbf{T}R \begin{bmatrix} \cos t \\ \sin t \end{bmatrix}. \tag{3.20}$$

This can be inverted to yield

$$R \begin{bmatrix} \cos t \\ \sin t \end{bmatrix} = \mathbf{T}^{-1} \begin{bmatrix} x \\ y \end{bmatrix} = \frac{1}{ad - bc} \begin{bmatrix} dx - by \\ ay - cx \end{bmatrix}, \tag{3.21}$$

24
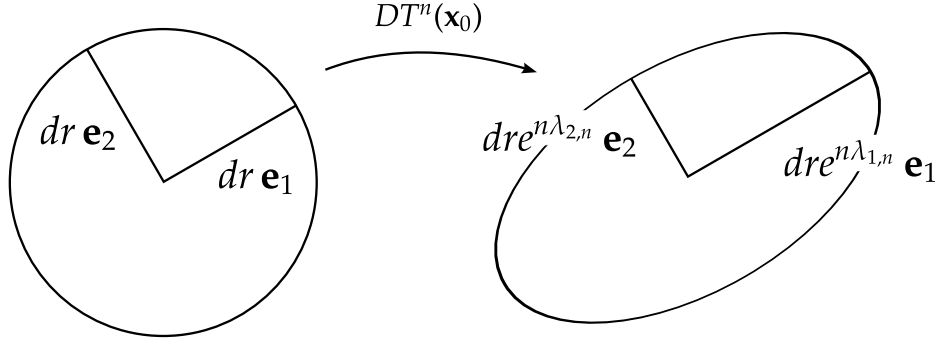
Figure 7: Infinitesimal ball in phase space evolves into an ellipsoid under linearized dynamics. Adapted from Ref. [11].

which gives

$$R^2 = R^2(\cos^2 t + \sin^2 t) = \frac{1}{(ad - bc)^2}\left[(dx - by)^2 + (ay - cx)^2\right] \quad (3.22)$$

$$(ad - bc)^2 R^2 = (d^2 + c^2)x^2 + (a^2 + b^2)y^2 - 2(ac + db)xy. \quad (3.23)$$

This is an equation for an ellipse.

Furthermore, since $\mathbf{T}$ is a continuous map and $B_2(0)$ is a compact set, the image $\mathbf{T}B_2(0)$ must also be compact. Since the origin is mapped to the origin and $\mathbf{T}\partial B_2(0) = \partial \mathbf{T}B_2(0)$ for linear maps, i.e., the boundary maps to the boundary, we find that the interior of the circle must be mapped to the interior of the ellipse to preserve compactness. We can thus conclude that the 2-sphere is mapped to a 2-ellipsoid under a linear, invertible map $\mathbf{T}$.

Now consider again the infinitesimal N-sphere in phase space. The sphere is mapped to an N-ellipsoid under the linearized dynamics of n iterations. The lengths of the principal axes of the ellipsoid are given by the finite time Lyapunov exponents so that they become approximately $dr \exp(\lambda_i n)$. There is, however, no general connection between the directions of the principal axes and the Lyapunov exponents as the orientation of the ellipsoid is not constant: it depends heavily on the dynamics and, more importantly, the number of iterations n [58].

3.2 Structure of the phase space

3.2.1 Poincaré section

Often the full phase space is difficult to study, and one wishes to reduce the number of dimensions without losing information on the dynamics. This can be done with the help of a *Poincaré surface of section*.

In a phase space $\mathbb{P}$ of dimension p, we can define a $(p-1)$–dimensional hypersurface $\mathbb{P}_r$ (Poincaré surface of section or Poincaré section) in such a way that each point in $\mathbb{P}_r$ corresponds uniquely to a point (trajectory) in phase space. Not to lose any information on the full phase space, all trajectories of the system should intersect with the Poincaré section.

The Poincaré section defines the Poincaré map $T : \mathbb{P}_r \to \mathbb{P}_r$, which maps a point on the surface of section to the next crossing of the corresponding trajectory with the Poincaré section. This allows us to analyze continuous trajectories (flow) with a discrete mapping T.

In billiards (with fixed energy) it is convenient to choose the boundary ∂Q accompanied by the tangential momentum $p_\parallel$ as the Poincaré section. The Poincaré section can be parametrized by the Birkhoff coordinates, i.e., the arc length s and the tangential momentum $p_\parallel$ of the incoming (or the outgoing) particle at the collision point. Often the norm of the momentum is fixed to unity so that the tangential momentum is the cosine of the collision angle. In billiards, the Poincaré map is often called the *collision map*. Note that the collision map preserves Poincaré section area when parametrized with the Birkhoff coordinates [51]. This property is essential for the KAM-theory introduced in Sec. 3.2.3.

Poincaré sections are often used to visualize three-dimensional phase spaces as two-dimensional figures by selecting a number of trajectories and calculating all their crossings with the Poincaré section. Often the obtained figures are also referred to as *Poincaré sections*.

Example 7 Consider a conservative system with the Hamiltonian

$$H = \frac{1}{2}(p_1^2 + p_2^2) + V(q_1, q_2).$$

Restriction to an energy surface $H = \text{const} \doteq E$ allows us to describe one of the coordinates as a function of the others, e.g.

$$p_2 = \sqrt{2(E - V(q_1, q_2)) - p_1^2}$$

where we have chosen to consider only positive values of p_2.

We can further reduce the three-dimensional energy surface by choosing a Poincaré section $S = \{(q_1, q_2, p_1, p_2) \in \mathbb{P} : H(q_1, q_2, p_1, p_2) = E, q_2 = 0\}$. Here S is a two-dimensional surface where every point corresponds to a single trajectory of the system.

26

Often it is also necessary to obtain temporal information on the dynamics in addition to the the Poincaré map. If we attach temporal information to the map, i.e., we keep track of the time of the crossings with the Poincaré section, we get the *true-time map* [59]. In billiards language, the collision map $T : \partial Q \to \partial Q$ is extended to the true-time map $T_\tau : \partial Q \times \mathbb{R} \to \partial Q \times \mathbb{R}$, where the extra dimension $\mathbb{R}$ keeps track of time at each collision. With the true-time map, the definition of the Lyapunov exponent in Eq. (3.6) should be modified to

$$\lambda \left(\boldsymbol{x}_0, \, \boldsymbol{u}_0\right) = \lim_{n \to \infty} \frac{1}{\tau_n} \log \|D^n T(\boldsymbol{x}_0) \boldsymbol{u}_0\| \,, \qquad (3.24)$$

where τ_n is the time at nth collision.

In the following we see how regularity, periodic and quasiperiodic orbits, mixed phase space, and chaoticity are seen in the Poincaré sections. The examples we give are in form of two-dimensional Poincaré sections, but similar structures exist also in higher dimensions.

3.2.2   Regular tori

Let us now consider an integrable or, in other words, a regular Hamiltonian system with phase space $\mathbb{P}$ of dimension $2N$. In the following we introduce a fundamental theorem on integrability in Hamiltonian systems.

> **Theorem 1**   (Arnold-Liouville theorem on integrability [60])
> A Hamiltonian system with phase space $\mathbb{P}$ of dimension $2N$ is integrable if, and only if, there exist N independent constants of motion $f_i(q^a, p_a) = k_i$, $i = 1 \ldots N$, which are in involution.

Since there are N conserved quantities $f_i(q^a, p_a) = k_i$ the trajectories corresponding to constants $\{k_i\}$ are restricted to an N-dimensional hypersurface

$$S = \{(q^a, p_a) \in \mathbb{P} : f_i(q^a, p_a) = k_i \, \forall i = 1, \ldots, N\} \,. \qquad (3.25)$$

Note that we can always choose $f_1 = H$ so that in one-dimensional systems the motion is always regular.

By independence of f_i we mean linear independence of $\{\nabla f_i\}$ at all points in the hypersurface. This requirement is necessary to guarantee the dimensionality of the hypersurface S by means of the implicit function theorem. In essence, if we had, e.g., only $N - 1$ linearly independent vectors in $\{\nabla f_i\}$, either the set would be empty, it would contain only one point, or one of the constants of motion f_i would not bring any additional constraints to the system.

Furthermore, the conserved quantities must be compatible with each other in sense that all conserved quantities must be invariant under symmetry transformations generated by the other quantities. Mathematically this is incorporated into the

theorem by requiring that they are in involution, i.e.,

$$\{f_i, f_j\} = \frac{\partial f_i}{\partial q^c}\frac{\partial f_j}{\partial p_c} - \frac{\partial f_j}{\partial q^c}\frac{\partial f_i}{\partial p_c} = 0, \tag{3.26}$$

for all pairs f_i, f_j. Consider for a moment that if this was not to the case for some i and j, i.e., $\{f_i, f_j\} \neq 0$. Then by Eq. (2.68) the transformations generated by f_j would not keep f_i invariant.

The requirement that the conserved quantities are in involution fixes the topology of the hypersurface S. It turns out that the hypersurface generated by the above conditions is diffeomorphic with an N-torus [11],[11]

$$\mathbb{T}^N = S^1 \times \cdots \times S^1 \ (N\text{-fold}),$$

where each S^1 is a unit circle.

To simplify the treatment, we can consider the hypersurface to be actually the torus since they are diffeomorphic. Naturally, we can reduce the number of variables used to describe the points on the torus. A new set of canonical coordinates (θ^i, J_i) can be chosen in which the new momenta J_i are constants of motion [11,61], and thus, the Hamiltonian depends only on the momentum J_i since

$$\frac{\partial H(\theta^i, J_i)}{\partial \theta^i} = \dot{J}_i = \frac{d}{dt}(const) = 0. \tag{3.27}$$

One such choice is $J_i = f_i(q^a, p_a)$, but this transformation is not typically canonical. The canonical coordinates (θ^i, J_i) are called the *action-angle* coordinates.

We can easily solve the Hamiltonian equations of motion in such coordinates:

$$\begin{cases} \dot{J}_i = 0 \\ \dot{\theta}^i = \frac{\partial H(\{J_a\})}{\partial J_i} \doteq \omega(\{J_a\}) \end{cases} \Rightarrow \begin{cases} J_i(t) = J_i(t = 0) \\ \theta^i(t) = \theta^i(t = 0) + \omega_i(\{J_a\})\,t. \end{cases} \tag{3.28}$$

In the action-angle coordinates, the values of J_i fix the torus in question and θ^i are angle-like coordinates that describe the position on the torus. The solution coils around the torus with angular frequencies of each direction on the torus given by $\omega_i(\{J_a\})$.

Consider a 2-torus with a trajectory around it [Fig. 8(a)]. If we unfold the torus to a rectangle [Fig. 8(b)], it is easy to see that in order for the motion to be periodic the trajectory must make an integer number of laps in both directions during some time t, i.e., ω_1/ω_2 must be rational. Similar reasoning holds also for an N-torus, but then the ratio between all frequencies ω_i/ω_j must be rational.

Quasiperiodicity, on the other hand, requires that there is no such rational dependence, i.e., there are no integers m_i for which $\sum_i m_i\omega_i = 0$.

---

[11]The diffeomorphism exists only if the surface S is compact and connected [60].

(a)   (b)
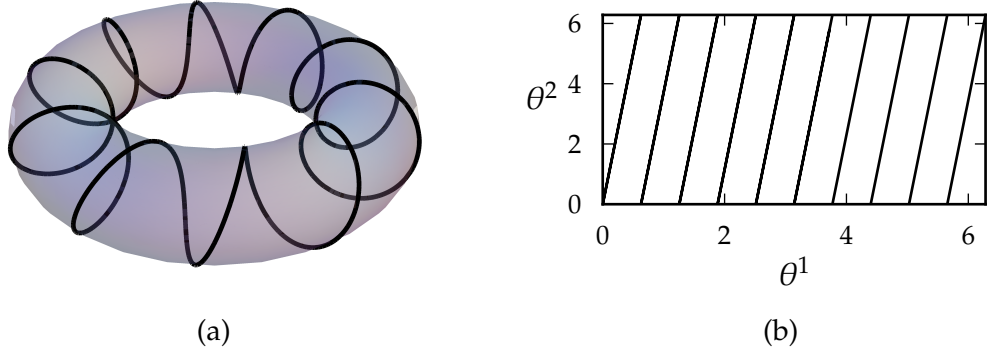
Figure 8: (a) A regular 2-torus with an example trajectory and (b) the two-torus and the orbit mapped onto $[0, 2\pi] \times [0, 2\pi]$.

Periodic orbits intersect the Poincaré section in a distinct set of points. Quasiperiodic orbits in turn fill the torus and thus we see a continuous curve in the Poincaré section. The shape of the curve depends on the coordinates used to describe the system.

3.2.3   KAM-theory and emergence of chaos

A natural question arises when considering small perturbations of the system: How stable the regular tori are with respect to the perturbations? That is, if we make a perturbation $\epsilon H'$ to an integrable Hamiltonian H_0,

$$H_0(I) \rightarrow H_0(I) + \epsilon H'(I, \theta), \tag{3.29}$$

where ϵ is small, what happens to the regular tori of the unperturbed Hamiltonian H_0? If they persisted, there would exist a generator S that would generate a new set of action-angle variables (θ', I') in which the perturbed Hamiltonian would depend only on I'.

A simple series expansion of the generator leads to so called problem of small denominators in classical mechanics where the series expansion of the generator S has terms like

$$S_1(J; m) = \frac{\kappa(J)}{\imath(\omega \cdot m)}, \tag{3.30}$$

where m is a vector of integers and ω is a vector of the frequencies of the tori [62]. This procedure, however, fails since not all the tori survive the perturbation. Especially, all the tori with rationally dependent frequencies (called rational tori) will be destroyed since for them $\omega \cdot m = 0$ for some m. For them terms such in Eq. (3.30) blow up.

A deeper insight to the effects of the perturbation can be obtained by considering the following example, which we follow from Refs. [11, 63]. The following results on the effects of perturbations on integrable systems are known as the *Kolmogorov-Arnold-Moser (KAM) theory* [64–66]. Note that most systems that exhibit the phenomena introduced in the following do not have a clear connection to some integrable system. Parts of their phase space have intrinsically similar structures

29
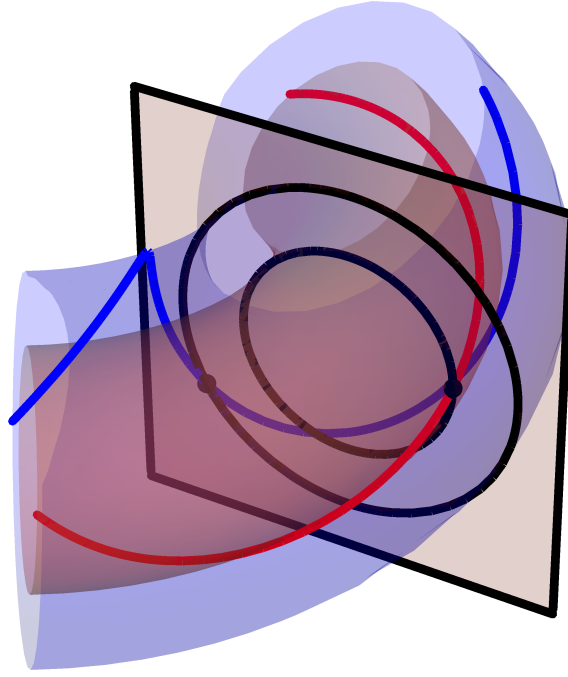
Figure 9: Poincaré section in three-dimensional phase space with regular tori. The intersections of the tori with the Poincaré section are circles. Adapted from Ref. [11].

to those that arise from perturbations to integrable systems.

Suppose we would have an unperturbed Hamiltonian with a three-dimensional energy surface filled with a set of nested two-dimensional tori $\mathbb{T}^2$ as in Fig. 9. We set up a Poincaré section (and thus a Poincaré map) on which we will visualize the effects of the perturbation on the structure of the phase space. The Poincaré map T can be parametrized by the radial distance r and the angle $\theta_1 \doteq \theta$:

$$r_{n+1} = r_n \tag{3.31}$$
$$\theta_{n+1} = \theta_n + 2\pi\xi(r_n), \tag{3.32}$$

where $\xi(r) = {}^{\omega_1}/_{\omega_2}$ is the ratio of the angular frequencies of the tori labeled by r. This can be obtained simply by unfolding the tori as in Fig. 8(b). The map [with certain conditions for $\xi(r)$] is called the *Moser twist map*. If we perturb the Hamiltonian, then also the Poincaré map T is perturbed to T_ϵ,

$$r_{n+1} = r_n + \epsilon f(r_n, \theta_n) \tag{3.33}$$
$$\theta_{n+1} = \theta_n + 2\pi\xi(r_n) + \epsilon g(r_n, \theta_n). \tag{3.34}$$

There are two kinds of tori that are of interest to us, namely rational tori and irrational tori for which the frequencies are rationally or irrationally dependent, respectively. First, we consider the effect of the perturbation on the rational tori (also called resonant tori), for which ${}^{\omega_1}/_{\omega_2} = {}^p/_q$ for some $p, q \in \mathbb{Z}$. All the points on such torus, the radius of the cross section of which is $r = r_{pq}$, are fixed points of the qth iteration of the unperturbed Poincaré map T. Suppose now that $\frac{d\xi(r)}{dr} > 0$ in
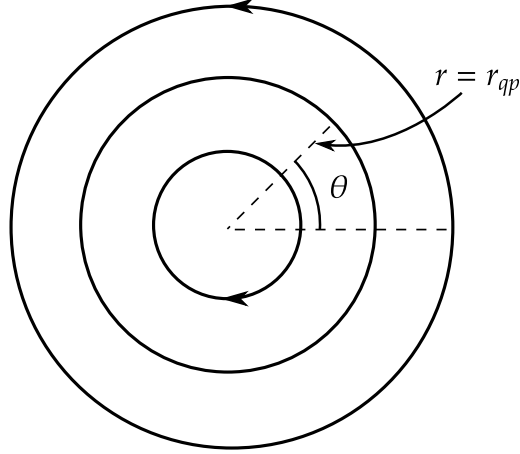
Figure 10: Moser twist map with $\frac{d\xi(r)}{dr}\Big|_{r=r_{pq}} > 0$ twists points on circles with $r > r_{pq}$ counterclockwise and $r < r_{pq}$ clockwise. Adapted from Ref. [63].

the vicinity of $r = r_{pq}$ (similar reasoning holds for $\frac{d\xi(r)}{dr} < 0$). With this choice, T^q maps points on a circle with $r > r_{pq}$ counterclockwise (increasing θ) and points on a circle with $r < r_{pq}$ clockwise (decreasing θ) as in Fig. 10.

For sufficiently small perturbations ϵ, the system will have some areas $r > r_{pq}$ and $r < r_{pq}$ that the perturbed map T_ϵ^q still twists (maps in the angular direction) in the same direction as in the unperturbed case. This is due to assuming the perturbation to be continuous in ϵ, i.e., we get regular dynamics in the limit $\epsilon \to 0$. Due to continuity, we find that for each value of θ there exists some $r = r_\epsilon(\theta)$ that is mapped purely in the radial direction by T_ϵ^q, i.e,

$$T_\epsilon^q(r_\epsilon(\theta), \theta) = (r_\epsilon'(\theta), \theta)$$

as shown in Fig. 11 where the arrows indicate the direction of the mapping.

The map T_ϵ results from a cross section of a flow in a Hamiltonian system. Therefore the map T_ϵ and all its iterations are symplectic [11]. All symplectic maps preserve the area, and so the mapping of the curve $r_\epsilon(\theta)$, i.e., $T_\epsilon^q(r_\epsilon(\theta), \theta)$, will intersect the original curve at even number of points as visualized in Fig. 11. These intersection points are the fixed points of T_ϵ^q.

By considering both the direction of the twist and the direction of the radial mapping near the intersections, as shown by arrows in Fig. 12, we find that the fixed points of T_ϵ^q are alternating hyperbolic and elliptic fixed points. Hyperbolic points are those that repel the "flow" of the map and elliptic points are those with a stable neighborhood.

To find out the number of fixed points, we observe – following Ref. [63] – that if there is one fixed point (r_f, θ_f), then also $T_\epsilon(r_f, \theta_f), \ldots, T_\epsilon^{n-1}(r_f, \theta_f)$ are fixed points of T_ϵ^q since, e.g.,

$$T_\epsilon^q\left[T_\epsilon(r_f, \theta_f)\right] = T_\epsilon\left[T_\epsilon^q(r_f, \theta_f)\right] = T_\epsilon(r_f, \theta_f). \tag{3.35}$$

31
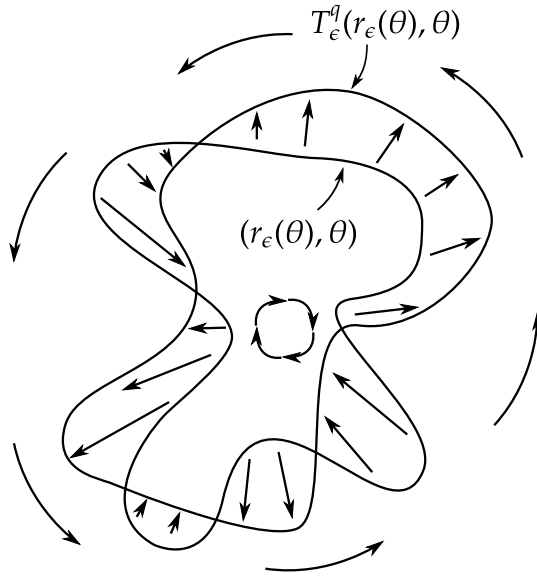
Figure 11: In the perturbed twist map there exists a curve $(r_\epsilon(\theta), \theta)$ which is mapped purely in the radial direction. Adapted from Ref. [63].

This way, we get at least q distinct fixed points of T_ϵ. As already mentioned above, the fixed points come in pairs of elliptic and hyperbolic points. The previous construction does not map elliptic fixed points to hyperbolic fixed points because they represent totally different kinds of trajectories (they are topologically inequivalent) [63]. We conclude that we get at least $2q$ (or some multiple of it) fixed points.

An elliptic fixed point of T_ϵ^q is always surrounded by closed curves that are invariant under T_ϵ^q as proven by Moser [63,66]. It turns out that the neighborhood of an elliptic fixed point behaves like a perturbed integrable system: Some curves remain and some curves are destroyed giving arise to yet a new set of elliptic and hyperbolic fixed points of some higher iterate of the Poincaré map, $(T_\epsilon^q)^m$. The structure repeats *ad infinitum*, i.e., the neighborhood of KAM islands is structurally self-similar[12] as can, to some extent, be seen, e.g., in Fig. 13 for elliptic billiards in a magnetic field.

The above consideration shows that the rational tori are destroyed giving arise to a self-similar structure in the phase space. However, the fate of the irrational tori is also answered by the KAM theorem stating that a torus with the frequency vector ω is preserved if for all nonzero integer vectors m

$$|m \cdot \omega| > K(\omega)|m|^{-(n+1)} \tag{3.36}$$

holds, where $|c| = |c_1| + \cdots + |c_n|$ is the taxicap norm [11]. Here $K(\omega)$ is some function of which not much is typically known for a given system. This can be thought as a condition for sufficient irrationality of a torus to survive the perturbation.

To give an idea on how common the surviving and destroyed tori are, we first

---

[12]Self-similar in the sense that the characteristics remain the same regardless of how small details we are looking at, not in a strict mathematical sense.
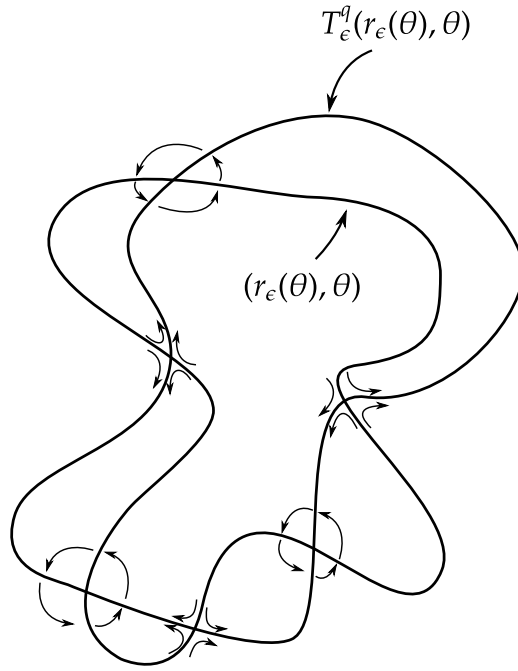
Figure 12: Fixed points of the perturbed map T_ϵ^q can be found at the intersection points of the curve $r_\epsilon(\theta)$, which is mapped purely radially, and its image. Furthermore, one can easily sketch the "flow" of the map near the fixed points by considering the radial mapping direction and the twist directions around $r_\epsilon(\theta)$ in Fig. 11. Adapted from Ref. [63].

point out that rational tori, which are destroyed, are dense in the phase space of the unperturbed Hamiltonian [11]. Secondly, the tori that do not satisfy the KAM condition form a set of zero Lebesque measure in ω-space [11]. This means that preserved tori are also quite common [11].

Generally speaking, a Poincaré map $T : \mathbb{R}^2 \to \mathbb{R}^2$ might have yet another kind of fixed point in addition to elliptic and hyperbolic fixed points. Naturally, we can attempt to analyze the stability of a fixed point $x \in \mathbb{R}^2$ by propagating a small perturbation in the linearized dynamics as done by Berry for billiard systems [67]. Let $x_1, \ldots, x_q$ be a q-cycle, i.e., $x_n = Tx_{n-1}$ and $x_q = x_1$. Consider a small perturbation ξ_1 that evolves according to (calculation similar compared to Sec. 3.1)

$$\xi_q = DT\big|_{x_{q-1}} \cdots DT\big|_{x_2} DT\big|_{x_1} \xi_1 \equiv DT^q \xi_1, \tag{3.37}$$

where DT^q is a linear map. By assuming that it has two linearly independent eigenvectors $e_\pm$ with the corresponding eigenvalues $\lambda_\pm$, we can expand the initial perturbation as a linear combination of the eigenvectors,

$$\xi_q = A\lambda_+ e_+ + B\lambda_- e_-. \tag{3.38}$$

The jth iteration of the linearized version of the map T^q evolves the perturbation to

$$\xi_{qj} = A\lambda_+^j e_+ + B\lambda_-^j e_-, \tag{3.39}$$

i.e., the eigenvalues of DT^q determine the stability of the fixed point. The eigenvalues of a 2×2 matrix

$$A = \begin{bmatrix} a & b \\ c & d \end{bmatrix}$$

can be easily solved to yield

$$\det(A - \lambda \mathbf{1}_{2\times2}) = 0$$
$$\lambda^2 - \underbrace{(a + d)}_{=\operatorname{Tr}A} \lambda + \underbrace{(ad - cb)}_{=\det A} = 0$$

$$\lambda_\pm = \frac{1}{2}\left[\operatorname{Tr}A \pm \sqrt{(\operatorname{Tr}A)^2 - 4\det A}\right].$$

Since the map T is symplectic and thus area-preserving, we have $\det(DT^q)=1$ [11]. In addition, the eigenvalues of a symplectic map are reciprocal to each other [68].

In conclusion, the eigenvalues of DT^q are

$$\lambda_\pm = \frac{1}{2}\left[\operatorname{Tr}DT^q \pm \sqrt{(\operatorname{Tr}DT^q)^2 - 4}\right]. \tag{3.40}$$

This result gives us three different scenarios:

1. If $|\operatorname{Tr}DT^q| < 2$, the eigenvalues are complex conjugates of each other, and we can write $\lambda_\pm^j = e^{\pm ij\theta}$ for some $\theta \in [0, 2\pi[$. The perturbations oscillate, but since they are bounded, the fixed point is stable. Such fixed points correspond to *elliptic fixed points* as discussed above.

2. If $|\operatorname{Tr}DT^q| > 2$, the eigenvalues are real (and reciprocal as mentioned earlier), and we get $|\lambda_\pm|^j = e^{\pm j\gamma}$ for some $\gamma \in \mathbb{R}$. The absolute value of the larger eigenvalue is greater than one, i.e. the flow of the map diverges in this direction whereas the absolute value of the other eigenvalue is smaller than one, i.e., the map flow is contracting in this direction. This kind of an unstable fixed point is called a *hyperbolic fixed point*.

3. $|\operatorname{Tr}DT^q| = 2$ is a marginal case where there is only one distinct eigenvalue ± 1. In linearized dynamics $\lambda = -1$ corresponds to the trajectory oscillating between two points on the opposite sides of the fixed point. $\lambda = 1$ in the other hand corresponds to a dense set of fixed points near the original fixed point. These fixed points are called *parabolic*.

In two-dimensional maps, the results of the linear stability analysis are guaranteed to hold also for the nonlinear dynamics. For hyperbolic fixed points this is guaranteed by the Hartman-Grobman theorem [69] and for elliptic fixed points by the existence of invariant curves around them according to KAM theory. Should the linearized dynamics yield a parabolic fixed point, the nature of the fixed point in the nonlinear dynamics can not be deduced just by the linear analysis.

To summarize, in a perturbed system we have hyperbolic sets originating from rational tori and irrational tori that do not satisfy the KAM condition. In addition
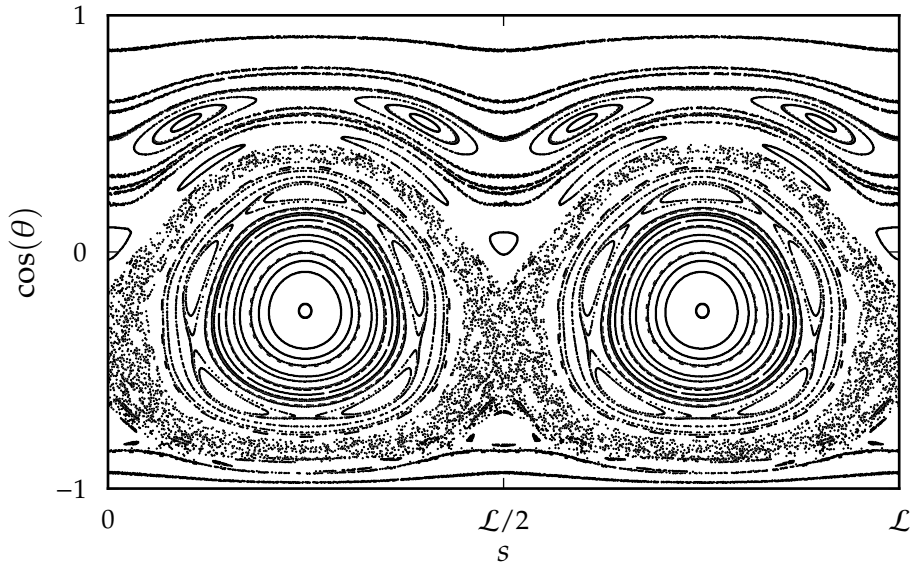
Figure 13: A numerically calculated Poincaré section of elliptic billiards in a magnetic field with semi-minor and -major axes 1 and 3/4, and the Larmor radius $r_{LR} = 3$. The Poincaré section shows several elliptic KAM islands (connected families of closed curves), parabolic KAM-islands (bottom and topmost islands), and chaotic sea(s) (irregularly filled regions). This system has been extensively studied – including the first calculation of the Poincaré section shown here – in Ref. [51]. Here the Poincaré section is parameterized by the arc length s counter-clockwise along the boundary of length $\mathcal{L}$ and $\cos(\theta)$, cosine of the collision angle.

to these hyperbolic sets, we also have connected sets of surviving KAM tori, *KAM islands*, which give arise to regular dynamics in the system. Such a system is called *mixed* in the sense that its phase space has both hyperbolic and regular components. As ϵ is increased, i.e., with a stronger perturbation, more and more of the KAM tori are destroyed until we are left with only the hyperbolic component of the phase space.

An example of a numerically calculated Poincaré section of a mixed system is shown in Fig. 13. The regular component of the system consists of (1) elliptic KAM islands, i.e., sets of closed invariant curves caused by an elliptic periodic orbit as described by the KAM theory, and (2) parabolic KAM islands, i.e., sets of marginally stable curves. The chaotic component, i.e., the chaotic sea is seen as irregularly filled regions. In the outskirts of the large elliptic islands, the remnants of the destroyed tori can be seen forming new elliptic islands.

We point out that in two-dimensional maps the KAM tori separate the phase space into parts inside the tori and outside the tori. This, however, is not the case in higher-dimensional systems [11].

3.2.4 Transition to full chaos

As the strength of the perturbation, ϵ, is increased, more and more of the KAM tori are destroyed. When there is still a large regular component in the phase space, the dynamics of the trajectories in the chaotic sea are restricted. As mentioned above, in low-dimensional systems it may even be that the chaotic seas are isolated by regular tori so that the chaotic trajectories are bounded to a small portion of the phase space [11]. In such a mixed system the regular dynamics dominate the long-time behavior, and we may consider the bounded chaotic seas as *weakly chaotic*.

At some point all the KAM tori are destroyed and the system becomes *strongly chaotic*, i.e., the phase space $\mathbb{P}$ becomes hyperbolic. Even if the system is strongly chaotic, there are still several different aspects related to complete chaoticity.

First, the system might be ergodic, which means that trajectories visit arbitrarily close to any point in phase space in such a way that all temporal averages may be replaced by spatial averages (with respect to a certain measure) [11]. One important consequence of ergodicity is that for almost all initial conditions the Lyapunov exponents are the same [11, 55].

Second, the system might be mixing. An area-preserving map T defined on a compact region S is said to be (strongly) mixing in S if, and only if, for any two subsets $U, V \subset S$ of nonzero measure, the ratio of their measures can be written as [70]

$$\frac{\mu(V)}{\mu(S)} = \lim_{k \to \infty} \frac{\mu(U \cap T^k(V))}{\mu(U)}. \tag{3.41}$$

This definition means that a subset V gets evenly distributed in S as $k \to \infty$ so that after the *mixing* with T^k, every subset W contains the same amount of the image of V, $T^k(V)$, as there was originally compared to the entire set S. Mixing is a stronger property than ergodicity in the sense that mixing implies ergodicity but not vice versa [11].

There are even more properties that can be attributed to chaotic systems, but the above two will suffice in order to give an idea that even in a strongly chaotic system there might be different degrees of chaoticity.

3.3 Summary of terminology

The following list briefly summarizes the terminology introduced so far.

Invariant set
> A set which is invariant under time evolution of the system.

Lyapunov exponent
> Two initially close chaotic trajectories diverge exponentially, and the exponent is called the Lyapunov exponent.

Hyperbolic orbit
> An orbit that has at least one positive Lyapunov exponent.

Hyperbolic set
> An invariant set where almost all orbits are hyperbolic. Hyperbolic sets are also called chaotic seas.

KAM torus
> A dynamically regular structure, diffeomorphic with a torus.

KAM island
> A dynamically regular set formed by KAM tori.

Elliptic island
> A KAM island formed due to an elliptic periodic orbit.

Parabolic island
> A KAM island composed of marginally stable (parabolic) orbits.

Regular system
> A system all orbits of which are integrable (regular).

Mixed system
> A system whose phase space has both KAM islands and chaotic seas.

Strongly chaotic system
> A system whose entire phase space is hyperbolic except perhaps for a set of zero measure.

(a) Sinai billiard   (b) Bunimovich stadium

(c) Bunimovich mushroom
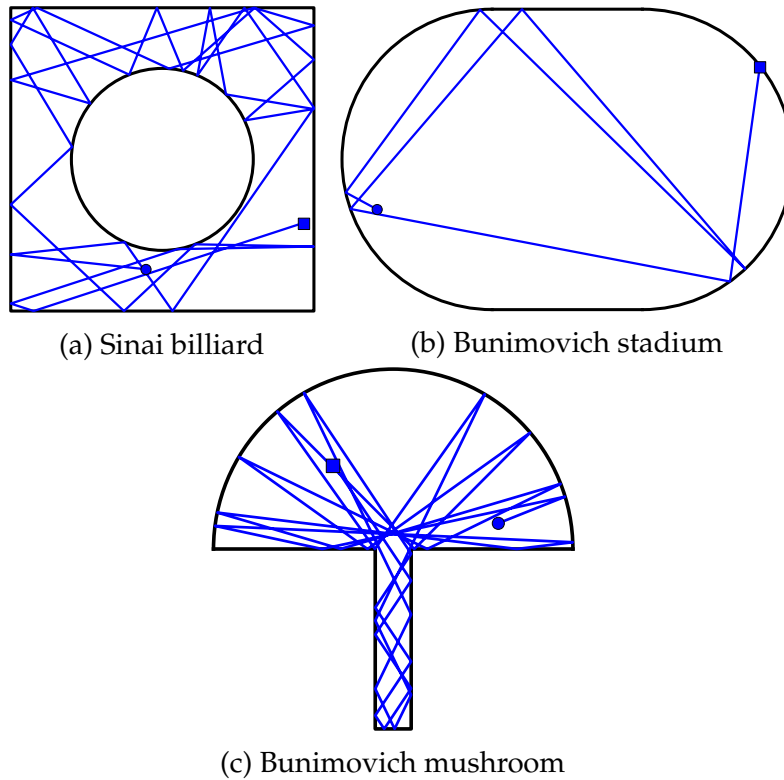
Figure 14: Different famous billiard systems.

3.4 Examples of billiards

In single-particle billiards the particle moves (typically) in straight lines between elastic collisions with the boundary, so one might be tempted to think that the motion will always be regular since between the collisions two trajectories will separate linearly in time. This, however, is not the case since the boundary collisions might diverge nearby trajectories.

The Sinai billiards is a single-particle billiards consisting of a rectangular table with a circular scatterer [Fig. 14(a)]. The table is convex, and it has been proven that the system is hyperbolic and ergodic [71,72]. The hyperbolicity of this billiards is easy to understand since the circular scatterer disperses nearby trajectories. Later it was shown that there might also be *concave* tables that are hyperbolic. For example, the Bunimovich stadium [Fig. 14(b)] is hyperbolic and ergodic [73,74].

As a generalization of the stadium, it is possible to introduce the Bunimovich mushroom [Fig. 14(c)]. The mushroom has a mixed phase space with both a chaotic sea and a single KAM island [16].

3.5 Stickiness

Stickiness is a phenomenon where a chaotic trajectory gets stuck for long period of time in some region of the chaotic sea, called a *sticky region*. There are many origins for a sticky region in a chaotic sea. For example, the phase space could be mixed and the region near the boundary between KAM islands and a chaotic sea might become sticky. This section mostly summarizes the main concepts of Ref. [75].

Stickiness manifests itself, for example, as nearly zero finite-time Lyapunov exponents, in temporal correlations, and survival probabilities of open systems. Survival probabilities of chaotic seas with no sticky regions decay exponentially whereas in the presence of sticky regions, they obtain power-law asymptotics. These effects will be explained further in Sec. 3.6.

Stickiness can be divided into two classes, external stickiness due to KAM tori and internal stickiness, i.e., stickiness without KAM tori.

As an example of internal stickiness, consider a stadium billiards shown in Fig. 14(b). The stadium is a hyperbolic system, i.e., the phase space is free of KAM tori. It has, however, a continuous family of marginally unstable periodic orbits (CFMUPO). In case of stadium, they are the orbits bouncing between the parallel lines of the boundary (often called bouncing-ball orbits). The CFMUPO forms an invariant set of zero measure. A chaotic orbit might come arbitrarily close to some of these MUPOs thus spending a long time bouncing between the parallel lines. In other words, the region around the CFMUPO is a sticky region. This sticky region is caused not by KAM tori but by the CFMUPO, which is an internal structure of the chaotic sea.

We can give a more exact definition of internally sticky regions: A sticky region is internally sticky if it is due to an invariant subset of positive codimension (i.e. the dimension of the subset is smaller than that of the original phase space) which resides completely inside a chaotic sea.

External stickiness, on the other hand, is due to the boundary between KAM islands and chaotic seas. However, not all KAM islands cause stickiness in the nearby chaotic seas. External stickiness is intuitively clear: the dynamics of the chaotic sea in the vicinity of the border with a KAM island are only slightly hyperbolic since orbits that get stuck in the sticky set tend to stay close to the KAM islands. This can be seen for example in Fig. 15. The upper panel shows a sticky orbit as red dots in the Poincaré section section together with the structure of the rest of the phase space and the bottom panel depicts the sticky orbit in coordinate space.

Elliptic KAM islands are typically sticky and parabolic KAM islands are typically nonsticky. However, elliptic islands are nonsticky if the boundary is an unstable invariant set that acts as a separatix between the regular dynamics of the KAM island and the chaotic dynamics of the sea.
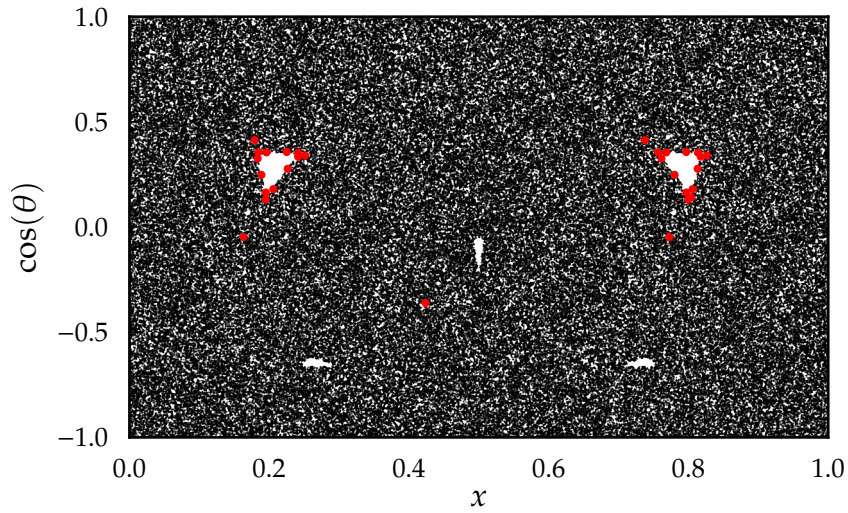
(a) Phase space representation of a sticky trajectory (red dots) along with the chaotic sea of the system (black dots).
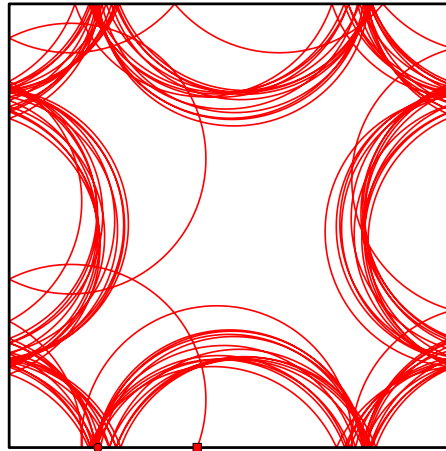
(b) Coordinate space representation of the sticky trajectory in Fig. 15(a).

Figure 15: A sticky trajectory in magnetic square billiards with the Larmor radius $r_{\mathrm{LR}} = 0.305$ and lengths of the sides $L = 1$. In the Poincaré section in (a), the collisions with the lower part of the boundary are shown, labeled by the x-coordinate of the collision point and $\cos(\theta)$, cosine of the collision angle.

3.6 Open systems

3.6.1 Overview

We can always open up a closed Hamiltonian system by introducing a hole $\mathbb{I}$ in the phase space $\mathbb{P}$ via which the particles can escape from the system. This is an important field of study since all experimental setups are open systems at least due to the act of observation. In Hamiltonian systems, particularly in billiards, the question is how the survival probability or equivalently the escape-time distribution through the hole depends on the structure of the phase space of the open system. Furthermore, what is the relation between the phase space of the open system and the corresponding closed system? The following introduction is mostly based on the review by Altmann et al. [76].

We define the escape for discrete mappings so that if at nth iteration a particle is at the hole $\mathbb{I}$, then in $(n + 1)$th iteration it will escape.

The quantities we are mostly interested are the survival probability and the escape-time distribution. If we set a normalized initial density $\rho(\mathbf{r}, t = 0)$ in the phase space and at some time t look at the phase space density $\rho(\mathbf{r}, t)$ that has not yet escaped the system, the survival probability is defined as the integrated density inside the system,

$$P_s(t) = \int_{\mathbb{P}} \rho(\mathbf{r}, t)\, d\mathbf{r}. \tag{3.42}$$

The escape-time distribution $P_e(t)\, dt$ on the other hand gives the portion of trajectories that leave the system in an infinitesimal time interval by

$$P_e(t) = -\frac{dP_s(t)}{dt}. \tag{3.43}$$

Numerically the distributions can be estimated by first distributing a large number N_0 of initial points randomly according to the density $\rho(\mathbf{r}, t = 0)$. To calculate the survival probability, one propagates the trajectories and compares the number of trajectories that have not escaped up to time t, i.e., $N(t)$, to the size of the initial ensemble [77],

$$P_s(t) = \frac{N(t)}{N_0}. \tag{3.44}$$

To get the escape-time distribution, one compares the number of escaping trajectories in a short time interval $[t - \delta t/2, t + \delta t/2[$,

$$\Delta N(t) = N(t - \delta t/2) - N(t + \delta t/2),$$

where δt is the size of the histogram bin, to the size of the initial ensemble, i.e.,

$$P_e(t) = \frac{\Delta N(t)}{N_0}. \tag{3.45}$$

Lifetime of a trajectory is defined as the time it takes from the initial point for

the trajectory to escape the system. In the following we often speak of time and long-lived trajectories but actually refer to the number of iterations under some discrete-time dynamics.

A structure of the phase space of a closed system is typically also found in the corresponding open system as long as the structure does not vanish very quickly due to the hole. As the size of the hole goes to zero, we can actually explain the survival probability of the open system in terms of the properties of the closed system [76,78].

3.6.2 Escape in chaotic systems

We first describe the properties of the survival probability in fully hyperbolic systems, i.e., in systems without sticky regions. The survival probability is fully exponential after some initial period [77].

The essential structure of the chaotic phase space that determines the exponential behavior of the survival probability is the so called *chaotic saddle* that is the invariant set of trajectories which do not leave the system for $t \to \pm\infty$. The saddle is very sparse in phase space [76], since, as one might expect, chaotic orbits typically travel everywhere in the phase space thus leaving it at some point.

There are two invariant sets in the phase space which can be connected to the saddle, namely its stable and unstable manifolds. The stable manifold is the set of trajectories that approach the saddle as $t \to \infty$. The unstable manifold is the set of trajectories that approach the saddle as $t \to -\infty$. The saddle determines the long-time behavior of the survival probability as long as the initial density overlaps with the manifolds sufficiently [76].

To gain insight into the long lived trajectories and the invariant sets, we introduce the sprinkler method, explained in Ref. [77], that can be used to numerically calculate the saddle and its manifolds. Suppose we set up a large number N_0 of initial points randomly in the phase space $\mathbb{P}$. Then we propagate these trajectories for a long time t^* (many times longer than the typical lifetime of a trajectory) and study only the trajectories that have not escaped the system.

These trajectories stay near the saddle for a long time during the considered period , so especially at $t \approx t^*/2$ we have points near the saddle [77]. The initial points of these trajectories are close the the stable manifold since they come close to the saddle during the propagation. The closer the initial points are to the stable manifold the longer lifetime the trajectories have. Thus by increasing the propagation time t^*, we get a better approximation for the stable manifold by cutting away trajectories that are further away from the stable manifold.

Of these long lived trajectories most will still leave the system if we continued the propagation. They would, however, stay in the system for a long time in the backward dynamics, and thus the end points of the trajectories are close to the unstable manifold.

To obtain mathematical formulation for the escape in fully chaotic systems and to understand some subtle differences between the Poincaré map and the true-time

map, we now make some analytical considerations for the escape process of fully hyperbolic systems as in Refs. [59,76,77].

Consider discrete dynamics given by the map T, which can be, e.g., a Poincaré map. Following Ref. [79], we define $P_n(A)$ to be the probability that for a randomly chosen $x \in \mathbb{P}$ the image $T^n(x) \in A$ given that x has not escaped the system up to n iterations. The limiting measure

$$\mu_c(A) = \lim_{n \to \infty} \frac{P_n(A)}{P_n(\mathbb{P})} \tag{3.46}$$

is called the conditionally invariant measure (c-measure).[13] The density ρ_c of the c-measure μ_c ($d\mu_c = \rho_c \, dx$) is concentrated on the unstable manifold since, as discussed above, most trajectories are still about to leave the system, i.e., they are in the vicinity of the unstable manifold.

To understand the meaning of the c-measure, consider the following. Assuming we have initially N_0 trajectories in the ensemble and remembering the escape process is exponential, the number of trajectories that have not escaped is $N(n) \approx N_0 e^{-\gamma n}$. The number of trajectories that escape at $(n+1)$th iteration is $N(n) - N(n+1) \approx N_0 e^{-\gamma n}(1 - e^{-\gamma})$, and the corresponding escape probability is given by

$$P_e(n) \approx e^{-\gamma n}(1 - e^{-\gamma}). \tag{3.47}$$

The trajectories that escape are at $(n+1)$th iteration are in the hole I at the nth iteration, and the probability for a trajectory to be in the leak $\mathbb{I}$ is given by $\mu_n(I) \approx \mu_c(I)$ for sufficiently large n. We would thus expect that

$$\frac{\mu_c(I)}{\mu_c(\mathbb{P})} N(n) \tag{3.48}$$

trajectories escape at the $(n+1)$th iteration. If we normalize the measure so that $\mu_c(\mathbb{P}) = 1$, we get

$$e^{-\gamma} \approx 1 - \mu_c(I). \tag{3.49}$$

We see that the c-measure and the corresponding density tell us how the particles that will escape the system are distributed along the unstable manifold.

For true-time dynamics, the situation changes a bit although at first glance everything looks the same. Consider for example a fully hyperbolic billiards with a leak I on the boundary. Let us denote the c-measure of the true time map also by μ_c.[14] The average time between two collisions in the billiards for trajectories which are about to escape is given by

$$\langle t_{\text{coll}} \rangle_c \equiv \int_{\mathbb{P}_r} \tau(x) \, d\mu_c, \tag{3.50}$$

---

[13]For our purposes it is not necessary to delve deeper into meaning of *conditional invariance*. For more details see, e.g., Ref. [77].

[14]Definition: $P_t(A)$ is the probability that $\phi^t(x) \in A$ given that x has not escaped the system up to time t. Then $\mu_c = \lim_{t \to \infty} \frac{P_t(A)}{P_t(\mathbb{P})}$. Here $\phi^t(x)$ denotes the time-evolution of the system.

where the integral is taken over the natural Poincaré section on the boundary and $\tau(x)$ gives the time to the next collision.

The relation between the number of collisions n and the time t is given by

$$n \approx \frac{t}{\langle t_{\text{coll}} \rangle_c}. \tag{3.51}$$

Trajectories can escape only at collisions so as above we get

$$P_e(n) \approx e^{-\gamma n}(1 - e^{-\gamma}), \tag{3.52}$$

and in the time domain

$$P_e(t) \approx e^{-\gamma \frac{t}{\langle t_{\text{coll}} \rangle_c}}(1 - e^{-\gamma}), \tag{3.53}$$

where $e^{-\gamma} = 1 - \mu_c(I)$ as above but now with respect to the c-measure of the true-time map.

The difference between the true-time dynamics and the discrete dynamics given by the Poincaré map is easily understood by an example given by the stadium billiards [76].[15] The Poincaré map has arbitrarily long orbits with respect to n in the circular caps. Thus they contribute to the discrete escape-rate distribution via the c-measure of the Poincaré map. The c-measure of the true-time map, however, has a totally different contribution from the same trajectories, since the actual time the trajectory collides with the cap is always bounded. With this in mind, one should always be careful when describing the escape-time distribution within the Poincaré map since the c-measures may be drastically different, and thus, the escape-time distributions of the two representations might be totally different as well [59]. This also applies to sticky systems.

3.6.3 Escape in sticky systems

Stickiness of a chaotic sea modifies the survival probability. Suppose for simplicity that the leak I is fully inside a chaotic sea, i.e., it does not extend to possible KAM islands. If the initial density is nonzero only in the chaotic sea, then the survival probability has the following structure [76]:

There is an initial period of time, up to t_s, during which the survival probability is affected by system-specific properties and the distribution of initial points. After this initial period, there might be a period during which chaotic trajectories do not typically enter a sticky region before leaving the system. We can thus expect based on the results in the previous section that the survival probability is exponential. After the (possible) exponential period up to t_z, the sticky region begins to influence the dynamics giving a power law tail for the asymptotics. To summarize,

$$P_s(t) \sim \begin{cases} \text{irregular,} & t < t_s \\ e^{-\gamma t,} & t_s < t < t_z \\ ae^{-\gamma t} + b(\gamma t)^{-z}, & t_z < t. \end{cases} \tag{3.54}$$

---

[15]Although the stadium is not fully hyperbolic, it is an excellent example to show the difference between the true-time map and the Poincaré map.

Due to the form of the survival probability, one sees that the chaotic saddle is divided into a hyperbolic component responsible for the exponentiality and a nonhyperbolic component due to the stickiness giving arise to the power-law asymptotics [76].

Regular dynamics give rise to power-law asymptotics so that $P_s(t) \sim 1/t$ [76]. The dynamics within the KAM tori are regular, and the survival probability obeys power-law asymptotics [76]. If the leak intersects both a chaotic and a regular component and the initial distribution also spreads over to the KAM tori one sees an overall power-law behavior after some time t_p in addition to the above $P_s(t)$ for sticky chaotic systems [80].

3.7 Interacting many-body billiards

When motivated by realistic systems, it is important to consider the effects of the interparticle interactions in many-body billiards. To set the context of the studies of this thesis more thoroughly, we briefly review the some of the previous activity on interacting many-body billiards.

What has been studied previously is typically few-particle billiards interacting either via elastic hard-ball collisions or by the Yukawa-interaction,

$$V(\boldsymbol{r}_1, \boldsymbol{r}_2) = \frac{e^{-\lambda \|\boldsymbol{r}_1 - \boldsymbol{r}_2\|}}{\|\boldsymbol{r}_1 - \boldsymbol{r}_2\|}. \tag{3.55}$$

Among one-dimensional systems, two-particle billiards with Yukawa interactions typically show a mixed phase space and generally nonergodic behavior with different ratios of the particle masses and range parameters λ of the Yukawa-interaction [24–26, 28]. The Poincaré section of two-particles in one dimensional billiards interacting via the Coulomb interaction shown in Fig. 16 is qualitatively similar to the Yukawa-interacting system studied in Ref. [26]. The figures shows several KAM-islands and a chaotic sea. Details on the calculation of this figure and a more detailed comparison between the Poincaré sections of the one-dimensional Yukawa and Coulomb-interacting systems are given in Appx. A.

Two-particle billiards in two-dimensional tables have been previously studied with both hard-ball and Yukawa-interactions. Hard-ball billiards have been studied in rectangular [21, 23], circular [21], and mushroom billiards [21]. These hard-ball billiards can show regular characteristics despite being usually chaotic [21]. With Yukawa interactions, the systems have been studied, e.g., by analyzing the maximal Lyapunov exponent [27], cross sections of the phase space [27], and the distribution of the finite time Lyapunov exponents [28] with different ranges of the length-parameter λ and mass ratios. Some traces of stickiness has been found in the two-particle circular billiards both with Yukawa and Coulomb-interactions [28].

Circular two-particle billiards have also been studied quantum-mechanically with Yukawa-interactions [81] and, more relevantly to our studies, with Coulomb-interactions [82].
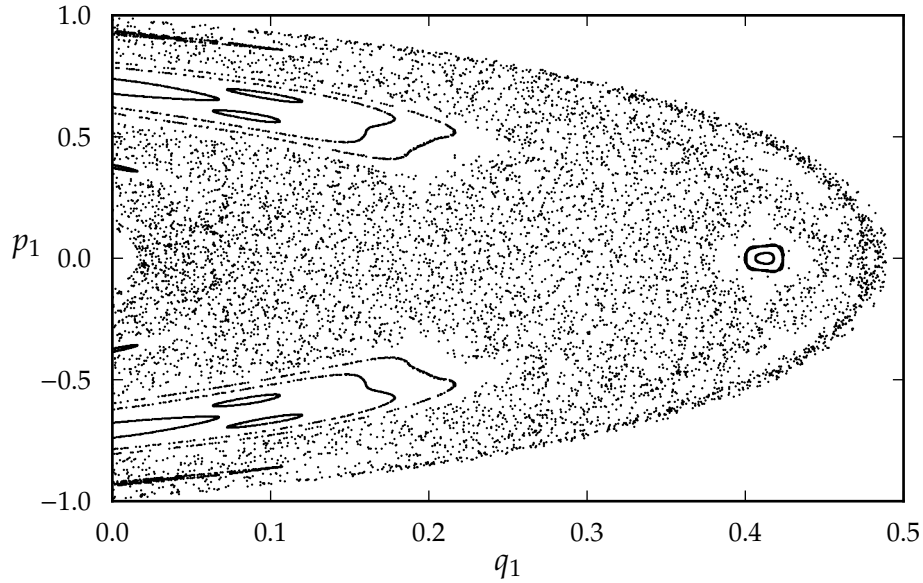
Figure 16: Poincaré section of one-dimensional two-particle Coulomb-interacting billiards in the intermediate interaction range (for details see Sec. A). The system has a mixed phase space that is qualitatively similar to the corresponding Yukawa-interacting system.

Our studies focus on Coulomb-interacting many-body billiards with different interaction strengths. With Coulomb-interactions, to best of our knowledge, only oscillators [33–37] have been studied in addition to periodic systems [38–40] and rectangular billiards in magnetic field [41]. Application vice, the Coulomb-interacting systems are a natural extension to previous studies on two-dimensional Yukawa-interacting billiards, where only a few remarks have been made in the Coulombic limit [28].

4 Numerical methods

4.1 Hamiltonian

In this thesis we are interested in billiard systems, especially Coulomb interacting many-particle billiards without external potentials except for the billiard boundary. The Lagrangian is given by

$$L = \sum_i \frac{1}{2} m_e v_i^2 - \sum_{i<j} \frac{q_e^2}{4\pi\epsilon_0} \frac{1}{\|r_i - r_j\|},$$ (4.1)

where r_i and v_i are the position and velocity of the ith particle, m_e and q_e the mass and the charge of the particles, and in the sums the indices i and j run over all the particles.

By introducing Hartree atomic units (a.u.), such that $q_e = m_e = \frac{1}{4\pi\epsilon_0} = 1$, the Lagrangian reduces to

$$L = \frac{1}{2} \sum_i v_i^2 - \sum_{i<j} \frac{1}{\|r_i - r_j\|}.$$ (4.2)

We now transform the formulation into Hamiltonian formalism. By choosing the generalized coordinates for the ith particle, q_i, as the cartesian coordinates r_i we get for the generalized momentum

$$p_i = \frac{\partial L}{\partial \dot{r}_i} = v_i,$$ (4.3)

i.e., the generalized momentum corresponds to the velocity in the cartesian frame. From now on we can use (r_i, v_i) as the parametrization of the phase space $\mathbb{P}$.

The Hamiltonian yielding the equations of motion between the collisions is obtained from Eq. (2.14),

$$H = \frac{1}{2} \sum_i v_i^2 + \sum_{i<j} \frac{1}{\|r_i - r_j\|}.$$ (4.4)

In order to simplify the treatment of geometrically similar systems with different length and/or energy scales, we show that all systems with Hamiltonians of form

$$H(q, p, t) = \frac{1}{2} \sum_i p_i^2 + \sum_{i<j} \frac{1}{\|q_i - q_j\|}$$ (4.5)

are reducible to a Hamiltonian system with a fixed length scale described by coordinates (Q, P, T) of the extended phase space and the Hamiltonian

$$K(Q, P, T) = \frac{1}{2} \sum_i P_i^2 + \sum_{i<j} \frac{\alpha}{\|Q_i - Q_j\|},$$ (4.6)

where $\alpha \in \mathbb{R}$ is a scaling parameter that is defined in the following.

We begin by a scale transformation of the original coordinates,

$$(\boldsymbol{q}_i, \boldsymbol{p}_i, t) \rightarrow (\boldsymbol{Q}_i = \gamma \boldsymbol{q}_i, \boldsymbol{P}_i = \beta^{1/2} \boldsymbol{p}_i, t). \tag{4.7}$$

The Hamiltonian, which yields the equations of motion for the new coordinates $(\boldsymbol{Q}_i, \boldsymbol{P}_i, t)$, is given by (2.41),

$$K(\boldsymbol{Q}_i, \boldsymbol{P}_i, t) = \beta^{1/2} \gamma H(\boldsymbol{q}_i, \boldsymbol{p}_i, t) = \frac{1}{2} \sum_i \beta^{-1/2} \gamma \boldsymbol{P}_i^2 + \sum_{i<j} \frac{\beta^{1/2} \gamma^2}{\|\boldsymbol{Q}_i - \boldsymbol{Q}_j\|}. \tag{4.8}$$

The equations of motion are obtained from Eqs. (2.17) and (2.18) yielding

$$\frac{d\boldsymbol{Q}_i}{dt} = \nabla_{\boldsymbol{P}_i} K = \beta^{-1/2} \gamma \boldsymbol{P}_i \tag{4.9}$$

$$\frac{d\boldsymbol{P}_i}{dt} = -\nabla_{\boldsymbol{Q}_i} K = -\sum_{j \neq i} \frac{\beta^{1/2} \gamma^2}{\|\boldsymbol{Q}_i - \boldsymbol{Q}_j\|^3} \left(\boldsymbol{Q}_i - \boldsymbol{Q}_j\right). \tag{4.10}$$

In order to further simplify these equations, we need to reparameterize time,

$$T(t) = \beta^{-1/2} \gamma t, \tag{4.11}$$

which gives us

$$\frac{d\boldsymbol{Q}_i}{dT} = \beta^{1/2} \gamma^{-1} \frac{d\boldsymbol{Q}_i}{dt} \stackrel{(4.9)}{=} \boldsymbol{P}_i \tag{4.12}$$

$$\frac{d\boldsymbol{P}_i}{dT} = \beta^{1/2} \gamma^{-1} \frac{d\boldsymbol{P}_i}{dt} \stackrel{(4.10)}{=} -\sum_{j \neq i} \frac{\beta \gamma}{\|\boldsymbol{Q}_i - \boldsymbol{Q}_j\|^3} \left(\boldsymbol{Q}_i - \boldsymbol{Q}_j\right). \tag{4.13}$$

Denoting $\alpha = \beta \gamma$, the Hamiltonian corresponding to equations of motion (4.12) and (4.13) is

$$K(\boldsymbol{Q}, \boldsymbol{P}, T) = \frac{1}{2} \sum_i \boldsymbol{P}_i^2 + \sum_{i<j} \frac{\alpha}{\|\boldsymbol{Q}_i - \boldsymbol{Q}_j\|}, \tag{4.14}$$

which can easily be checked with the Hamiltonian equations of motion in Eqs. (2.17) and (2.18).

In summary, we make a transformation in the extended phase space,

$$(\boldsymbol{q}, \boldsymbol{p}, t) \rightarrow (\boldsymbol{P} = \beta^{1/2} \boldsymbol{p}, \boldsymbol{Q} = \gamma \boldsymbol{q}, T = \beta^{-1/2} \gamma t), \tag{4.15}$$

which gives the Hamiltonian for the new variables $(\boldsymbol{Q}, \boldsymbol{P}, T)$,

$$K(\boldsymbol{Q}, \boldsymbol{P}, T) = \beta H(\boldsymbol{q}, \boldsymbol{p}, t) = \frac{1}{2} \sum_i \boldsymbol{P}_i^2 + \sum_{i<j} \frac{\alpha}{\|\boldsymbol{Q}_i - \boldsymbol{Q}_j\|}, \tag{4.16}$$

where $\alpha = \beta \gamma$.

As a concluding remark, all length and energy scales of geometrically similar

systems can be reduced to a single constant energy surface, e.g. $K(\mathbf{Q}, \mathbf{P}, T) = 1$, of the system with Hamiltonian $K(\mathbf{Q}, \mathbf{P}, T)$. Only the product of the scaling parameters β and γ, i.e. $\alpha = \beta\gamma$, is included as a parameter in the Hamiltonian.

In Appx. B we derive the scale transformations also for systems with vector and scalar potentials and demonstrate the transformations with an example.

4.2 Molecular dynamics with velocity Verlet algorithm

Above in Examples 3 and 4 in Sec. 2.5 we noticed that the Hamiltonian H is the generator of the time evolution, i.e., we can write any phase-space trajectory $z(t) = (q^a(t), p_a(t))$ as

$$z(t) = e^{t\{\cdot, H\}} z(0). \tag{4.17}$$

To obtain a symplectic integration scheme,[16] we need to find an approximation for $e^{t\{\cdot, H\}}$ in terms of canonical transformations as was done, e.g., in Ref. [83].

Let us first clarify the notation by denoting $\{\cdot, A\} \doteq D_A$ for any function A. Furthermore, we consider only the cases where the Hamiltonian separates into the kinetic energy T depending only on the generalized momenta and the potential energy V depending only on the generalized coordinates.

The propagator can be written as

$$e^{t D_H} = e^{t(D_T + D_V)}, \tag{4.18}$$

which we can rewrite using the symmetric Trotter formula [84] as

$$e^{t(D_T + D_V)} = \lim_{n \to \infty} \left[e^{\frac{t}{2n} D_V} e^{\frac{t}{n} D_T} e^{\frac{t}{2n} D_V} \right]^n. \tag{4.19}$$

By defining $\Delta t = t/n$ and letting $n < \infty$, we get an approximation

$$e^{\Delta t D_H} \approx e^{\frac{\Delta t}{2n} D_V} e^{\frac{\Delta t}{n} D_T} e^{\frac{\Delta t}{2n} D_V}. \tag{4.20}$$

The approximation is of second order in Δt as can be seen by expanding both sides as Taylor series,

$$e^{\Delta t D_H} = 1 + \Delta t D_H + \frac{1}{2} \Delta t^2 D_H^2 + O(\Delta t^3)$$

and

$$e^{\frac{\Delta t}{2n} D_V} e^{\frac{\Delta t}{n} D_T} e^{\frac{\Delta t}{2n} D_V} = (1 + \frac{1}{2}\Delta t D_V + \frac{1}{8}\Delta t^2 D_V^2 + \dots) \times$$

$$(1 + \Delta t D_T + \frac{1}{2}\Delta t^2 D_T^2 + \dots)(1 + \frac{1}{2}\Delta t D_V + \frac{1}{8}\Delta t^2 D_V^2 + \dots)$$

$$= 1 + \Delta t(D_V + D_T) + \frac{1}{2}\Delta t^2(D_V^2 + D_V D_T + D_T D_V + D_T^2) + O(\Delta t^3).$$

We see that these are equal up to the second order in Δt (but not up to the third

---

[16]Symplectic means that it preserves the essential properties of the phase space. For more details, see Ref. [11].

order as can easily be checked), i.e., we have a second-order propagation scheme.

The next step is to figure out how the operators $e^{\frac{\Delta t}{2n}D_V}$ and $e^{\frac{\Delta t}{n}D_T}$ operate on the phase space coordinates. D_T can be rewritten using the definition of the Poisson brackets (2.27) as

$$D_T = \{\cdot, T\} = \frac{\partial T}{\partial p_a}\frac{\partial}{\partial q^a} = \frac{\partial T}{\partial p_a}\{\cdot, p_a\}. \tag{4.21}$$

In our case we have $T = \frac{1}{2}\sum_i p_i^2$ so that $\frac{\partial T}{\partial p_a} = p_a$. Since momentum generates translation as in Example 2 in Sec. 2.5, we conclude that

$$e^{\Delta t D_T}\begin{pmatrix} q \\ p \end{pmatrix} = \begin{pmatrix} q + \Delta t p \\ p \end{pmatrix}, \tag{4.22}$$

where we have denoted the coordinates and the momentum in vector notation, i.e., $q = (q^1, q^2, \ldots, q^n)^T$ and $p = (p_1, p_2, \ldots, p_n)^T$.

Similarly we have $V = V(q)$ and $D_V = -\frac{\partial V}{\partial q^a}\{\cdot, q^a\}$ (from the definition of the Poisson brackets) leading to

$$e^{\frac{1}{2}\Delta t D_V}\begin{pmatrix} q \\ p \end{pmatrix} = \begin{pmatrix} q \\ p - \nabla_q V \frac{\Delta t}{2} \end{pmatrix}. \tag{4.23}$$

When combining these results we get the following propagation algorithm:

$$p(t + {}^{\Delta t}/_2) = p(t) - \nabla_q V(q(t))\frac{\Delta t}{2} \tag{4.24}$$

$$q(t + \Delta t) = q(t) + \Delta t p(t + {}^{\Delta t}/_2) \tag{4.25}$$

$$p(t + \Delta t) = p(t + {}^{\Delta t}/_2) - \nabla_q V(q(t + \Delta t))\frac{\Delta t}{2}. \tag{4.26}$$

They reduce even further to

$$q(t + \Delta t) = q + \Delta t p(t) - \frac{1}{2}\Delta t^2 \nabla_q V(q(t)) \tag{4.27}$$

$$p(t + \Delta t) = p - \frac{1}{2}\Delta t \left[\nabla_q V(q(t)) + \nabla_q V(q(t + \Delta t))\right]. \tag{4.28}$$

This is the classical velocity Verlet algorithm [85].

As seen from the derivation, the velocity Verlet algorithm corresponds to a canonical transformation, and it is thus a symplectic integration scheme. It can also be easily checked to be time-reversible. These two properties make it suitable for the study of chaotic phenomena.

In the following we will also consider two-dimensional billiards in magnetic fields. In such systems we do not directly propagate the Hamiltonian equations of motion, but instead we replace the velocity Verlet scheme by the one developed by Spreiter and Walter [86], which will explicitly incorporate the effect of the magnetic field into the formulas so that we can use arbitrarily strong magnetic fields without changing the time step. In their scheme the positions and velocities (in cartesian

frame) are calculated from

$$
\begin{aligned}
r_x(t + \Delta t) = r_x(t) &+ \frac{1}{\Omega} \left\{ v_x(t) \sin(\Omega \Delta t) - v_y(t) \left[\cos(\Omega \Delta t) - 1 \right] \right\} \\
&- \frac{1}{\Omega^2} \left\{ a_x^C(t) \left[\cos(\Omega \Delta t) - 1 \right] + a_y^C(t) \left[\sin(\Omega \Delta t) - \Omega \Delta t \right] \right\} + O(\Delta t^3)
\end{aligned}
$$

$$
\begin{aligned}
r_y(t + \Delta t) = r_y(t) &+ \frac{1}{\Omega} \left[v_y(t) \sin(\Omega \Delta t) + v_x(t) \left[\cos(\Omega \Delta t) - 1 \right] \right\} \\
&- \frac{1}{\Omega^2} \left[a_y^C(t) \left[\cos(\Omega \Delta t) - 1 \right] + a_x^C(t) \left[-\sin(\Omega \Delta t) + \Omega \Delta t \right] \right\} + O(\Delta t^3)
\end{aligned}
$$

$$
\begin{aligned}
v_x(t + \Delta t) = v_x(t) \cos(\Omega \Delta t) &+ v_y(t) \sin(\Omega \Delta t) + \frac{1}{\Omega} \left\{ -a_y^C(t) \left[\cos(\Omega \Delta t) - 1 \right] + a_x^C(t) \sin(\Omega \Delta t) \right\} \\
&- \frac{1}{\Omega^2} \left\{ \frac{a_x(t + \Delta t) - a_x^C(t)}{\Delta t} \left[\cos(\Omega \Delta t) - 1 \right] + \frac{a_y(t + \Delta t) - a_y^C(t)}{\Delta t} \left[\sin(\Omega \Delta t) - \Omega \Delta t \right] \right\} \\
&+ O(\Delta t^3)
\end{aligned}
$$

$$
\begin{aligned}
v_y(t + \Delta t) = v_y(t) \cos(\Omega \Delta t) &- v_x(t) \sin(\Omega \Delta t) + \frac{1}{\Omega} \left\{ a_x^C(t) \left[\cos(\Omega \Delta t) - 1 \right] + a_y^C(t) \sin(\Omega \Delta t) \right\} \\
&- \frac{1}{\Omega^2} \left\{ \frac{a_y(t + \Delta t) - a_y^C(t)}{\Delta t} \left[\cos(\Omega \Delta t) - 1 \right] + \frac{a_x(t + \Delta t) - a_x^C(t)}{\Delta t} \left[-\sin(\Omega \Delta t) + \Omega \Delta t \right] \right\} \\
&+ O(\Delta t^3).
\end{aligned}
$$

Here $\Omega = B$ is the magnetic field (or cyclotron frequency in SI units) and $\boldsymbol{a}^C = -\nabla_r V(\boldsymbol{r})$ is the velocity-independent part of the acceleration. Symplecticity of the scheme has not been explicitly proven, but we have found the method to be accurate when dealing with phase space properties. Also, the scheme has already been used previously to study interacting magnetic billiards [41].

4.3   Implementation – *Bill2d*

The software – *Bill2d* – used in the simulations of the billiards studied in this thesis is written in C++ following the object-oriented paradigm to offer speed, expandability, and easy-to-read source code. The implemented methods have been previously used in molecular dynamics simulations and are well suited for the study of interacting many-body billiards. We note that *Bill2d* has been already used to study, e.g., the dynamics of classical Wigner molecules [87] and two-particle circular billiards [88], and it is being further used to study diffusion in the soft Lorentz gas, which is a model system motivated by both the fundamentals of classical chaos and also recently fabricated artificial graphene-like structures [89–93].

The code has been separated into several C++-classes, each of which handles a specific part of the program. This makes the code *generic* in sense that it can be used for several different billiard tables, particle numbers, and interaction types. The modularity also allows for an easy construction of stripped binaries, e.g., for the calculation of statistical properties of the systems.

Bill2d uses several external libraries to handle tasks not related to the propagation. *Boost* C++ libraries are used to offer both command-line and configuration file interfaces. *GSL* libraries are used for special functions and random number generators. Data from simulations is saved using *HDF5*-libraries. All external libraries are wrapped within C++ classes to offer an easy-to-use application programming interface. Plotting and analysis tools are written using *Python* with the help of additional libraries such as *Numpy* and *Matplotlib*. Also, compilation and installation are automated using *GNU Autotools*.

The actual structure of the simulation package is rather complicated, and therefore a detailed discussion is omitted here. For a more extensive review on the implementation of *Bill2d*, we refer to Appx. D and our previous work in Ref. [94]. Here we describe only the relevant part of the program, i.e., the propagation procedure, which is demonstrated as a flowchart in Fig. 17.

First, we obtain the initial state of the system in the phase space by either manual user input or by randomly choosing the state. The energy of the initial state is always fixed. The random initial state is chosen by first randomizing the positions of the particles in the energetically allowed part of the configuration space. We then calculate the remaining energy and distribute it evenly among the particles. The directions of the velocities are randomized as well. Distributing the speeds evenly should not affect the results since the velocities are usually mixed shortly after the propagation has been started due to chaotic properties of many-particle billiards.

Next, we propagate the particles one time-step forward with one of the algorithms described above in Sec. 4.2. After each time-step, we check that the particles are inside the billiard table. If some of the particles have crossed the boundary, we (i) save the position, incoming velocity, and the collision angle if we are calculating Poincaré sections and (ii) apply the following scheme to calculate the effect of the collision with the boundary.

1. The collision point and the time of the collision are calculated by approximating the trajectory backwards as a straight line in the configuration space. The particle in question is then propagated backwards to the collision point, which corresponds to some time between the actual time-steps.

2. The velocity is changed according to the billiard reflection law in Eq. (2.79).

3. The particle is propagated with the new velocity linearly to the end of the time-step.

As we see from the description, we do not use the main integration scheme when handling the boundary collisions. This results in increase in energy in interacting many-particle systems. This is the most prominent approximation in the entire propagation scheme, and therefore the propagation algorithm, i.e., the velocity Verlet algorithm, is only of second order in our code. Nevertheless, we have found that the method is sufficiently accurate for the purpose of our calculations.

For future reference, we describe here a more accurate way to handle the boundary collisions. The time-step, during which the collision occurs, could be divided into smaller intervals to get closer to the boundary with the main integration scheme. The actual collision point could then be calculated *in parallel* using, e.g., the bisection method. This way, the linear approximation step could be either completely skipped or at least the corresponding system time would be significantly shorter. This would also enable the use of higher order integrators and a larger overall time-step.

After handling the boundary collisions of each particle, we check if the end criterion, e.g., the maximum simulation time, is fulfilled. If it is fulfilled, the simulation ends; otherwise we continue the propagation.
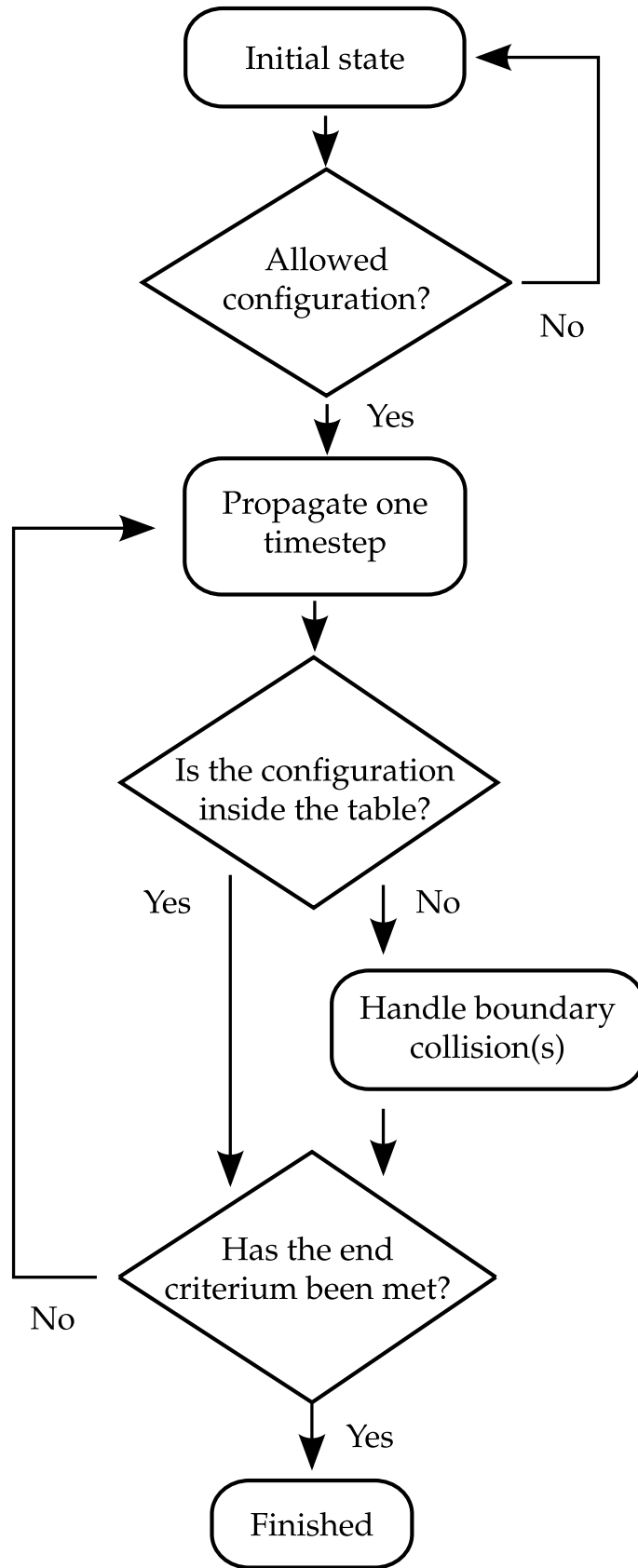
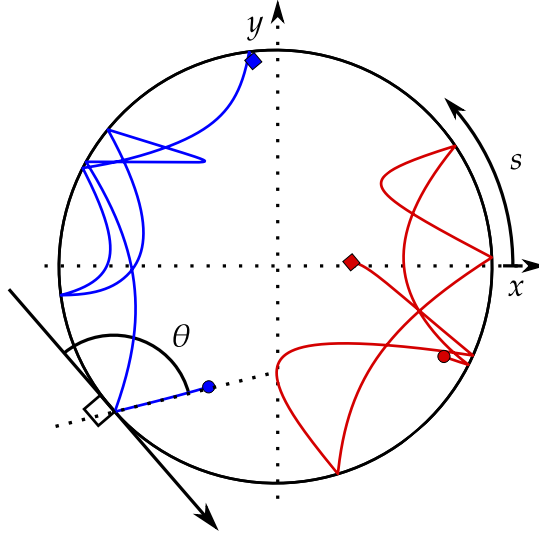Figure 17: Flowchart of the propagation scheme in the *Bill2d* code

Figure 18: Coordinate system of the circular billiards

5 Results

5.1 Coulomb-interacting billiards in circular cavities

5.1.1 System

We consider here two-dimensional circular billiards with two Coulomb-interacting particles (electrons) (Fig. 18). The results shown here have been published in our recent article [88]. As discussed above in Sec. 4.1, the system is described by the Hamiltonian (4.16) that for our two-particle system reads

$$H = \frac{1}{2}\left(v_1^2 + v_2^2\right) + \frac{\alpha}{\|r_1 - r_2\|},\tag{5.1}$$

where $r_i = (x_i, y_i)$ is the position and $v_i = (v_{i,x}, v_{i,y})$ the velocity of the ith particle. Total energy of the system is fixed to $E = 1$ and the radius of the circular table to $R = 1/2$. These conditions restrict the interaction strength to $0 \leq \alpha \leq 1$. $\alpha = 0$ is the noninteracting limit, where we have essentially two independent particles. $\alpha = 1$, on the other hand, is the strong-interaction limit, where the kinetic energy is zero and the particles are localized at the opposite sides of the circular table. We remind that just by varying α we can study all the length and energy scales of the two-particle circular billiards.

The collisions with the boundary are described by the oriented arc length $s \in \;]{-\pi/2}, \pi/2]$ from the chosen origin and the angle θ between the velocity of the incoming particle and tangent of the boundary as illustrated in Fig. 18. $\theta < \pi/2$ and $\theta > \pi/2$ correspond to counterclockwise and clockwise directions, respectively.

5.1.2 Bouncing maps

In Fig. 19 we show examples of trajectories and bouncing maps for billiards with different interaction strengths α. The bouncing maps show s and $\cos(\theta)$ for each collision of one of the particles. The bouncing maps are not Poincaré sections *per se*, but they can be thought as projections of the six-dimensional Poincaré sections (collision maps) to certain two-dimensional surfaces. Even if the bouncing maps do not show the entire structure of the phase space, they can be used to get qualitative information on the dynamics. The bouncing maps in Fig. 19 consist of 14 000 ($\alpha = 10^{-5}$) and 5 600 ($\alpha = 0.2$ and 0.7) collisions with the boundary for one of the particles in the system. In the figure, only a short time interval of the corresponding trajectory is shown.

The noninteracting system with $\alpha = 0$ is a classical example of regular billiards [42] where all the trajectories are marginally stable and form straight lines in the bouncing maps. In the configuration space the trajectories draw a pattern that fills only a portion of the table leaving a central circle of the table untraveled. The weak-interaction limit $\alpha = 10^{-5}$ (upper panel of Fig. 19) should be compared to the noninteracting case. The bouncing map shows deviations from the noninteracting case as seen by several different straight lines. Only when the particles pass very close to each other, the interaction is strong enough to affect the trajectories. Depending on how close the particles pass each other and at which angles, the effect ranges from small to drastic jumps from one quasi-regular trajectory to another. These jumps are are seen as parallel lines with irregular spacing in the bouncing map.

In the intermediate interaction range (middle panel of Fig. 19), the behavior of the trajectories seems chaotic, and the bouncing map gets filled. On the average, the particles hit the wall perpendicular to the boundary. As the interaction strength α is increased, the maximum of the probability distribution for θ splits into two for some trajectories as seen in the bottom panel in Fig. 19. The splitting corresponds to trajectories in which the particles are bouncing on the opposite sides of the circle while in a collective circulating motion so that the dominant collision angles slightly differ from $\theta = \pi/2$. This effect, however, is smoothed out when a large ensemble of trajectories is taken into account. When α is increased further, we find close to the strong-interaction limit $\alpha = 1$ that the system becomes (quasi)regular. The transition to (quasi)regularity is analyzed in the following section.
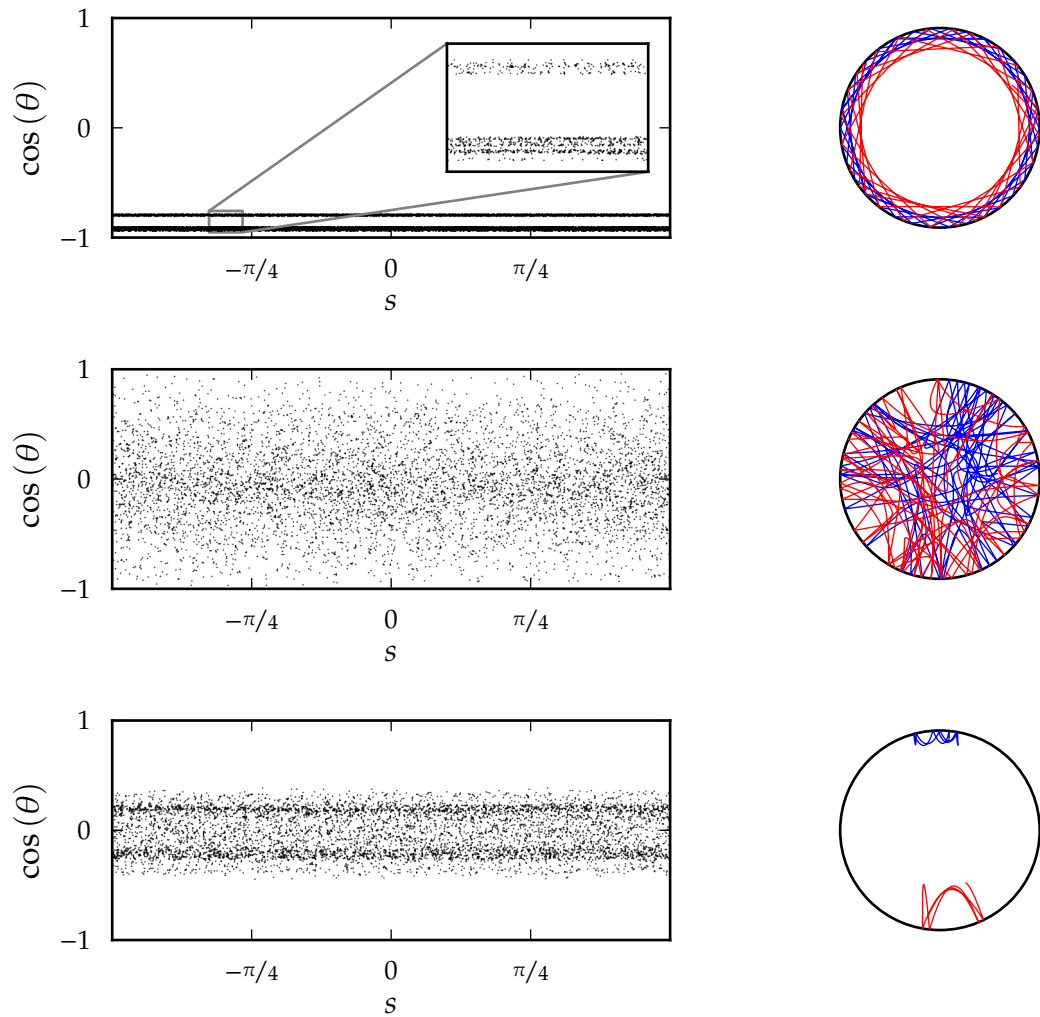
Figure 19: Bouncing maps and trajectories for two-particle circular billiards with interaction strengths $\alpha = 10^{-5}$ (top), $\alpha = 0.2$ (middle), and $\alpha = 0.7$ (bottom). Only a small section of the trajectories corresponding to the bouncing maps is shown.
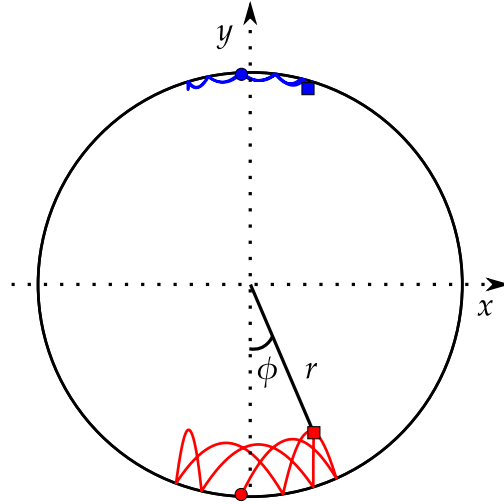
Figure 20: Polar coordinates used to describe the strong-interaction limit of the system.

5.1.3 Strong-interaction limit

At strong interactions, i.e., with $\alpha \lesssim 1$, the effect of the interaction between the particles varies only slightly in time since the particles are nearly localized at the opposite sides of the table. For simplicity, we consider only the case of zero angular momentum in the strong-interaction limit.

Due to zero angular momentum, the particles oscillate around an axis that goes through the center of the table. Also, due to full rotational symmetry, we can choose – without any loss of generality – this axis to be the y-axis. With this choice of coordinates we have one particle in the upper part of the table ($y > 0$) and one in the lower part ($y < 0$).

In the following we will make use of polar coordinates (r, ϕ) defined by

$$r = \sqrt{x^2 + y^2} \tag{5.2}$$

$$\phi = \arcsin\left(\frac{x}{\sqrt{x^2 + y^2}}\right) \tag{5.3}$$

as shown in Fig. 20. The unit vectors in the polar coordinates are

$$\hat{e}_r = \sin\phi\hat{x} - \cos\phi\hat{y} \tag{5.4}$$

$$\hat{e}_\phi = \cos\phi\hat{x} + \sin\phi\hat{y}, \tag{5.5}$$

where $\hat{x}$ and $\hat{y}$ are the unit vectors in cartesian coordinates. They can also be rewritten as

$$\hat{x} = \sin\phi\hat{e}_r + \cos\phi\hat{e}_\phi \tag{5.6}$$

$$\hat{y} = -\cos\phi\hat{e}_r + \sin\phi\hat{e}_\phi. \tag{5.7}$$

The total angular momentum can be written as

$$L = r_1(t)v_{\phi,1}(t) + r_2(t)v_{\phi,2}(t), \tag{5.8}$$

where $r_i(t)$ are the distances of the particles from the center of the table and $v_{\phi,i}(t)$ the tangential velocities. Since $r_1(t) \approx r_2(t)$, Eq. (5.8) – together with conservation of angular momentum – shows that the particles must have nearly equal tangential speeds at all times. In particular, the tangential velocities must have opposite signs at all times to ensure zero angular momentum. We can therefore conclude that $\phi_1(t) \approx \phi_2(t)$ leading to $x_1(t) \approx x_2(t)$ since $r_1(t) \approx r_2(t)$.

Since $x_1(t) \approx x_2(t)$, the force acting on the particle in the lower part of the table can be approximated by

$$F \approx -\frac{\alpha}{\|r_1(t) - r_2(t)\|^2}\hat{y}, \tag{5.9}$$

where $\hat{y}$ is the unit vector in the y-direction. As $\alpha \to 1$, also $\|r_1(t) - r_2(t)\| \to 1$, and thus, we can estimate

$$\frac{\alpha}{\|r_1(t) - r_2(t)\|^2} \approx 1$$

in the strong-interaction limit. This approximation becomes exact as $\alpha \to 1$. In total, the force can be written as

$$F \approx -\hat{y}. \tag{5.10}$$

Collisions with the boundary are easiest to take into account in polar coordinates where only the radial velocity is reversed in a collision. In the strong-interaction limit ϕ is small, and we can make a small-angle approximation to Eq. (5.7), i.e., $\cos\phi \approx 1 + O(\phi^2)$ and $\sin\phi \approx \phi + O(\phi^2)$. This gives the force acting on the lower particle in polar coordinates,

$$F \approx \hat{e}_r - \phi\hat{e}_\phi. \tag{5.11}$$

Next, we use Newtonian dynamics to calculate the equations of motion in polar coordinates. The position of the lower particle in polar coordinates is just

$$r = r\hat{e}_r. \tag{5.12}$$

The velocity can be directly calculated as

$$\dot{r} = \dot{r}\hat{e}_r + r\frac{d\hat{e}_r}{dt}, \tag{5.13}$$

where using Eqs. (5.2), (5.4), and (5.5) we get

$$\frac{d\hat{e}_r}{dt} = \dot{\phi}(t)\cos\phi\hat{x} + \dot{\phi}(t)\sin\phi\hat{y} = \dot{\phi}(t)\hat{e}_\phi, \tag{5.14}$$

i.e.,

$$\dot{r}(t) = \dot{r}(t)\hat{e}_r + r(t)\dot{\phi}(t)\hat{e}_\phi. \tag{5.15}$$

Continuing further, we get for the acceleration

$$\ddot{\boldsymbol{r}} = \ddot{r}\hat{\boldsymbol{e}}_r + \dot{r}\frac{d\hat{\boldsymbol{e}}_r}{dt} + \dot{r}\dot{\phi}\hat{\boldsymbol{e}}_\phi + r\ddot{\phi}\hat{\boldsymbol{e}}_\phi + r\dot{\phi}\frac{d\hat{\boldsymbol{e}}_\phi}{dt}$$
$$= (\ddot{r} - r\dot{\phi}^2)\hat{\boldsymbol{e}}_r + (r\ddot{\phi} + 2\dot{r}\dot{\phi})\hat{\boldsymbol{e}}_\phi, \tag{5.16}$$

where we have used

$$\frac{d\hat{\boldsymbol{e}}_\phi}{dt} = -\dot{\phi}\hat{\boldsymbol{e}}_r,$$

which was calculated from Eq. (5.5).

Equations (5.11) and (5.16) together give the equations of motion in polar coordinates,

$$\ddot{r} - r\dot{\phi}^2 = 1 \tag{5.17}$$
$$r\ddot{\phi} + 2\dot{r}\dot{\phi} = -\phi. \tag{5.18}$$

They can not be solved analytically, but since the kinetic energy of the particle will be small in the strong-interaction limit, we may expect centrifugal [second term in Eq. (5.17)] and coriolis [second term in Eq. (5.18)] terms[17] to be negligible, i.e., the equations of motion would be

$$\ddot{r} = 1 \tag{5.19}$$
$$r\ddot{\phi} = -\phi. \tag{5.20}$$

Finally, we decouple these differential equations by assuming that the small variation of r in Eq. (5.20) will not have a dramatic effect on the solution for $\phi(t)$. Thus, we replace r in the lower equation by its average r_{avg}, which can be calculated from the solution of $r(t)$ in Eq. (5.19). Later we will show that these assumptions are valid by numerically solving Eqs. (5.17) and (5.18) and comparing them to our simplified model.

Solution to Eq. (5.19) is

$$r(t) = r(0) + \dot{r}(0)t + \frac{1}{2}t^2, \tag{5.21}$$

where $r(0)$ and $\dot{r}(0)$ are the initial values for r and its time derivative. This solution is only valid up to the first collision. At each collision the sign of $\dot{r}$ is changed and thus $r(t)$ is actually a periodically repeating parabola. To express $r(t)$ for all times in a closed form, we first calculate the time t_s when the particle last collided (before $t = 0$) with the boundary in the time-reversed dynamics [where $r(t_s) = R$] yielding

$$t_s = -\dot{r}(0) - \sqrt{\dot{r}(0)^2 + 2[R - r(0)]}, \tag{5.22}$$

where $R = 1/2$ is the radius of the circle. On the other hand, the period T between collisions is

$$T = 2\sqrt{\dot{r}(0)^2 + 2[R - r(0)]}. \tag{5.23}$$

---

[17]Notice that despite their names, these terms are not due to a noninertial frame of reference but due to the polar basis in the inertial frame of reference.

Using t_s and T, we can construct a periodic sawtooth wave

$$\tau(t) = T\left[\frac{t - T - t_s}{T} - \left\lfloor\frac{t - T - t_s}{T}\right\rfloor\right]$$

(5.24)

that has a period T, minimum value 0, maximum value T, and a shift t_s in time so that $\tau(t_s) = 0$ and $\tau(0) = |t_s|$. Here $\lfloor\cdot\rfloor$ is the floor function. After each collision we have $\tau = 0$ and just before each collision $\tau = T$.

The radial velocity of the particle when colliding with the boundary is

$$\dot{r}(\tau = 0) \doteq \dot{r}(t_s) = \dot{r}(0) + t_s.$$

(5.25)

The equation (5.25) can be used to write the periodic solution for the radial distance r as

$$r(t) = R + \dot{r}(\tau = 0)\tau(t) + \frac{1}{2}\tau(t)^2.$$

(5.26)

For the angular equation we need the cycle average of the radius,

$$r_{\text{avg}} = \frac{1}{T}\int_0^T r(\tau)\,d\tau = R + \frac{1}{6}T[T + 3\dot{r}(\tau = 0)].$$

(5.27)

Let us now concentrate on the angular equation

$$r_{\text{avg}}\ddot{\phi} = -\phi.$$

(5.28)

It has the solution

$$\phi(t) = \phi(0)\cos\left(\frac{t}{\sqrt{r_{\text{avg}}}}\right) + \sqrt{r_{\text{avg}}}\dot{\phi}(0)\sin\left(\frac{t}{\sqrt{r_{\text{avg}}}}\right),$$

(5.29)

where $\phi(0)$ and $\dot{\phi}(0)$ are the initial values for the polar angle and its time derivative. To calculate the bouncing maps, we also need the tangential velocity

$$v_\phi = R\dot{\phi}(t) = -\frac{R}{\sqrt{r_{\text{avg}}}}\phi(0)\sin\left(\frac{t}{\sqrt{r_{\text{avg}}}}\right) + R\dot{\phi}(0)\cos\left(\frac{t}{\sqrt{r_{\text{avg}}}}\right).$$

(5.30)

Our model predicts the collisions with the boundary to take place at $t = nT + t_s$ where $n \in \mathbb{Z}$. We can thus write the cosine of the collision angle of the nth collision as

$$\cos[\theta(n)] = \frac{v_\phi(nT + t_s)}{\sqrt{v_r(nT + t_s)^2 + v_\phi(nT + t_s)^2}} = \frac{v_\phi(nT + t_s)}{\sqrt{\dot{r}(\tau = 0)^2 + v_\phi(nT + t_s)^2}},$$

(5.31)

where the cosine has been calculated by simple trigonometry of the collision.
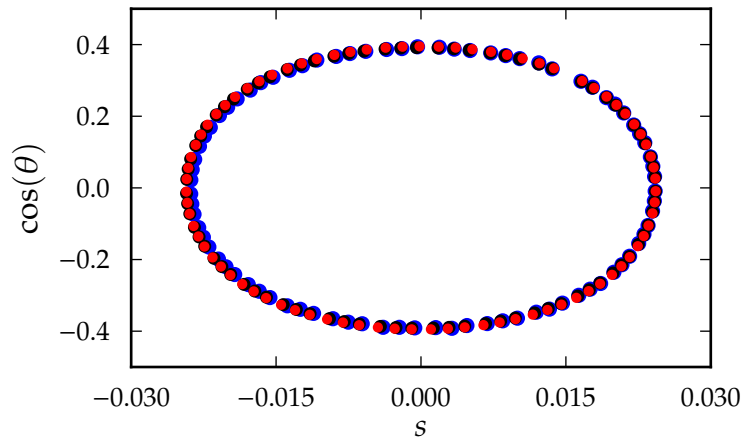
In Fig. 21 we compare our model calculated with Eqs. (5.26) and (5.29) (red curves and dots) with simulated, numerically exact data calculated with the time-step $\Delta t = 10^{-6}$ (blue curves and dots), and the full solution to Eqs. (5.17) and (5.18) (dashed black curves and dots). Figs. 21(a) and 21(b) show an example trajectory
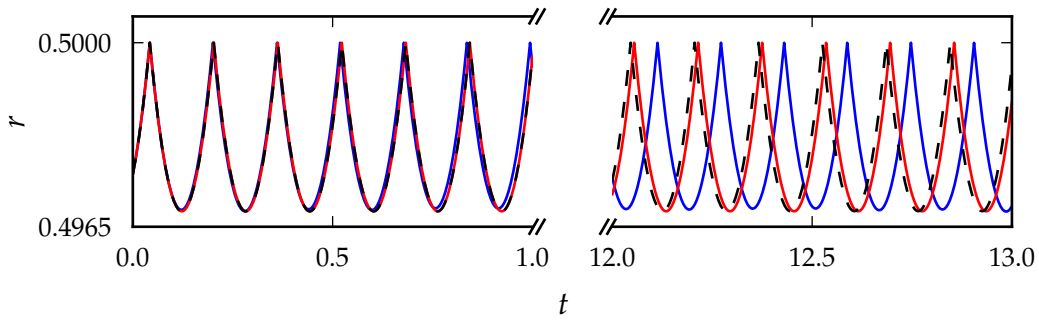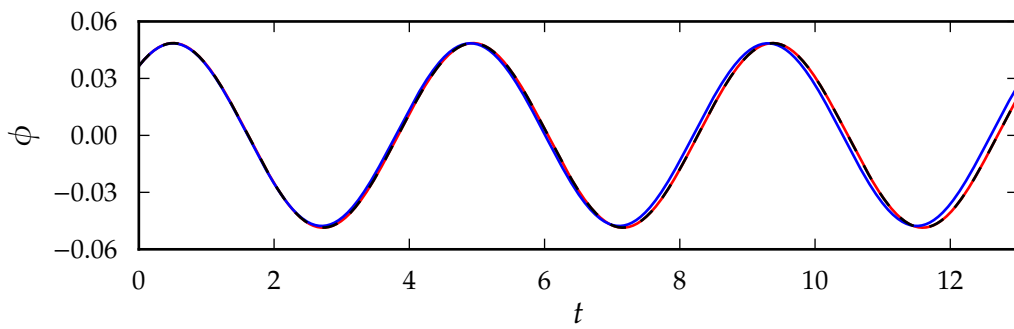
Figure 21: (a) Radial coordinate, (b) angular coordinate, and (c) bouncing map for zero angular momentum circular billiards with $\alpha = 0.98$. The analytical model is in red, the numerically solved model in black, and the simulated data in blue. At extremely strong interaction strengths the model produces well the temporal dynamics of the system.
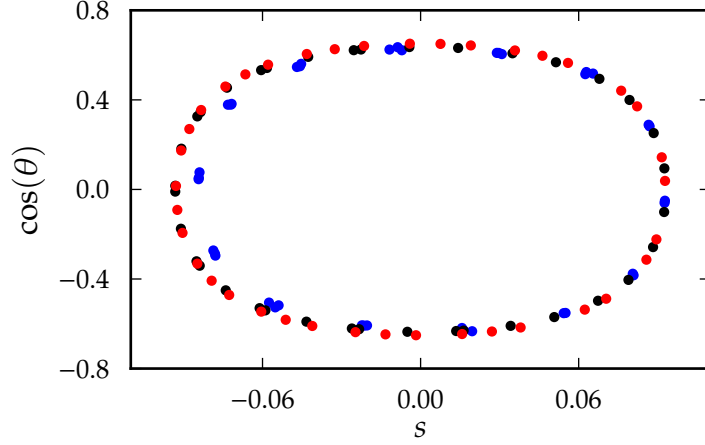
Figure 22: Bouncing map for $\alpha = 0.9$ with zero angular momentum. The analytical model is shown in red, the numerically solved model in black, and the simulated data in blue. The model produces the form of the bouncing map well down to $\alpha \gtrsim 0.9$.

with $\alpha = 0.98$. Our model agrees well with the simulated data, and the difference in longer times is mostly seen due to slight overestimation of the collision period in our model. The full solution of the Eqs. (5.17) and (5.18) (blue curve) does not yield better results than our model implying that the difference between the simulated data and our model is due to approximations of the force rather than due to neglecting the centrifugal and coriolis terms of the acceleration.

The full trajectory is reproduced well down to $\alpha \gtrsim 0.98$ for several bounces. The form of the bouncing map of our model agrees with the simulated data at $\alpha \gtrsim 0.9$ (Fig. 22) even if the temporal dynamics are reproduced only at larger values of α. In some specific cases, the model produces the form of the bouncing map with even lower values of α.

Our analytical model is a regular, non-hyperbolic system. Furthermore, as $\alpha \to 1$, our model becomes more and more accurate, and in the limit $\alpha \to 1$ all our approximations become exact. To emphasize, this means the since the true system reduces to our model as $\alpha \to 1$ and since our model is regular, also the true system with nonzero angular momentum becomes regular in the strong-interaction limit $\alpha \to 1$.

We note that it is also possible to deduce the form of the bouncing maps in the strong α limit by using conservation laws [88, 95]. The advantage of the approach we have used here is that (i) we can also model temporal dynamics and (ii) we can have a clear understanding of the approximations used. Both approaches have the same applicability range in α when reproducing the form of the bouncing map.

Here we have restricted the calculations to zero angular momentum. Due to complications caused by the collective rotation, the analytical model was not extended to nonzero angular momenta. However, we note that the bouncing maps show quasi-regular behavior also in the case of nonzero angular momentum in the strong-interaction limit.

5.1.4 Escape-time distributions

Next, we study the changes in the system dynamics as the interaction strength is varied from the noninteracting ($\alpha = 0$) to the intermediate-interaction regime ($\alpha \lesssim 0.5$). The structure of the phase space can not be studied directly since the calculation of six-dimensional Poincaré sections is not possible in practice. As an alternative method we open up the billiards and consider the escape-time distributions. As discussed in Sec. 3.6, power-law asymptotics of the distributions would indicate sticky or KAM regions in the phase space whereas exponential distributions would indicate nonsticky, i.e., fully hyperbolic behavior at the calculated time scales. However, since the escape-time distributions are statistical properties of the system and they reflect the amount of stickiness in the system rather than regular and chaotic components of the phase space, we can not draw any conclusions about the detailed structure of the phase space.

The circular table is opened by placing ten holes at even distances in the boundary covering total of 1/50 of the length of the boundary, the same amount as in Ref. [96]. The two-particle trajectories escape when either particle hits the hole. We choose to express the escape-time distributions P as a function of the total number of collisions n, i.e., the sum of collisions of both particles, rather than as a function of time due to different time scales of systems with different α. In principle, this might affect the form of P as explained in Sec. 3.6.2. However, we have numerically checked that the behavior of the escape-time distributions P is the same both as a function of n and as a function of time.

To calculate the escape-time distributions $P(n)$, we set up an ensemble of $N_0 = 2.5 \ldots 6 \times 10^5$ random initial points for each α. The trajectories in the ensemble are propagated in time and the escape-time distributions are calculated from

$$P(n) = \frac{\Delta N(n)}{N_0}, \tag{5.32}$$

where $\Delta N(n)$ is the number of escaping trajectories at nth total number of collisions. For each α the time step of the propagation is chosen in range $\Delta t = 10^{-8} \ldots 10^{-7}$ so that a sufficiently accurate simulation of the trajectories is guaranteed.

In Fig. 23(a) we show escape-time distributions of the noninteracting ($\alpha = 0$) and moderately interacting ($\alpha = 0.1, 0.3, 0.5$) systems. The noninteracting system has a power-law tail as expected due to the regularity of the system. A power-law fit $P \sim n^{-\gamma} + const$ to the tail of the distribution yields $\gamma = 3.46$.[18] The moderately interacting systems, on the other hand, exhibit purely exponential escape-time distributions at these time scales. The numerically obtained distributions are in perfect agreement with

$$P(n) = \frac{49^{n-1}}{50^n}, \tag{5.33}$$

which can be obtained by assuming that there is no correlation between two successive collisions and the probability to escape at each collision is the ratio of

---

[18]To ensure a good fit, all the fits have been calculated by minimizing the *relative* error between the fitted function and the data using the least squares minimization procedure.

holes on the boundary (1/50). In essence, this means that at these time scales the moderately interacting systems can be classified as chaotic.

The escape-time distribution of a weakly interacting system with $\alpha = 10^{-6}$ is compared with the noninteracting case in Fig. 23(b). The tail of the distribution of the weakly interacting system also follows a power law $P \sim n^{-\gamma} + const$ with $\gamma = 4.08$. The escape is slightly faster than in the noninteracting case, but still the system exhibits sticky behavior. This effect was already seen in the bouncing maps in Sec. 5.1.2. At small time scales the trajectories of the weakly interacting system follow (quasi-)regular trajectories similar to noninteracting trajectories, and therefore the distributions for both systems are similar at small time scales. The interaction, however, reduces the lengths of the quasi-regular parts of the trajectories, as already seen from the bouncing maps, and thus the survival probability (and escape-time distribution) is decreased at long time scales.

Finally, we make some assessments on the transition from regularity to chaoticity in the noninteracting limit at moderate interaction strengths. In Fig. 24 we show the escape-time distributions divided by the noninteracting distribution for different α. We see a clear transition to chaoticity represented by the exponential distribution of Eq. (5.33) as $\alpha \to 10^{-3}$. The transition occurs first at long numbers of collisions as seen in Figs. 23(b) and 24. This is due to the interaction affecting the long quasiregular trajectories more easily and thus reducing the stickiness in long times as already explained above.

As a final note, we point out that these numerical results do not exclude the possibility of small sticky regions that would not appear at time scales considered here. Furthermore, the regime $\alpha > 0.5$ is excluded from our studies since the measure of the energetically allowed region of the configuration space tends to zero as $\alpha \to 1$. A smaller region would require smaller holes in the boundary which in turn would require a smaller time-step and thus would increase the computational requirements of the simulations. Hence, we have focused here only on the range $0 \le \alpha \le 0.5$.

5.1.5   Summary

To summarize, we have studied Coulomb-interacting two-particle circular billiards with different interaction strengths. Projections of the Poincaré sections, i.e., the bouncing maps, show quasi-regular behavior both at weak ($\alpha \to 0$) and strong-interaction limits ($\alpha \to 1$), but otherwise the dynamics appear chaotic. Furthermore, we have derived an analytical model showing that in the strong-interaction limit the system becomes regular in the case of zero angular momentum.

To further analyze the dynamics, we have made use of escape-time distributions of the corresponding open system. The distributions are exponential for a wide range of interactions suggesting generally chaotic behavior at intermediate interaction ranges. Only the range $\alpha \le 10^{-3}$ appears to have sticky behavior at the time scales considered here.
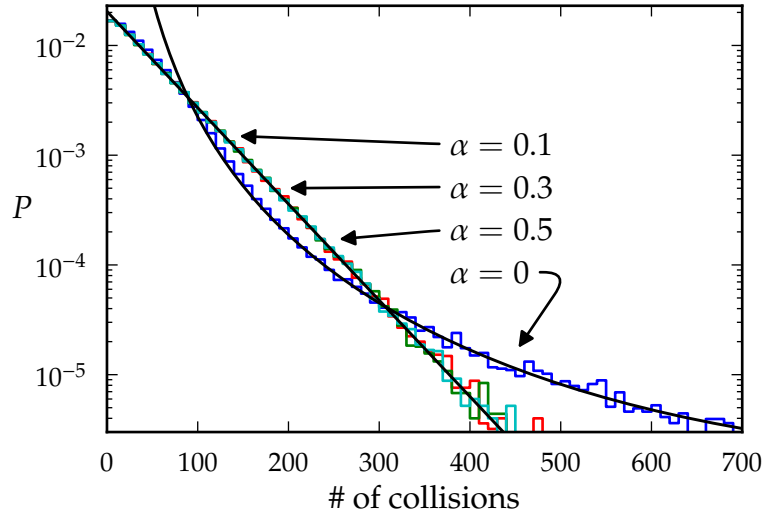
(a) Escape-time distributions in the noninteracting and intermediate-interaction regimes.
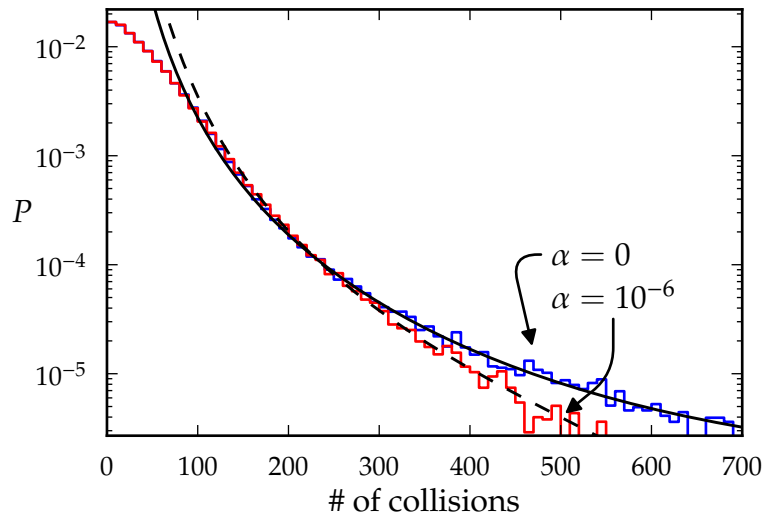
(b) Escape-time distributions in the noninteracting and weakly interacting regimes.

Figure 23: Escape-time distributions in the two-particle circular billiards. Both the noninteracting and weakly interacting cases show a power law tail whereas at $0.1 \leq \alpha \leq 0.5$ the distributions are exponential.
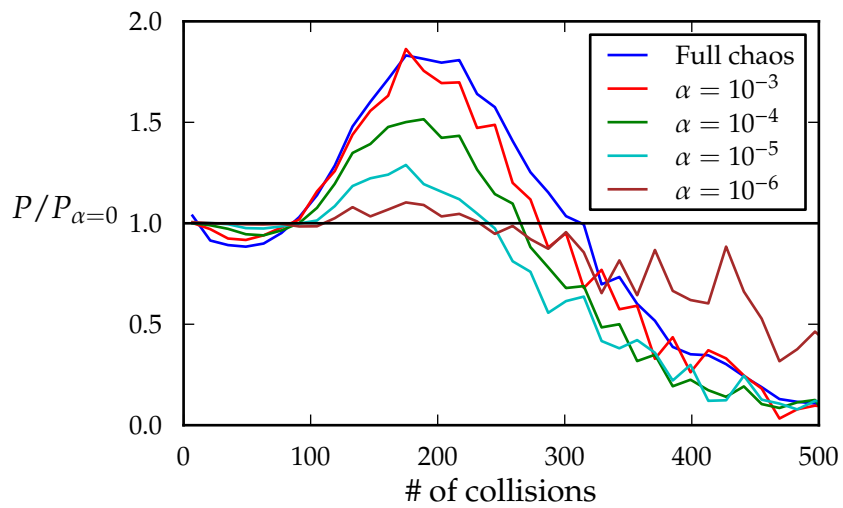
Figure 24: Escape-time distributions divided by the escape-time distribution of the noninteracting system. The transition to full chaos represented by Eq. (5.33) occurs as $\alpha \to 10^{-3}$.

Figure 25: Example trajectories of a diffusion process including nine Coulomb-interacting particles in a weak magnetic field. The circles and rectangles mark the initial and final positions of the particles, respectively.

5.2 Diffusion

5.2.1 System

We introduce a billiard table composed of two unit square containers connected by a channel of width Δ as demonstrated in Fig. 25. The geometry is motivated by similar experimentally realizable systems such as quantum point contacts and coupled quantum dots. The system consists of $N = 9$ Coulomb interacting charged particles (electrons) in a homogeneous magnetic field B perpendicular to the table. To justify the restriction to a specific particle number, we have checked that the results are qualitatively similar also for $N = 4, \ldots, 8$ particles in the intermediate-interaction regime. A posteriori we know that the results must be qualitatively similar also in the weak-interaction regime.

Our study focuses on a relaxation process where all the particles are initially in the left container (see Fig. 25, where the circles denote the initial positions). When over half, i.e., five, of the particles are in the right container, the system has reached an equilibrium with respect to the number of particles per container. We point out that the particles are also allowed to travel back from the right to the left container. The time it takes for the system to reach the equilibrium with respect to the number of particles per container for the first time is called the relaxation time t_{rel}. The behavior of the averages of the relaxation times as a function of the system parameters will be the focus of this study.

The total energy of the system is set to $E = 90$. The interaction strength α scales so that $\alpha = 0$ is the noninteracting limit and $\alpha \approx 1.5$ is close to the strong-interaction limit for the initial conditions. Since the particles are initially in the same container, which is less than half of the entire configuration space, initially strongly interacting systems with $\alpha \approx 1.5$ quickly become moderately interacting as the system begins to relax. To propagate the particles, we use the modified velocity Verlet algorithm for arbitrary magnetic fields (see Sec. 4.2), i.e., we propagate the Newtonian equations of motion. The time step used is $\Delta t = 10^{-5}$, although some results have

also been calculated with $\Delta t = 5 \cdot 10^{-6}$ to check the convergence of the results with respect to the time step.

5.2.2 Relaxation process

Since the 35-dimensional phase space is vast, we are interested only in ensemble averages. We set up a large ensemble of random initial configurations for each value of the parameter set (Δ, α, B).[19] Each configuration of the ensemble is propagated until it reaches the equilibrium. Finally, the ensemble average of the relaxation times $\langle t_{\text{rel}} \rangle$ is calculated. The size of the ensemble is increased until sufficient convergence of the average is achieved.

We are interested in the behavior of the average relaxation times as a function of the magnetic field B. However, since the effect of the magnetic field depends heavily on α, we need to replace B with a variable that describes the *effect* of the magnetic field on the trajectories. This in mind we define *the effective Larmor radius*

$$r_{\text{ELR}} = \left\langle \frac{1}{N} \sum_{i=1}^{N} \int_{0}^{t_{\text{rel}}} \frac{\|v_i(t)\|}{B} \theta(1 - x_i(t)) \, dt \right\rangle, \tag{5.34}$$

where $\theta(x)$ is the heaviside step function, v_i the velocity of the ith particle, and $\langle \cdot \rangle$ denotes the average over the ensemble. In essence, r_{ELR} describes the average effect of the magnetic field on the particles that are in the left container, i.e., still in the progress of traveling to the right container. In the limit $\alpha \to 0$ the effective Larmor radius r_{ELR} reduces to the conventional Larmor radius r_{LR} of the particles since the initial speeds are distributed evenly. Therefore, we can try to understand the results at weak interactions in terms of single-particle properties of open magnetic square billiards.

In essence, $r_{\text{ELR}} = const/B$, where *const* depends on the system parameters. However, we find that *const* is independent of the magnetic field B (see Fig. 26) and the channel width Δ. To emphasize, we have a bijective map between r_{ELR} and B, and the map depends on only one parameter, the interaction strength α.

To demonstrate the effects of the interaction, we show (i) the total kinetic energy as a function of time in Fig. 27 and (ii) speeds as a function of time and speed histograms of two different particles (red and blue) in Fig. 28. The calculated systems have the channel width $\Delta = 0.3$ and $B = 9$ corresponding to $r_{\text{ELR}} \approx 0.23$ at $\alpha = 1$ and $r_{\text{ELR}} \approx 0.49$ at $\alpha = 0.0001$.

At $\alpha = 0.0001$ the kinetic energy [Fig. 27(a)] is nearly a constant. The sharp drops are caused by the particles passing close to each other thus interacting more prominently. When the particles are away from each other, their speeds are almost constant [left panel of Fig. 28(a)]. However, when the particles come close to each other, their speeds change rapidly to new values, which is also seen as only a few almost discrete values for the speeds in the speed histograms [right panel of Fig. 28(a)]. The same behavior was seen in the bouncing maps of the two-particle

---

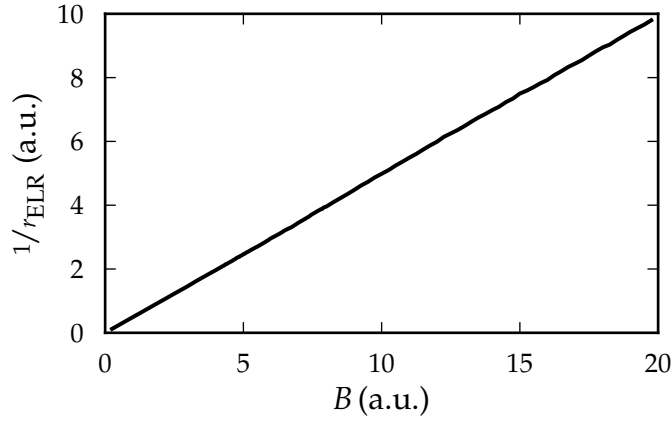[19]See Sec. 4.3 for further details on the randomization procedure.

Figure 26: The graph shows numerically calculated dependence between the inverse of the effective Larmor radius, $1/r_{\mathrm{ELR}}$, and the magnetic field B in the system with the channel width $\Delta = 0.3$ and the interaction strength $\alpha = 1$. Since the relation between $1/r_{\mathrm{ELR}}$ and B is bijective, also the relation between r_{ELR} and B is bijective.

circular billiards in Sec. 5.1.2.

In the intermediate-interaction regime with $\alpha = 1$ the total kinetic energy [see Fig. 27(b)] fluctuates due to complex dynamics. The initial increase in the total kinetic energy is due to the particles being close to each other in the initial state but as some of the particles travel to the right container, the potential energy of the system decreases thus increasing the overall kinetic energy. The speed-time graphs and the speed histograms in Fig. 28(b) show that the interaction is important also when the particles are far away from each other so that the particle speeds change constantly in contrast to the weak-interaction regime.
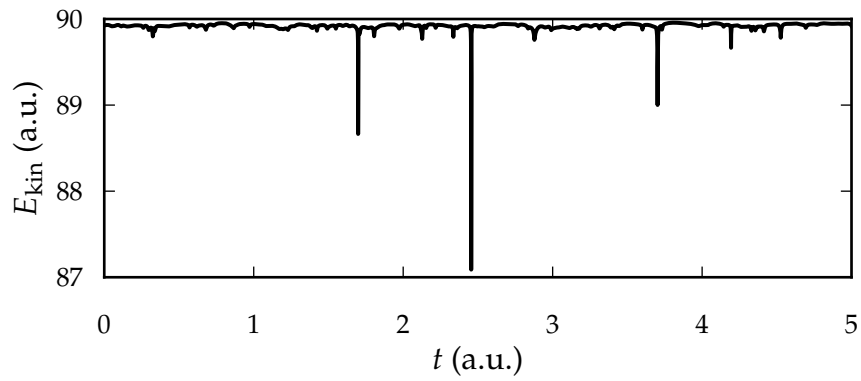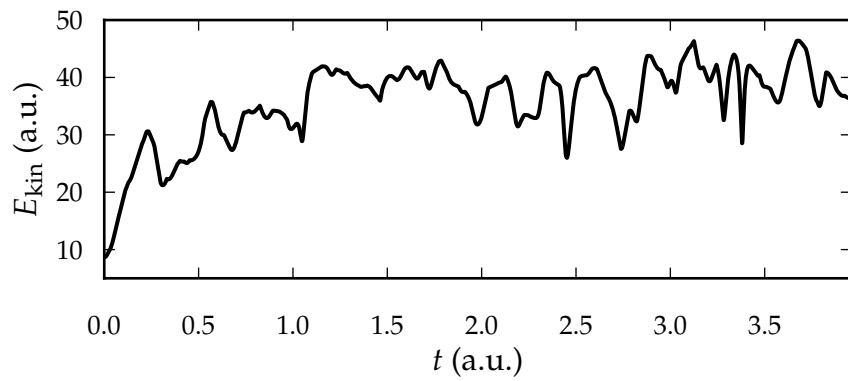
Figure 27: Total kinetic energy during one diffusion process for interaction strengths (a) $\alpha = 0.001$ and (b) $\alpha = 1$ in a system with the magnetic field $B = 9$ and the channel width $\Delta = 0.3$.
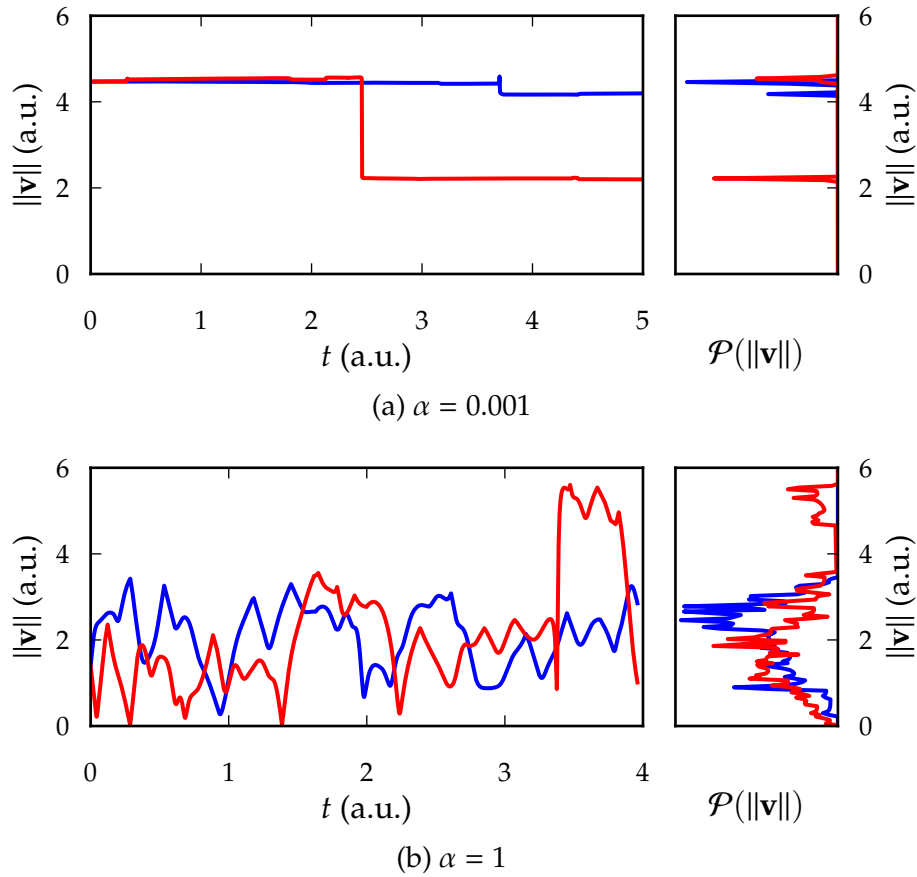
Figure 28: Speeds as a function of time (left panel) and speed histograms (right panel) for two different particles (blue and red) for interaction strengths (a) $\alpha = 0.001$ and (b) $\alpha = 1$ in a system with the magnetic field $B = 9$ and the channel width $\Delta = 0.3$.

5.2.3 Relaxation times

In Fig. 29 we show the average relaxation times $\langle t_{rel} \rangle$ as a function of r_{ELR} for interaction strengths $\alpha = 10^{-4}, \ldots, 1.5$ and the channel width $\Delta = 0.3$. The r_{ELR}-$\langle t_{rel} \rangle$ graphs have general features across all interaction strengths.

The rapid decrease of the relaxation time at $r_{ELR} \lesssim 0.3$, i.e., before the first minimum, is due to the magnetic field dominating over the Coulomb interaction in this regime: at small r_{ELR} the magnetic field strongly bends the particle trajectories (see Fig. 30) thus increasing the average relaxation time $\langle t_{rel} \rangle$.

The minimum at $r_{ELR} \approx 0.3$ exists for all interaction strengths α and channel widths Δ. This universal minimum is the optimal balance between the Coulomb interaction and the magnetic field allowing fast relaxation.

As r_{ELR} is increased to $r_{ELR} \gtrsim 4$, $\langle t_{rel} \rangle$ quickly tends to a constant. This is easy to understand since at large r_{ELR} the dynamics are alike due to dominating role of the Coulomb interaction over the magnetic field.

From Figs. 29(b) and 29(c) we see that as the interaction strength α is decreased to less than $\alpha \approx 0.3$, several new extrema appear in the r_{ELR}-$\langle t_{rel} \rangle$ graphs. In the range $\alpha \lesssim 0.3$ the system is weakly interacting, and the new extrema can be attributed to properties of the corresponding single-particle systems, i.e., open magnetic square billiards. This is studied further in Sec. 5.2.4.

The effective Larmor radii corresponding to the minima (blue) and maxima (red) do not depend heavily on the interaction strength as seen in Fig. 31. The positions of the extrema have been calculated from a fitted second or third order polynomial, or a low-order Laurent polynomial of only negative powers around the minimum. The error bars show visually estimated error limits for the calculated positions of the extrema. The extrema due to single-particle properties seen at $\alpha \lesssim 0.3$ naturally change only little with α since the effect of the Coulomb interaction is alike throughout the weak-interaction regime. Also, the position of the universal minimum changes only slightly from $r_{ELR} \approx 0.35$ to $r_{ELR} \approx 0.22$ as the interaction strength is increased from $\alpha = 10^{-4}$ to $\alpha = 1.5$. We note that the overall increase in the average relaxation time with increasing interaction strength α is expected due to smaller kinetic energies at higher interaction strengths.

The general shape of the r_{ELR}-$\langle t_{rel} \rangle$ graphs does not depend on the channel width Δ. However, the dependence of the exact value of $\langle t_{rel} \rangle$ on the channel width for a fixed r_{ELR} is more complicated, and it is different for weak and strong interactions. Also, r_{ELR} of the extrema increase only slightly with increasing channel width. At $\alpha = 1$ the effective Larmor radius r_{ELR} corresponding to the universal minimum increases from 0.28 ± 0.05 to 0.5 ± 0.1 when Δ varies from 0.1 to 1 as seen in Fig. 32. Similarly for weak interactions, in Fig. 33 we see that the positions the extrema are shifted to slightly larger r_{ELR} as Δ is increased.
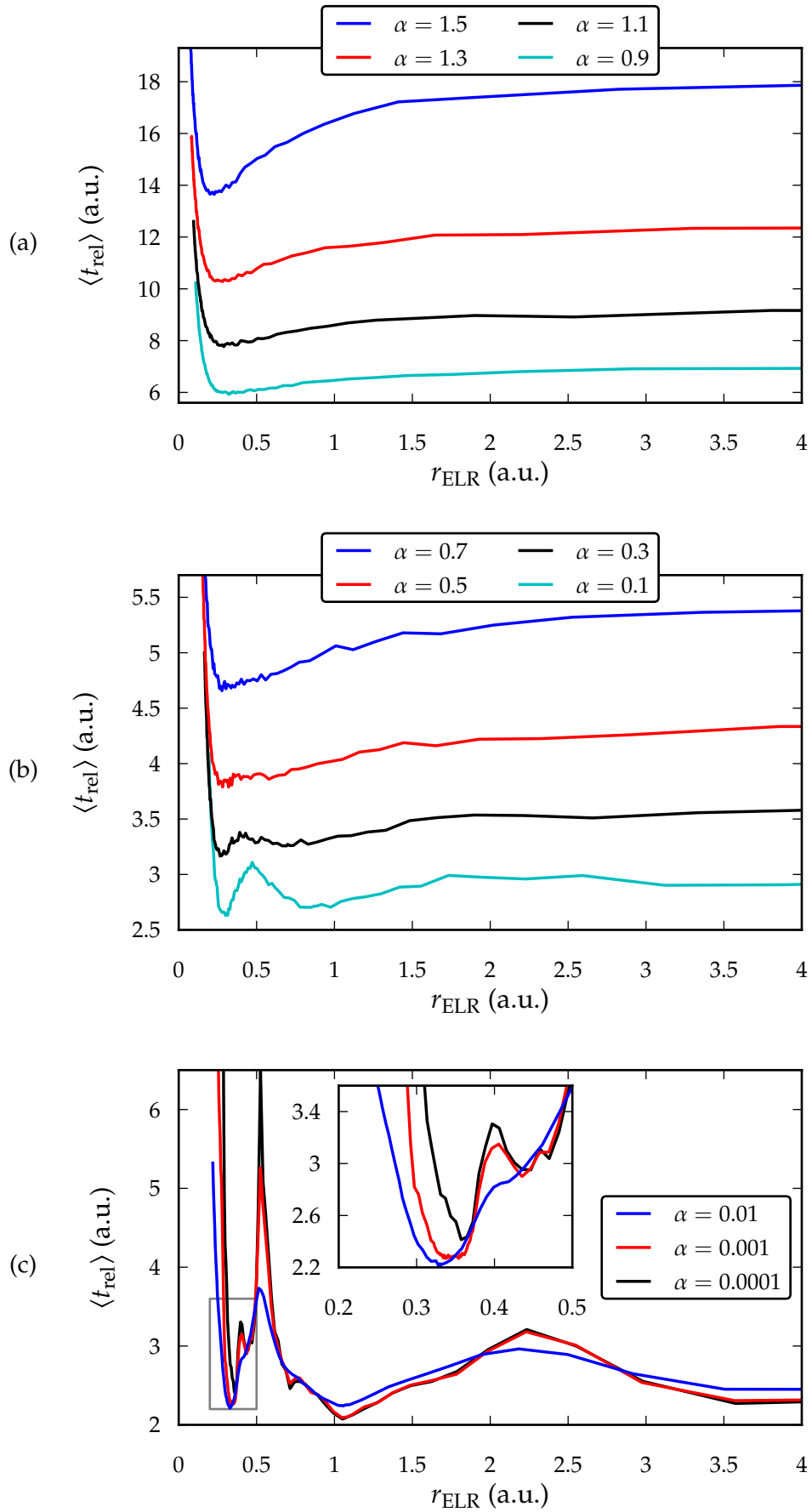
Figure 29: Dependence of the average relaxation time $\langle t_{\text{rel}} \rangle$ on the effective Larmor radius r_{ELR} for different interaction strengths α with the channel width $\Delta = 0.3$.

Figure 30: With effective Larmor radius $r_{ELR} = 0.103$ the magnetic field strongly bends the particle trajectories and therefore increases the average relaxation time compared to larger r_{ELR}.
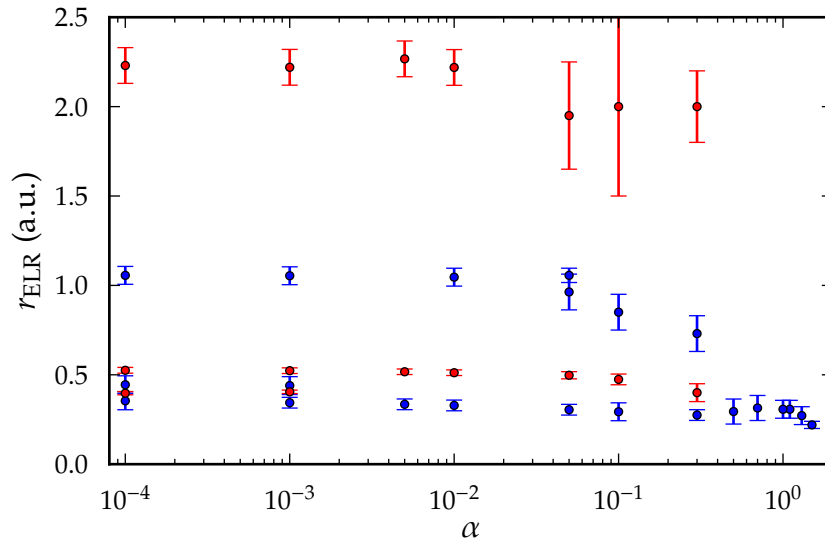

Figure 31: The effective Larmor radii r_{ELR} for which the average relaxation time $\langle t_{rel} \rangle$ finds its minima (blue) and maxima (red) with different interaction strengths α for the gate width $\Delta = 0.3$.
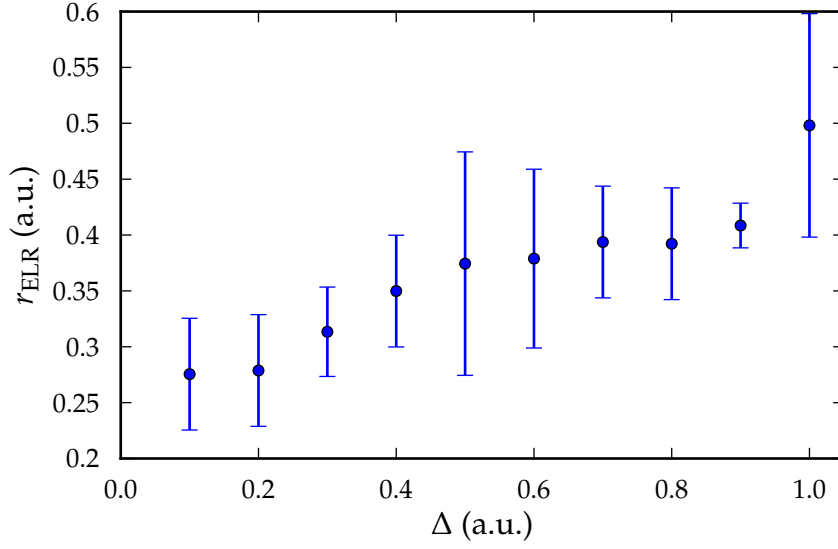
Figure 32: The effective Larmor radii r_{ELR} for which the average relaxation time $\langle t_{\mathrm{rel}} \rangle$ finds its minima with different gate widths Δ in the intermediate-interaction regime with the interaction strength $\alpha = 1$.

Figure 33: Dependence of the average relaxation time $\langle t_{\mathrm{rel}} \rangle$ on the effective Larmor radius r_{ELR} for different gate widths Δ in the weak-interaction regime with the interaction strength $\alpha = 0.01$.

5.2.4 Extreme weak-interaction limit

As already seen in Fig. 29(c), the more we decrease the interaction strength the more prominent the single-particle features, i.e., the additional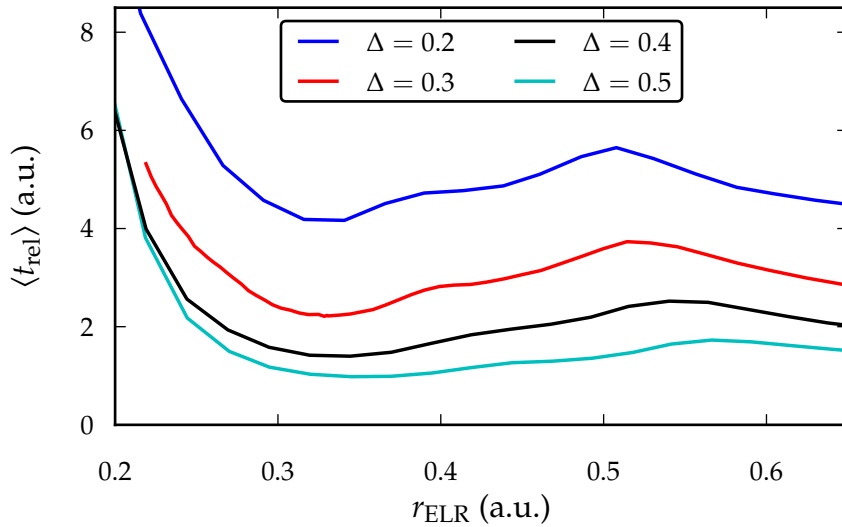 extrema at $\alpha \lesssim 0.3$, become. For example, the height of the peak at $r_{\mathrm{ELR}} \approx 0.5$ increases rapidly as $\alpha \to 0$. This is due to the perturbative nature of the Coulomb interaction in the weak-interaction limit.

To explain the extrema that appear only at weak interactions, we study open single-particle magnetic square billiards, which is the corresponding single-particle system since the effective Larmor radius r_{ELR} defined in Eq. (5.34) tends to the conventional Larmor radius of the particles r_{LR} in the limit $\alpha \to 0$. The magnetic square billiards, the sides of which are of unit length, is opened by placing a hole of width Δ in the center of one side of the billiard table. Here we focus on the case $\Delta = 0.3$.

In the single-particle case the average relaxation time $\langle t_{\mathrm{rel}} \rangle$ is the average escape time, which can be calculated from

$$\langle t_{\mathrm{rel}} \rangle = \int_0^\infty t \rho(t, r_{\mathrm{LR}}) \, dt, \tag{5.35}$$

where $\rho(t, r_{\mathrm{LR}})$ is the escape-time distribution of the system.

For each r_{LR} we set up a large ensemble[20] of initial points distributed uniformly in the phase space. The trajectories of the ensemble are propagated in time, and the escape-time distribution is calculated from

$$P(t) = \frac{\Delta N(t)}{N_0}, \tag{5.36}$$

where N_0 is the size of the ensemble and $\Delta N(t)$ is the number of escaping trajectories in a small time interval $[t - \delta t/2, t + \delta t/2[$, where δt is the size of the histogram bin. Only the trajectories that escape the system are taken into account.

To explain the peak of $\langle t_{\mathrm{rel}} \rangle$ at $r_{\mathrm{ELR}} \approx 0.5$ at weak interactions in Fig. 29(c), we show escape-time distributions at $r_{\mathrm{LR}} = 0.49, \ldots, 0.53$ in Fig. 34. Perfect fits to the escape-time distributions can be found with a combination of exponential and algebraic functions as in Ref. [97],

$$P(t) = A\lambda \exp(-\lambda t) + E\alpha(\beta - 1)(1 + \alpha t)^{-\beta}, \tag{5.37}$$

where $A + E = 1$ due to normalization and A, α, β, and λ are the fitting parameters. In the fits we neglect the initial, system dependent period. Furthermore, all the fits have been calculated by minimizing the *relative* error between the fitted function and the numerically calculated distribution with the least squares minimization procedure. As an example, we show a numerically calculated escape-time distribution (red) and the fitted function (blue) for $r_{\mathrm{LR}} = 0.5075$ in Fig. 35.

---

[20]The sizes of the ensembles are chosen such that the convergence of the escape-time distributions is guaranteed in the chosen time interval.
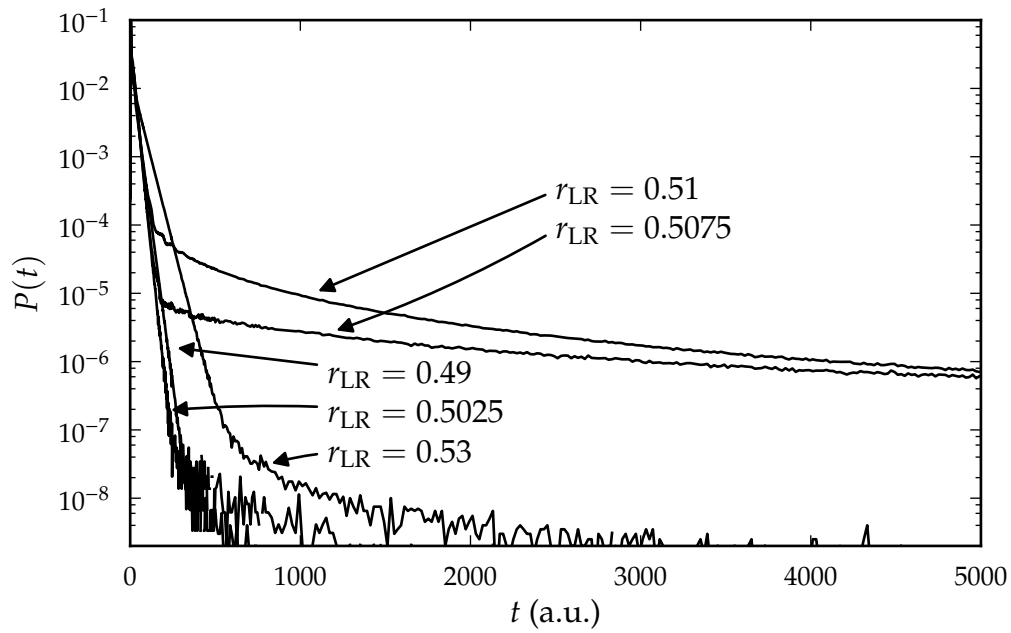
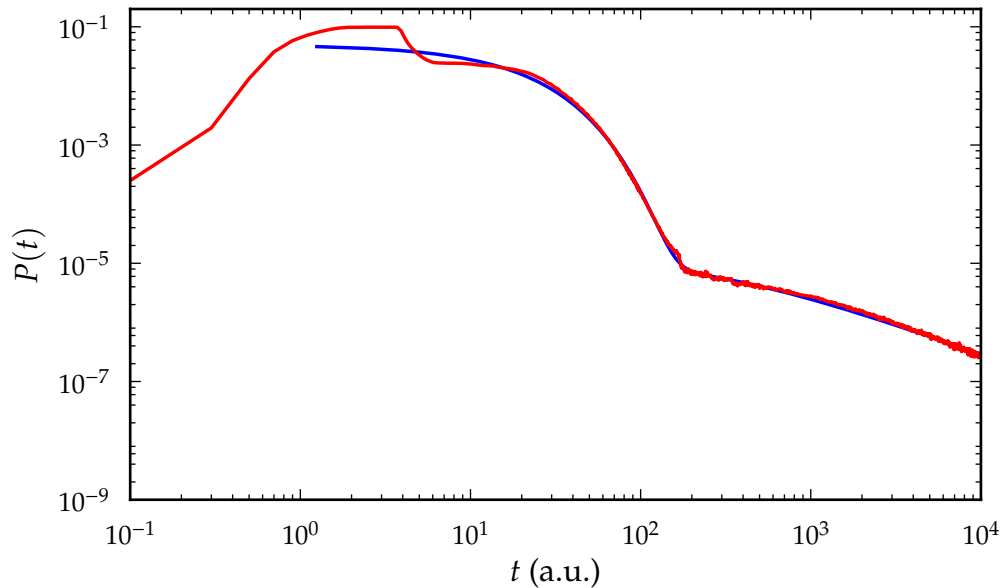Figure 34: Escape-time distributions for open magnetic square billiards with Larmor radii $r_{LR} = 0.49, \ldots, 0.53$.

Figure 35: Numerically calculated escape-time distribution for open magnetic square billiards with the Larmor radius $r_{LR} = 0.5075$ (red) and a fit to a combination of exponential and algebraic functions in Eq. (5.37) (blue).

At $r_{LR} = 0.49$ the escape-time distribution decays fast. However, as r_{LR} is increased, we find that the power-law tail becomes more prominent. At $r_{LR} = 0.5075$ the power-law tail has the exponent $\beta = 1.02$, i.e., the average escape-time integral in Eq. (5.35) diverges. The most divergent behavior is found at $r_{LR} \approx 0.5075$. As the effective Larmor radius is increased to $r_{LR} = 0.53$, the escape-time distribution returns to similar faster decaying shape (in the calculated time scales) seen at $r_{LR} = 0.49$. We interpret the rapid changes in the escape-time distributions around $r_{LR} = 0.5075$ as the cause of the peak in $\langle t_{rel} \rangle$ at $r_{ELR} \approx 0.5$ [Fig. 29(c)].

Next we attribute the changes in the escape-time distributions to changes in the phase space of the billiards. To identify the structures causing the extreme power-law tail, we calculate collision maps of the closed billiards and sections of the phase space that have not escaped before time $t = t^*$ in the open billiards. Trajectories that do not collide with the boundary are ignored since we concentrate on $r_{LR} \gtrsim 0.5$, where such trajectories do not exist.

To calculate the collision maps, we propagate a few hand-picked particle trajectories and calculate all their collisions with one side of the billiard table. The collisions are labeled by $s \in [0, 1]$, the length along the selected side of the table, and $\cos(\theta)$, cosine of the angle between the tangent of the boundary and the outgoing trajectory at the collision point. The range $s \in [0.35, 0.65]$ in the collision maps corresponds to the hole in the open system.

To calculate the remaining phase space of the open billiards at $t = t^*$, we set up a uniformly distributed ensemble of initial points in the phase space. The trajectories are propagated up to $t = t^*$, and the end points of the remaining trajectories, i.e., trajectories that have not escaped, are shown with black dots. The end points are labeled by the length along the boundary $s \in [0, 4]$ with $s \in [0.35, 0.65]$ corresponding to the hole and $\cos(\theta)$, cosine of the angle between the tangent of the boundary and the outgoing trajectory at the collision point.[21] Notice that due to the hole, the remaining phase space does not have a four-fold rotational symmetry, and therefore we can not reduce the consideration only to $s \in [0, 1]$ as we do with the collision maps of the closed system. The scheme is the Sprinkler scheme explained in Sec. 3.6.2, but here we also consider the KAM islands.

In Fig. 37 the leftmost column shows the collision maps for $r_{LR} = 0.49, \ldots, 0.53$ and the middle and right columns show the remaining phase space at times $t^* = 30$ and $t^* = 300$, respectively. At $r_{LR} = 0.49$ the large KAM island shown in Fig. 37(a) is connected to the hole and escapes the system before $t = 30$, which is seen as four large escaped areas (in white) in Fig. 37(b). The small sections of the phase space that do not escape, i.e., those that are still visible at $t = 300$ in Fig. 37(c), are due to the self-similarity of KAM-islands: there are several small islands located near the boundary of the large KAM island that are not connected to the opening in the boundary.

As the Larmor radius is increased to $r_{LR} = 0.5075$, the large KAM island breaks down to several disjoint islands as seen in Fig. 37(d). Some sections of these disjoint islands are not connected to the hole as seen from the remaining phase space at $t^* = 300$ concentrated at certain sections of the KAM islands [Fig. 37(f)].

---

[21]The end point is the last collision point with the boundary before $t = t^*$.

(a)   (b)
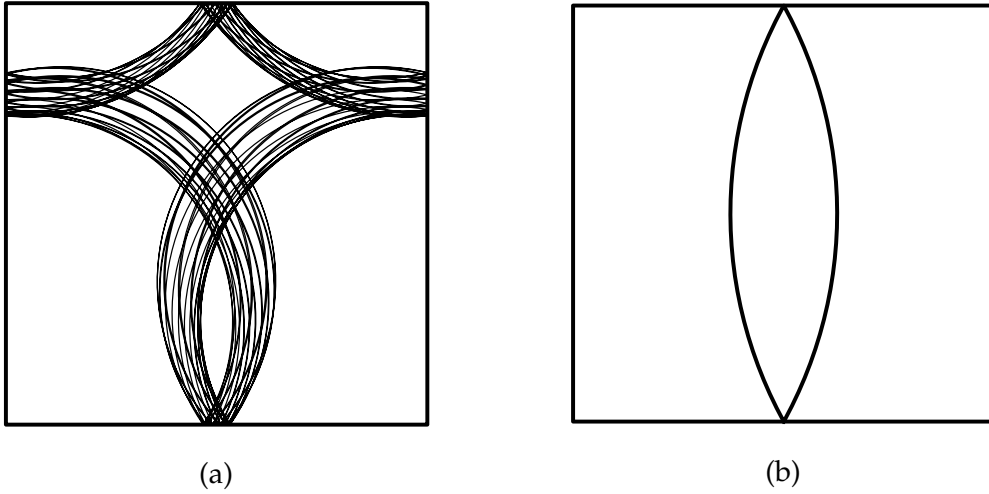
Figure 36: Examples of the families of trajectories responsible for the power-law behavior at Larmor radii (a) $r_{LR} = 0.5075$ and (b) $r_{LR} = 1.05$. In (a) we have a quasiperiodic KAM-orbit and in (b) a two-cycle MUPO.

Four of the sets of the remaining phase space seen in Fig. 37(f) correspond to a family of trajectories demonstrated in Fig. 36(a), and the other four to a family of trajectories that are mirror images of the trajectories of the first family. In Fig. 37(g) we see that as $r_{LR} \to 0.53$ the disjoint islands disappear and the remaining center island is connected to the hole [Fig. 37(i)].

We remind that the escape-time distributions do not include trajectories that do not escape the system, e.g., the remaining sections of the KAM islands at $t \to \infty$ for $r_{ELR} = 0.5075$. We interpret that the emergence of the non-escaping sets in the disjoint KAM islands is still the cause of the extremely slow power-law escape at $r_{LR} \approx 0.5075$. More specifically, it is the trajectories near the non-escaping sets that cause the change in the escape-time distributions. We conclude that the slow single-particle escape and also the appearance of the non-escaping sets at $r_{LR} \approx 0.5075$ are seen as the high peak in the average relaxation time $\langle t_{rel} \rangle$ at $r_{ELR} \approx 0.5$ at weak interactions in Fig. 29(c).
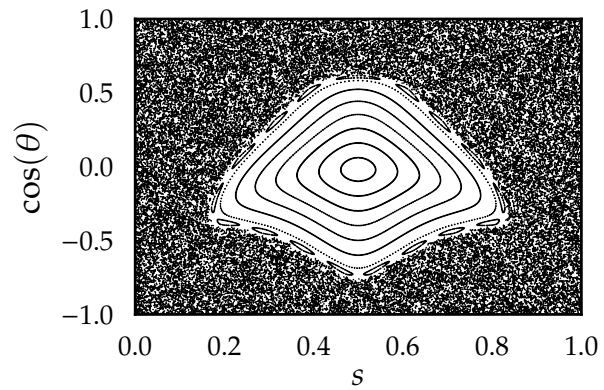
(a) $r_{LR} = 0.49$
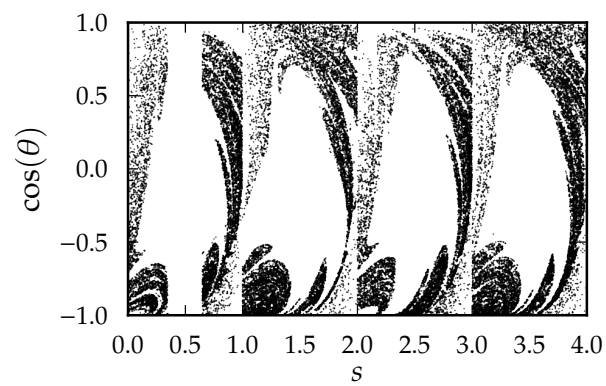
(b) $r_{LR} = 0.49$, $t^* = 30$
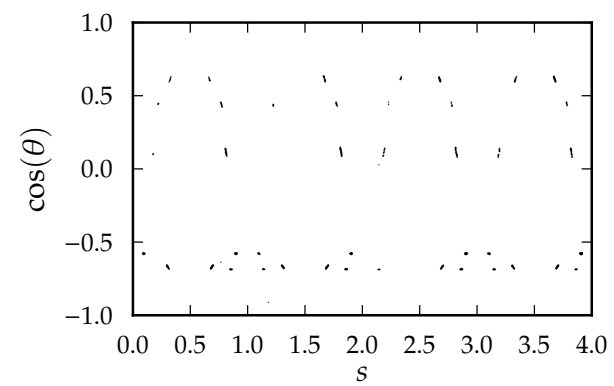
(c) $r_{LR} = 0.49$, $t^* = 300$
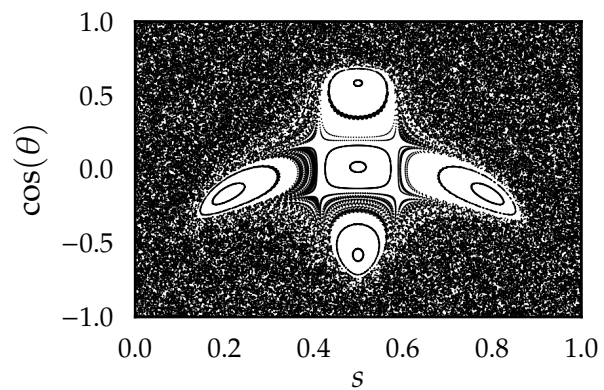
(d) $r_{LR} = 0.5075$
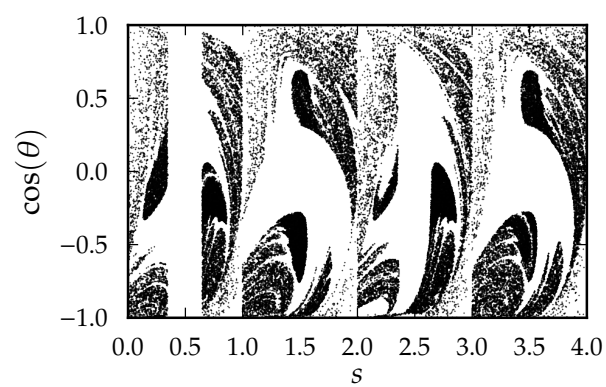
(e) $r_{LR} = 0.5075$, $t^* = 30$
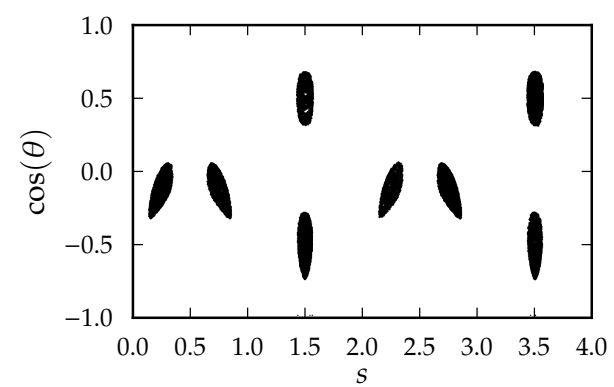
(f) $r_{LR} = 0.5075$, $t^* = 300$

Figure 37: Continues on the next page.
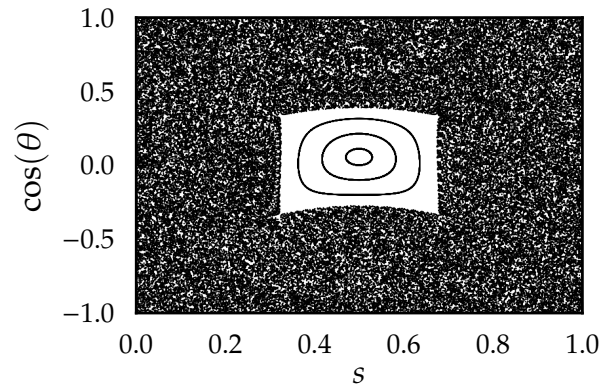
(g) $r_{LR} = 0.53$
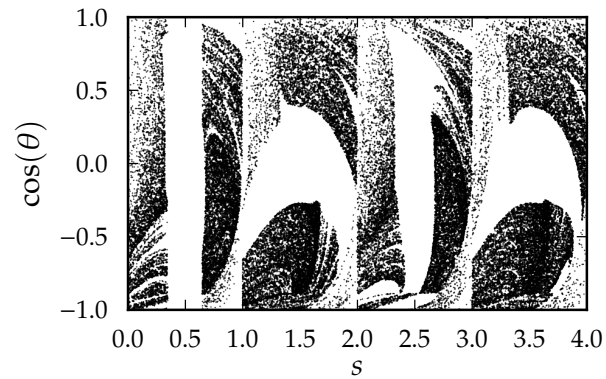
(h) $r_{LR} = 0.53$, $t^* = 30$
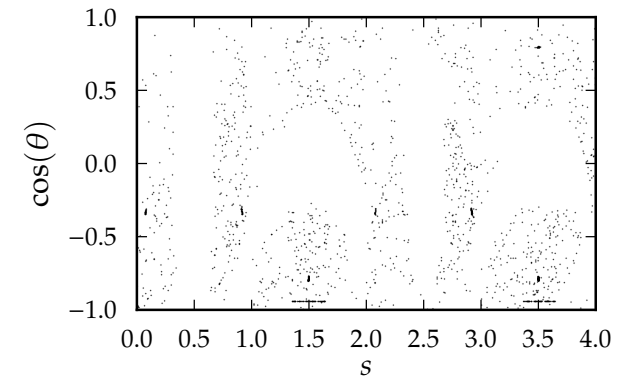
(i) $r_{LR} = 0.53$, $t^* = 300$

Figure 37: Poincaré sections in (a),(d), and (g) show that as the Larmor radius r_{LR} increases from 0.49 to 0.53, the large KAM island first splits into five separate parts at $r_{LR} \approx 0.5$. The outermost isolated islands are destroyed as $r_{LR} \rightarrow 0.53$. (b),(c),(e),(f),(h), and (i) show the remaining phase space for the open billiards at different times t^*.
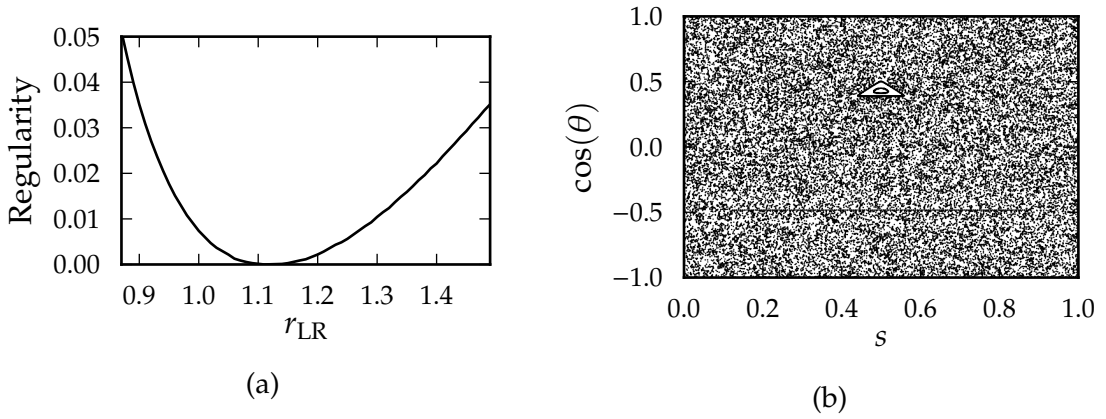
Figure 38: Around the Larmor radius $r_{LR} = \sqrt{5}/2 \approx 1.118$ the magnetic square billiards goes through a squeeze bifurcation where the KAM island in (b) – plotted here for $r_{LR} = 1.05$ – disappears and reappears [52]. This causes the numerically calculated area of the regular component of the Poincaré section in (a) to go to zero at $r_{LR} = \sqrt{5}/2$.

Let us next consider the minimum of the average relaxation time at $r_{ELR} \approx 1.05$ [Fig. 29(c)]. The phase space of the magnetic square billiards undergoes a squeeze bifurcation at $r_{LR} = \sqrt{5}/2 \approx 1.118$, i.e., the measure of the regular component of the phase space goes to zero as shown in Fig. 38(a) [52].[22] Due to the measure of the regular component going to zero, we may assume that around $r_{LR} = \sqrt{5}/2$ all the regular components of the phase space are located near the KAM island shown in Fig. 38(b). All the trajectories of the KAM island are connected to the hole at $0.93 \lesssim r_{LR} \lesssim 1.34$, and they escape the system during the four first collisions with the boundary. Since the KAM-orbits escape the system fast and since there are no other regular trajectories, the average escape times are expected to be convergent for these r_{LR}.

Since the KAM island escapes quickly and affects the escape-time distribution only in short times, we must study the chaotic sea to understand the behavior of the escape-time distributions. The chaotic sea splits into a hyperbolic region and a sticky region. The sticky region is around the CFMUPO (see Sec. 3.5 for definitions) seen as a horizontal line in the collision map in Fig. 38(b) around $\cos(\theta) \approx -0.48$. The MUPOs are two-cycle orbits bouncing between the opposite sides of the table as demonstrated in Fig. 36(b).

As in Ref. [76], the splitting can be better visualized by calculating numerical approximations of the unstable manifold of the chaotic saddle at different time instants $t^* = 5, 30, 50$, and 100, which are shown in Fig. 39. During the early time-instants the hyperbolic component is dominant, but already at $t^* = 100$ the sticky set around the CFMUPO dominates the escape dynamics. The splitting of the saddle leads to an escape-time distribution that is (i) exponential at $t \lesssim t_z \approx 80$, apart from an initial, geometry dependent period $t \lesssim t_s \approx 5$, and (ii) has a power-law tail at $t \gtrsim t_z \approx 80$. We point out that the splitting of the saddle occurs for all

---

[22]The measure has been estimated by numerically estimating the area of the KAM island in the Poincaré section.

(a) $t^* = 5$

(b) $t^* = 30$

(c) $t^* = 50$

(d) $t^* = 100$
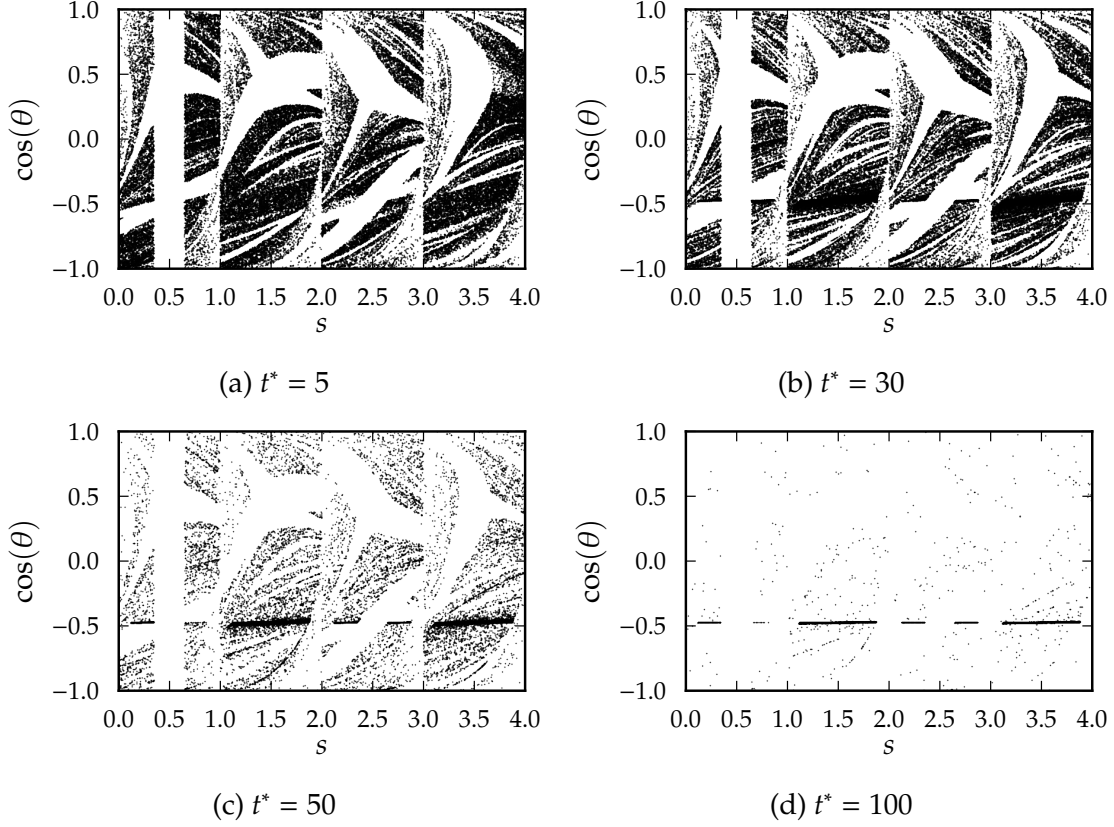
Figure 39: Numerical approximations of the unstable manifold of the open magnetic square billiards with the Larmor radius $r_{LR} = 1.05$ calculated at different times t^*.

r_{LR} around $r_{LR} = 1.05$, and the time-scales stay approximately the same.

An example escape-time distribution is shown for $r_{LR} = 1.05$ in Fig. 40, where the dashed vertical lines show the estimated time-instances $t_s = 5$ and $t_z = 80$. The red curve is the numerically calculated distribution, and the blue curve is a fit with Eq. (5.37) yielding the power-law exponent $\beta \approx 2.08$. As before, the fit is done by minimizing the relative error with the least squares method, and the initial period $t < t_s = 5$ is not included in the fitting range. In contrast to the divergent average escape times at $r_{LR} \approx 0.5075$, here the average escape time seems convergent at least for all $0.95 \lesssim r_{LR} \lesssim 1.2$.

Due to different time-scales (the initial period, the exponential period, and the power-law tail) we write the average escape-time integral of Eq. (5.35) as

$$\langle t_{\text{rel}} \rangle = \int_0^\infty t\rho(t, r_{LR})\, dt = \int_0^{t_s} t\rho(t, r_{LR})\, dt + \int_{t_s}^{t_z} t\rho(t, r_{LR})\, dt + \int_{t_z}^\infty t\rho(t, r_{LR})\, dt, \quad (5.38)$$

where we have split the integral over the different time-scales to see how the hyperbolic and the nonhyperbolic components of the chaotic saddle affect the average escape time. Numerically calculated values of the integrals are shown as a function of r_{LR} in Fig. 41.

84
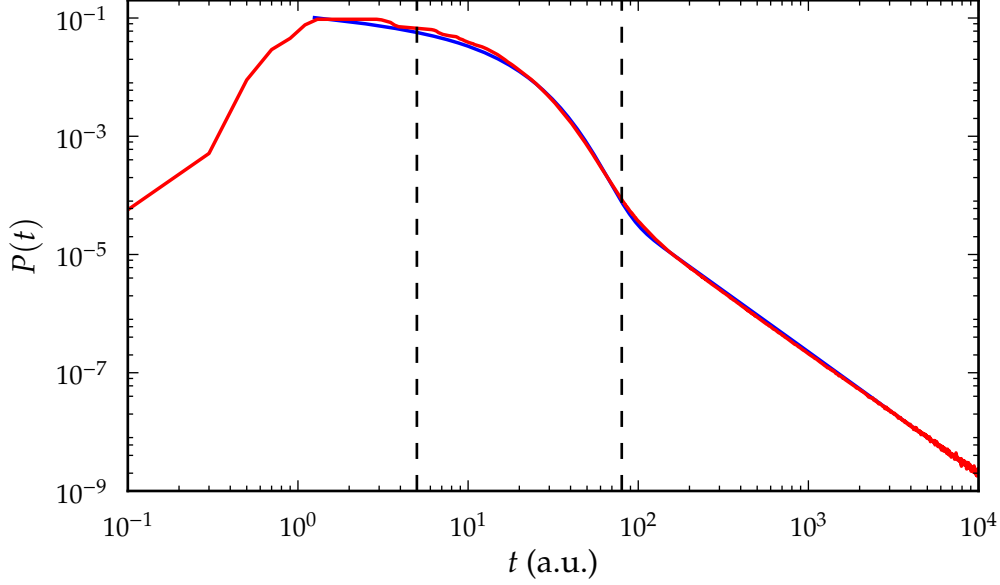
Figure 40: Numerically calculated escape-time distribution for open magnetic square billiards with the Larmor radius $r_{LR} = 1.05$ (red) and a fit to a combination of exponential and algebraic functions in Eq. (5.37) (blue). The dashed vertical lines show the time instants $t_s = 5$ and $t_z = 80$.

The behavior of the initial period [Fig. 41(e)] does not affect the behavior of the average escape time as a function of r_{LR} since the variations of the initial contribution for different r_{LR} are an order of magnitude smaller than the variations in the contribution from the hyperbolic and non-hyperbolic time-scales [see Fig. 41(a)]. The contribution to the integral from the hyperbolic component of the saddle has a minimum at $r_{LR} \approx 1.05$ [Fig. 41(c)]. The contribution of the power-law tail at the non-hyperbolic time-scale calculated up to $t = 10^5$ shows a monotonically increasing contribution as a function of r_{LR} [Fig. 41(d)]. However, we can not exclude the possibility that the contribution of the power-law tail would change if we calculated the integrals to longer times. Longer times could not be taken into account here due to (i) computational requirements when numerically calculating the escape-time distributions in long time-scales and (ii) the instability of extrapolation of the contribution of the power-law tail.

In total, the average escape time shows a minimum at $r_{LR} \approx 1.05$ [Fig. 41(b)]. This is likely the cause of the minimum of $\langle t_{rel} \rangle$ at $r_{ELR} \approx 1.05$ in the weak-interaction limit [Fig. 29(c)]. Furthermore, we point out that in the weak-interaction regime, the interaction can be expected to remove or reduce the contribution of the CFMUPO of the single-particle case so that it is indeed the changes in the hyperbolic component of the chaotic saddle which cause the minimum of the average relaxation time at $r_{ELR} \approx 1.05$.

Last, we note that even if relatively large sticky sets or KAM islands that are disconnected from the hole appear at higher r_{LR} such as, e.g., around $r_{LR} \approx 2.23$, these orbits are affected more by the Coulomb interaction due to large Larmor radius, and thus high peaks similar to $r_{ELR} \approx 0.5$ do not appear for higher r_{ELR}.

Figure 41: Contributions of different time-scales to the average escape-time integral in Eq. (5.38) as a function of the Larmor radius r_{LR}. Minimum of 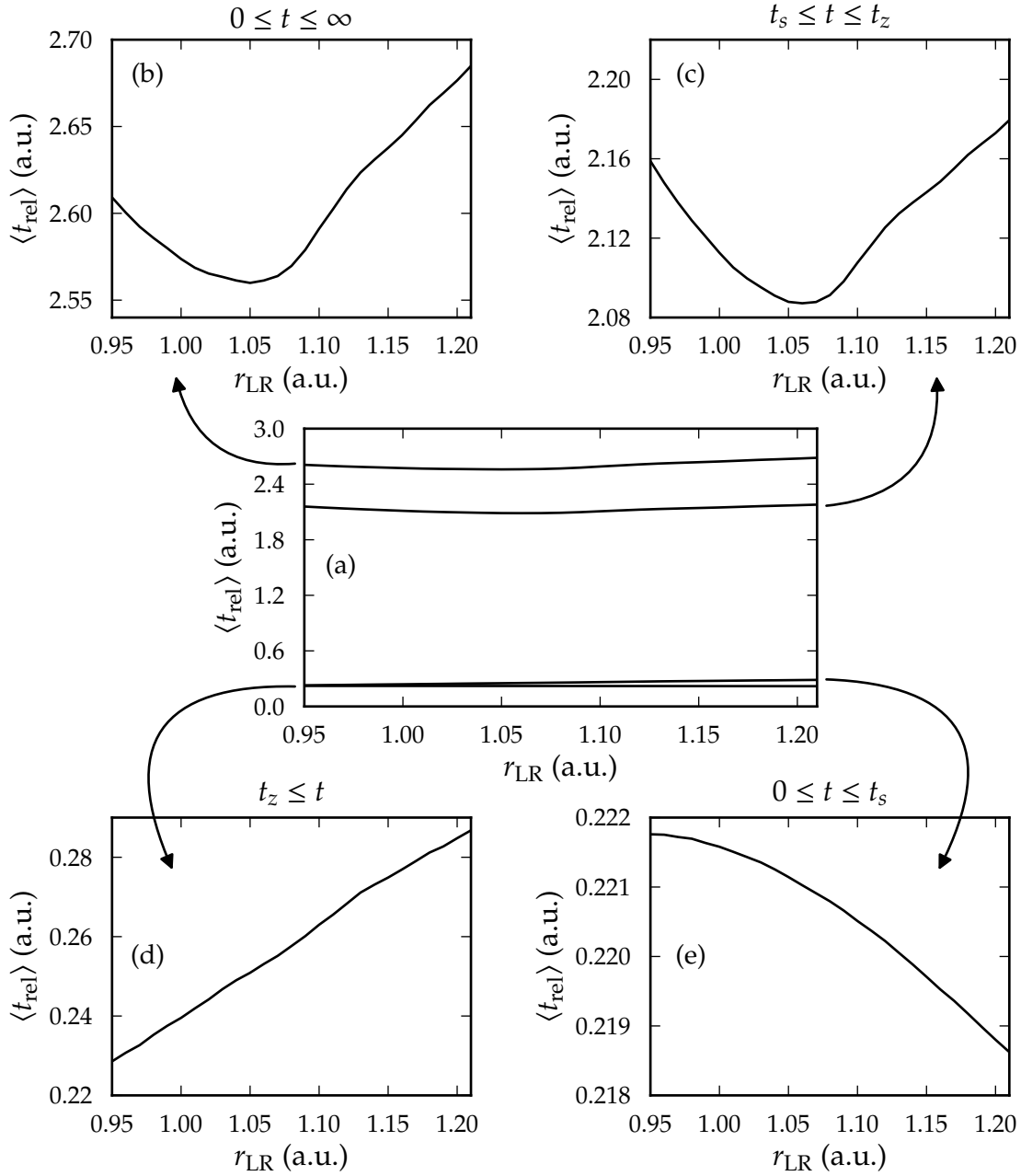the average escape time in (a) is caused by the changes in the hyperbolic component of the chaotic saddle [(b)]. Due to numerical reasons the integrals over the tail [(d)] have been calculated only up to $t = 10^5$.

5.2.5 Summary

To summarize, we have studied a diffusion process of $N = 9$ Coulomb interacting particles in a two-container billiards under a magnetic field. Initially all the particles are in one of the containers, and an equilibrium is reached when over half of the particles are in the other container.

We have demonstrated by the use of speed–time graphs and speed histograms that in the weak-interaction limit the particle speeds are affected by the Coulomb interaction only when the particles pass close to each other. In the intermediate-interaction regime, the speed–time graphs and the speed histograms demonstrate continuously changing speeds due to the interaction.

The average relaxation times have been calculated as of function the magnetic field B. To better describe the effects of the magnetic field especially in the intermediate-interaction regime, we have shown numerically that there exists a bijective map $B \to r_{\mathrm{ELR}}$, where the effective Larmor radius r_{ELR} describes the average effect of the magnetic field on the particles that are in the initial container. Furthermore, we have shown that the bijection depends on only one parameter, the interaction strength α.

The average relaxation times as a function of r_{ELR} were found to have general features across all interaction strengths: a rapid decrease as r_{ELR} increases from 0, a universal minimum around $r_{\mathrm{ELR}} \approx 0.3$, and asymptotic tendency to a constant value, which varies with α and the channel width Δ. The general features can be explained as the magnetic field and the Coulomb interaction dominating in different r_{ELR} regimes. The universal minimum was interpreted as the optimal balance between the magnetic field and the Coulomb interaction to allow for a fast relaxation.

In the weak-interaction limit, several additional extrema appear in the r_{ELR}-$\langle t_{\mathrm{rel}} \rangle$ graphs. Due to perturbative nature of the Coulomb interaction, we were successful in explaining these extrema using escape-time distributions of open single-particle magnetic square billiards. Changes in the escape-time distributions for different Larmor radii r_{LR} were attributed to changes in the phase space by calculating not-escaped sections of the phase space at different time instances.

6 Discussion

In this thesis we have addressed two systems relevant to the study of Coulomb-interacting many-body billiards: a two-particle circular billiards, which is summarized in Sec. 5.1.5 and the results have already been published in Ref. [88] (also found in Appx. E), and a few-particle diffusion process summarized in Sec. 5.2.5. In the studies we adopted the molecular dynamics approach to propagation of the systems, and when necessary, the results have been reproduced with different time-steps and sizes of ensembles to ensure reliability. In the following we discuss the insights into general Coulomb-interacting billiards obtained from our results.

At weak interactions the Coulomb interaction works as a perturbation in the systems, and thus the weakly interacting systems retain many of the properties of the underlying noninteracting system albeit slightly perturbed. This was seen as quasiregular bouncing maps and sticky escape-time distributions in the circular billiards, and in the diffusion process as the extrema in the average diffusion time graphs that arose from the changes in the phase space of open single-particle magnetic square billiards. This perturbative nature can be expected to be a general property of the Coulomb-interaction, i.e., independent of the billiard table or the confining potential. The perturbative nature also seems to be independent of the number of particles – at least in the few-particle limit. Furthermore, we may also expect to find perturbative behavior for other similar long-range interactions, such as the Yukawa interaction, in the weak-interaction limit. We note that perturbative nature of the Coulomb-interaction has been previously discussed, e.g., in Ref. [39] for one-dimensional lattices.

In the circular billiards, the perturbative regime was found to end already at low interactions strengths. However, in the noninteracting limit all the trajectories of the circular billiards are *parabolic* (marginally stable), so it would be of further interest to study whether systems with *elliptic* KAM islands in the noninteracting limit would retain regular features to higher interaction strengths.

The intermediate-interaction regime was found to be hyperbolic in the circular billiards in the studied time scales, and in the diffusion process the average relaxation times as a function of the effective Larmor radius behave alike throughout the intermediate-interaction regime. We expect the universal chaoticity at intermediate interaction strengths to be a general property of Coulomb-interacting billiards also in other tables; however, further studies should be conducted to confirm this.

We showed the strong-interaction limit of the two-particle circular billiards to be regular by calculating bouncing maps and by deriving an analytical model for the phase space trajectories. The analytical model is readily applicable to, e.g., the stadium billiards, which is hyperbolic in the noninteracting limit. In the strong-interaction limit of the stadium billiards, the particles will localize in the semi-circular caps. Also the Coulomb-interacting two-particle billiards in a square container has been shown to become (quasi)regular in the strong-interaction limit [95]. It is not known, however, if the (quasi)regularity at strong interactions occurs in all billiard tables. Further studies would also be required to see how the results of the strong-interaction limit change when considering more than two particles.

We note that also previous studies for interacting two-particle billiards have demonstrated some traces of quasi-regularity: in Ref. [41] the Coulomb-interacting two-particle square billiards in a magnetic field was shown to have some trajectories with quasi-regular properties, and, e.g., in Ref. [28] some signatures of sticky behavior were found both in the Coulomb-interacting and in the Yukawa-interacting two-body circular billiards. In contrast to these previous studies, we have thoroughly demonstrated the existence of sticky trajectories in the Coulomb-interacting circular billiards both in the weak and strong-interaction limits and shown the intermediate-interaction regime to be hyperbolic at the time scales we have studied.

Also, our conjectures on the universal effect of the Coulomb-interaction for different billiards in weak, intermediate, and possibly also in strong-interaction regime are drastically different to what has been found in soft potentials. For example, in a deformed harmonic oscillator chaoticity of Coulomb-interacting two-particle dynamics was found to depend heavily on the shape of the confining potential for all interaction strengths [34].

The diffusion process presented interesting phenomena as itself in addition to contributions to the above insights. Our study focused on a case where we had a uniquely corresponding single-particle system in the noninteracting limit. It would be of further interest to extend this study to different ensembles, e.g., with the initial velocities following the Maxwell-Boltzmann distribution. Also, a natural extension of the diffusion process would be to consider a transport process through a point contact both with a billiard model and also with a smooth potential landscape, which is a more realistic model for experimental setups.

Another significant contribution arising from this thesis is the *Bill2d* code, which has been expanded vastly during this research. *Bill2d* offers a fast, flexible, and expandable package applying the molecular dynamics approach to interacting many-body billiards, and it is readily applicable to several systems ranging from billiards to soft potentials and periodic lattices. The code is already being further used to study, e.g., the soft Lorentz gas, which is a prototype model that draws motivation from both the fundamentals of classical chaos (see, e.g., Ref. [98]) and also from recently fabricated artificial graphene-like structures [89–93]. Furthermore, we plan to publish the code in near future after implementing a few minor improvements.

References

[1] Steven H. Strogatz. *Nonlinear Dynamics And Chaos: With Applications To Physics, Biology, Chemistry, And Engineering*. Perseus Books Group, 1994.

[2] J. Gleick. *Chaos: Making a new science*. Penguin Books, 1988.

[3] R. C. Hilborn. *Chaos and Nonlinear Dynamics: An Introduction for Scientists and Engineers*. Oxford University Press, 2000.

[4] H.-O. Peitgen, H. Jürgens, and D. Saupe. *Chaos and Fractals: New Frontiers of Science*. Springer, 2004.

[5] A. E. Motter and D. K. Campbell. Chaos at fifty. *Phys. Today*, 55:27, 2013.

[6] B. P. Belousov. Периодически действующая реакция и ее механизм. Сборник рефератов по радиационной медицине, 147:145, 1959.

[7] A. M. Zhabotinsky. ериодический процесс окисления малоновой кислоты растворе. Биофизика, 9:306–311, 1964.

[8] J. D. Murray. *Mathematical Biology: I. An Introduction*. Springer, 2001.

[9] T. Matsumoto. A chaotic attractor from chua's circuit. *IEEE Transactions on Circuits and Systems*, CAS-31:1055–1058, 1984.

[10] G. A. Leonov, V. I. Vagaitsev, and N. V. Kuznetsov. Localization of hidden chua's attractors. *Physics Letters A*, 375:2230–2233, 2011.

[11] E. Ott. *Chaos in dynamical systems*. Cambridge University Press, 1994.

[12] K. Nakamura and T. Harayama. *Quantum Chaos and Quantum Dots*. Oxford University Press, Oxford, 2004.

[13] A. P. Micolich, A. M. See, B. C. Scannell, C. A. Marlow, T. P. Martin, I. Pilgrim, A. R. Hamilton, H. Linke, and R. P. Taylor. Is it the boundaries or disorder that dominates electron transport in semiconductor 'billiards'? *Fortschritte der Physik*, 61(2-3):332–347, 2013.

[14] A. Fuhrer, S. Lüscher, T. Heinzel, K. Ensslin, W. Wegscheider, and M. Bichler. Transport properties of quantum dots with steep walls. *Phys. Rev. B*, 63:125309, 2001.

[15] C. P. Dettmann and O. Georgiou. Transmission and reflection in the stadium billiard: Time-dependent asymmetric transport. *Phys. Rev. E*, 83:036212, 2011.

[16] L. A. Bunimovich. Mushrooms and other billiards with divided phase space. *Chaos*, 11:802–808, 2001.

[17] C. P. Dettmann and O. Georgiou. Open mushrooms: stickiness revisited. *J. Phys. A*, 44(19):195102, 2011.

[18] C. P. Dettmann and O. Georgiou. Survival probability for the stadium billiard. *Physica D*, 238(23–24):2395 – 2403, 2009.

[19] C. P. Dettmann and O. Georgiou. Quantifying intermittency in the open drivebelt billiard. *Chaos*, 22:026113, 2012.

[20] L. A. Bunimovich and C. P. Dettmann. Open circular billiards and the riemann hypothesis. *Phys. Rev. Lett.*, 94:100201, 2005.

[21] S. Lansel, M. A. Porter, and L. A. Bunimovich. One-particle and few-particle billiards. *Chaos*, 16:013129, 2006.

[22] S. Ranković and M. A. Porter. Two-particle circular billiards versus randomly perturbed one-particle circular billiards. *Chaos*, 23:013123, 2013.

[23] A. Awazu. Liquid-solid phase transition of a system with two particles in a rectangular box. *Phys. Rev. E*, 63:032102, 2001.

[24] C. Manchein and M. W. Beims. Gauss map and lyapunov exponents of interacting particles in a billiard. *Chaos, Solitions & Fractals*, 39:2041, 2007.

[25] H. A. Oliveira, C. Manchein, and M. W. Beims. Soft wall effects on interacting particles in billiards. *Phys. Rev. E*, 78:046208, 2008.

[26] L. Meza-Montes and S. E. Ulloa. Dynamics of two interacting particles in classical billiards. *Phys. Rev. E*, 55:R6319, 1997.

[27] L. A. Toporowicz and M. W. Beims. Correlation effects of two interacting particles in a circular billiard. *Physica A*, 371:5, 2006.

[28] M. W. Beims, C. Manchein, and J. M. Rost. Origin of chaos in soft interactions and signatures of nonergodicity. *Phys. Rev. E*, 76:056203, 2007.

[29] A. M. See, I. Pilgrim, B. C. Scannell, R. D. Montgomery, O. Klochan, A. M. Burke, M. Aagesen, P. E. Lindelof, I. Farrer, D. A. Ritchie, R. P. Taylor, A. R. Hamilton, and A. P. Micolich. Impact of small-angle scattering on ballistic transport in quantum dots. *Phys. Rev. Lett.*, 108:196807, May 2012.

[30] C. M. Marcus, A. J. Rimberg, R. M. Westervelt, P. F. Hopkins, and A. C. Gossard. Conductance fluctuations and chaotic scattering in ballistic microstructures. *Phys. Rev. Lett.*, 69:506–509, Jul 1992.

[31] L. P. Kouwenhoven, D. G. Austing, and S. Tarucha. Few-electron quantum dots. *Rep. Prog. Phys*, 64:701, 2001.

[32] S. M. Reimann and M. Manninen. Electronic structure of quantum dots. *Rev. Mod. Phys.*, 74:1283–1342, Nov 2002.

[33] R. G. Nazmitdinov, N. S. Simonovic, and J.-M. Rost. Semiclassical analysis of a two-electron quantum dot in a magnetic field: Dimensional phenomena. *Phys. Rev. B*, 65:155307, 2002.

[34] S. Radionov, S. Åberg, and T. Guhr. Regularity and chaos in interacting two-body systems. *Phys. Rev. E*, 70:036207, 2004.

[35] P. S. Drouvelis, P. Schmelcher, and F. K. Diakonos. Two-electron anisotropic quantum dots. *Europhys. Lett.*, 64:232, 2003.

[36] P. S. Drouvelis, P. Schmelcher, and F. K. Diakonos. Global view on the electronic properties of two-electron anisotropic quantum dots. *Phys. Rev. B*, 69:035333, 2004.

[37] S. Schröter, P.-A. Hervieux, G. Manfredi, J. Eiglsperger, and J. Madroñero. Exact treatment of planar two-electron quantum dots: Effects of anharmonicity on the complexity. *Phys. Rev. B*, 87:155413, Apr 2013.

[38] A. Knauf. Ergodic and topological properties of coulombic periodic potentials. *Comm. Math. Phys.*, 110:89, 1987.

[39] B. Liebchen, F. K. Diakonos, and P. Schmelcher. Interaction-induced current-reversals in driven lattices. *New J. Phys*, 14:103032, 2012.

[40] S. I. Denisov, E. S. Denisova, and P. Hänggi. Ratchet transport for a chain of interacting charged particles. *Phys. Rev. E*, 71:016104, 2005.

[41] M. Aichinger, S. Janecek, and E. Räsänen. Billiards in magnetic fields: A molecular dynamics approach. *Phys. Rev. E*, 81:016703, 2010.

[42] M. C. Gutzwiller. *Chaos in Classical and Quantum Mechanics*. Springer-Verlag, 1990.

[43] See, e.g., H. van Houten and C. W. J. Beenakker. Quantum point contacts. *Phys. Today*, 49:22, 1996.

[44] A. Guderian, G. Dechert, K.-P. Zeyer, and F. W. Schneider. Stochastic resonance in chemistry. 1. the Belousov-Zhabotinsky reaction. *J. Phys. Chem.*, 100(11):4437–4441, 1996.

[45] B. Z. Shakhashiri. *Chemical Demonstrations, Volume 2: A Handbook for Teachers of Chemistry*. Univ of Wisconsin Press, 1985.

[46] E. N. Lorenz. Deterministic nonperiodic flow. *Journal of the Atmospheric Sciences*, 20:130–141, 1963.

[47] H. Goldstein, C. Poole, and J. Safko. *Classical Mechanics*. Addison-Wesley Press, 2001.

[48] P. L. Maupertuis. *Accord de différentes loix de la nature qui avoient jusqu'ici paru incompatibles*. 1744.

[49] P. L. Maupertuis. *Les loix du mouvement et du repos déduites d'un principe metaphysique*. 1746.

[50] O. D. Johns. *Analytical Mechanics for Relativity And Quantum Mechanics*. Oxford University Press, 2005.

[51] M. Robnik and M. V. Berry. Classical billiards in magnetic fields. *J. Phys. A.: Math. Gen.*, 18:1361–1378, 1985.

[52] N. Berglund and H. Kunz. Integrability and ergodicity of classical billiards in a magnetic field. *J. Stat. Phys.*, 83:81, 1996.

[53] A. Kaplan, N. Friedman, M. Andersen, and N. Davidson. Observation of islands of stability in soft wall atom-optics billiards. *Phys. Rev. Lett.*, 87:274101, 2001.

[54] A. M. Lyapunov. *General problem of the stability of motion (in Russian)*. PhD thesis, Moscow University, 1892.

[55] V. I. Oseledets. A multiplicative ergodic theorem. Lyapunov characteristic numbers for dynamical systems. *Trans.Moscow Math. Soc.*, 19:197–231, 1968.

[56] L. A. Bunimovich, S. G. Dani, R. L. Dobrushin, M. V. Jakobson, I. P. Kornfeld, N. B. Maslova, Ya. B. Pesin, J. Smillie, Yu. M. Sukhov, A. M. Vershik, and Ya. G. Sinai. *Dynamical Systems, Ergodic Theory and Applications*. Perseus Books Group, 1994.

[57] P. Ghatage and S. Shao. Linear transformation of the unit circle in $\mathbb{R}^2$. *The College Mathematics Journal*, 32:204–206, 2001.

[58] A. Wolf, J. B. Swift, H. L. Swinney, and J. A. Vastano. Determining lyapunov exponents from a time series. *Physica D*, 16:285–317, 1984.

[59] Z. Kaufmann and H. Lustfeld. Comparison of averages of flows and maps. *Phys. Rev. E*, 64:055206(R), 2001.

[60] M. Audin. *Torus Actions On Symplectic Manifolds*. Springer-Verlag, 2004.

[61] V. I. Arnold, A. Weinstein, and K. Vogtmann. *Mathematical Methods Of Classical Mechanics*. Springer, 1989.

[62] J. V. José and E. J. Saletan. *Classical Dynamics: A Contemporary Approach*. Cambridge University Press, 1998.

[63] E. A. Jackson. *Perspectives of Nonlinear Dynamics Vol. 2*. Cambridge University Press, 1990.

[64] A. N. Kolmogorov. On conservation of conditionally periodic motions for a small change in Hamilton's function. *Dokl. Akad. Nauk SSSR*, 98:527–530, 1954.

[65] V. I. Arnold. Proof of a theorem of A. N. Kolmogorov on the preservation of conditionally periodic motions under a small perturbation of the Hamiltonian. *Uspehi Mat. Nauk*, 18:13–40, 1963.

[66] J. Moser. On invariant curves of area-preserving mappings of an annulus. *Nachr. Akad. Wiss. Göttingen Math.-Phys.*, 2:1–20, 1963.

[67] M. V. Berry. Regularity and chaos in classical mechanics, illustrated by three deformations of a circular billiard. *Eur. J. Phys.*, 2:91–102, 1981.

[68] B. L. Hao. *Directions in chaos Vol. 1*. World Scientific, 1987.

[69] L. Pecko. *Differential Equations and Dynamical Systems*. Springer, 2001.

[70] M. Queffelec. *Substitution Dynamical Systems - Spectral Analysis*. Springer, 2010.

[71] Y. G. Sinai. Dynamical systems with elastic reflections. *Russian Mathematical Surveys*, 25:137–191, 1970.

[72] Y. G. Sinai. On the foundations of the ergodic hypothesis for a dynamical system of statistical mechanics. *Sov. Math Dokl*, 4:1818–1822, 1963.

[73] L. A. Bunimovich. On billiards close to dispersing. *Mathematical USSR Sbornik*, 95:49–73, 1974.

[74] L. A. Bunimovich. The ergodic properties of certain billiards. *Funkt. Anal. Prilozh.*, 8:73–74, 1974.

[75] L. A. Bunimovich and L. V. Vela-Arevalo. Many faces of stickiness in hamiltonian systems. *Chaos*, 22:026103, 2012.

[76] E. G. Altmann, J. S. E. Portela, and T. Tél. Leaking chaotic systems. *Rev. Mod. Phys.*, 85:869, 2013.

[77] Y.-C. Lai and T. Tamas. *Transient Chaos: Complex Dynamics on Finite-Time Scales*. Springer, 2011.

[78] L. A. Bunimovich and C. P. Dettmann. Peeping at chaos: Nondestructive monitoring of chaotic systems by measuring long-time escape rates. *Europhys. Lett.*, 80(4):40001, 2007.

[79] M. Dhamala and Y.-C. Lai. The natural measure of nonattracting chaotic sets and its representation by unstable periodic orbits. *International Journal of Bifurcation and Chaos*, 12:2991–3005, 2002.

[80] N. Buric, A. Rampioni, G. Turchetti, and S. Vaienti. Weak chaos and Poincaré recurrences for area preserving maps. *Journal of Physics A: Math. and Gen.*, 36:L209, 2003.

[81] E. P. S. Xavier, M. C. Santos, L. G. G. V. Dias da Silva, M. G. E. da Luz, and M. W. Beims. Quantum chaos for two interacting particles confined to a circular billiard. *Physica A*, 342:377, 2004.

[82] S. Sawada, A. Terai, and K. Nakamura. Coulomb-interaction-induced quantum irregularity in two electrons within a hard-walled circular billiard. *Chaos, Solitons & Fractals*, 40:862, 2009.

[83] M. Tuckerman, G. J. Berne, and G. J. Martyna. Reversible multiple time scale molecular dynamics. *J. Chem. Phys*, 97:1990–2001, 1992.

[84] See, e.g., M. Suzuki. Decomposition formulas of exponential operators and lie exponentials with some applications to quantum mechanics and statistical physics. *J. Math. Phys*, 26:601, 1985.

[85] M. P. Allen and D. J. Tildesley. *Computer Simulation of Liquids*. Oxford University Press, USA, 1989.

[86] Q. Spreiter and M. Walter. Classical molecular dynamics simulation with the velocity verlet algorithm at strong external magnetic field. *Journal of Computational Physics*, 152:102–119, 1999.

[87] J. Solanpää, P. J. J. Luukko, and E. Räsänen. Many-particle dynamics and intershell effects in Wigner molecules. *J. Phys. Condens. Matter*, 23:395602, 2011.

[88] J. Solanpää, J. Nokelainen, P. J. J. Luukko, and E. Räsänen. Coulomb-interacting billiards in circular cavities. *J. Phys. A: Math. Theor.*, 46:235102, 2013.

[89] C.-H. Park and S. G. Louie. Making massless Dirac fermions from a patterned two-dimensional electron gas. *Nano Letters*, 9(5):1793–1797, 2009. PMID: 19338276.

[90] M. Gibertini, A. Singha, V. Pellegrini, M. Polini, G. Vignale, A. Pinczuk, L. N. Pfeiffer, and K. W. West. Engineering artificial graphene in a two-dimensional electron gas. *Phys. Rev. B*, 79:241406, Jun 2009.

[91] A. Singha, M. Gibertini, B. Karmakar, S. Yuan, M. Polini, G. Vignale, M. I. Kastnelson, A. Pinczuk, L. N. Pfeiffer, K. W. West, and V. Pellegrini. Two-dimensional Mott-Hubbard electrons in an artificial honeycomb lattice. *Science*, 332:1176, 2011.

[92] E. Räsänen, C. A. Rozzi, S. Pittalis, and G. Vignale. Electron-electron interactions in artificial graphene. *Phys. Rev. Lett.*, 108:246803, Jun 2012.

[93] K. K. Gomes, W. Mar, W. Ko, F. Guinea, and H. C. Manoharan. Designer Dirac fermions and topological phases in molecular graphene. *Nature*, 483:306, 2012.

[94] J. Solanpää. Bill2d – *A molecular dynamics approach to simulation of billiards*. Special assignment, University of Jyväskylä, 2013.

[95] Johannes Nokelainen. *Chaotic properties of classical Coulomb-interacting few-particle billiards*. B.Sc. thesis, University of Jyväskylä, 2013.

[96] W. Bauer and G. F. Bertsch. Decay of ordered and chaotic systems. *Phys. Rev. Lett.*, 65:2213–2216, Oct 1990.

[97] H. Alt, H.-D. Gräf, H. L. Harney, R. Hofferbert, H. Rehfeld, A. Richter, and P. Schardt. Decay of classical chaotic systems: The case of the Bunimovich stadium. *Phys. Rev. E*, 53:2217–2222, Mar 1996.

[98] Y. G. Sinai. Ergodic properties of the Lorentz gas. *Functional Analysis and Its Applications*, 13(3):192–202, 1979.

Appendices

A Calculation of Poincaré section in one-dimensional two-particle Coulomb-interacting billiards

In this section we demonstrate how to calculate a Poincaré section of a system. As an example, we use one-dimensional two-particle Coulomb interacting billiards, where the particles, labeled by 1 and 2, are confined to the interval $q \in [0, 1]$. The Hamiltonian [Eq. (4.16)] describing the system is

$$H = \frac{1}{2} \left(p_1^2 + p_2^2 \right) + \frac{\alpha}{q_2 - q_1}, \tag{A.1}$$

where q_1 and q_2 are the generalized coordinates and p_1 and p_2 the generalized momenta. Without any loss of generality, we have chosen $q_1 < q_2$.

The energy of the system is fixed to $H = 1$ so that the interaction strength α has the limits $0 \leq \alpha \leq 1$ (for details see Sec. 4.1). For our demonstration, we choose $\alpha = 1/2$.

First thing to do is to use the available conservation laws to reduce the number of coordinates. Restricting ourselves to the energy surface $H = 1$ allows us to describe p_2 as

$$p_2 = \sqrt{2 - \frac{2\alpha}{q_2 - q_1} - p_1^2}, \tag{A.2}$$

where we have chosen to consider only positive values of p_2.

We define the Poincaré section (collision map)

$$S = \{(q_1, q_2, p_1, p_2) \,|\, q_2 = 1\}, \tag{A.3}$$

which corresponds to collisions of the particle 2 with the boundary at $q = 1$. The Poincaré section S is a two-dimensional surface that can be fully parametrized with q_1 and p_2.

First we propagate a large ensemble of trajectories with random initial conditions and record all their crossings with the Poincaré section S. This allows us to see the structure of the phase space. Next, to clear up the figure, we choose a few trajectories with which the structures of the phase space are demonstrated clearly and show only the crossings of these hand-picked trajectories with the Poincaré section S.

The resulting Poincaré section is shown in Fig. 42. The system has a mixed phase space with multiple KAM-islands. It is noteworthy that the structure of the phase space has qualitative similarities to the Poincaré section in one dimensional system with two Yukawa-interacting particles for certain parameters.

For Yukawa-interactions (screened Coulomb) the interaction potential is

$$V(q_1, q_2) = \frac{\exp(-\lambda|q_1 - q_2|)}{|q_1 - q_2|},$$

(A.4)

where λ is the screening parameter.

To demonstrate the similarities, we show in Fig. 43 the Poincaré section for the Yukawa-interacting billiards with the total energy $H = 1.56$ and the screening parameter $\lambda = 0.6$. We point out that the Yukawa-interacting system, including the Poincaré section we show here, has already been studied in Ref. [26]. The KAM-islands of the Yukawa-interacting system with these parameters are remarkably similar to the islands in the Coulomb-interacting system: the positions and the structure of the islands are roughly the same for both systems. However, there are likely to be small scale differences in the structures of the phase spaces, as as already seen in the islands at $q_1 \gtrsim 0.4$.
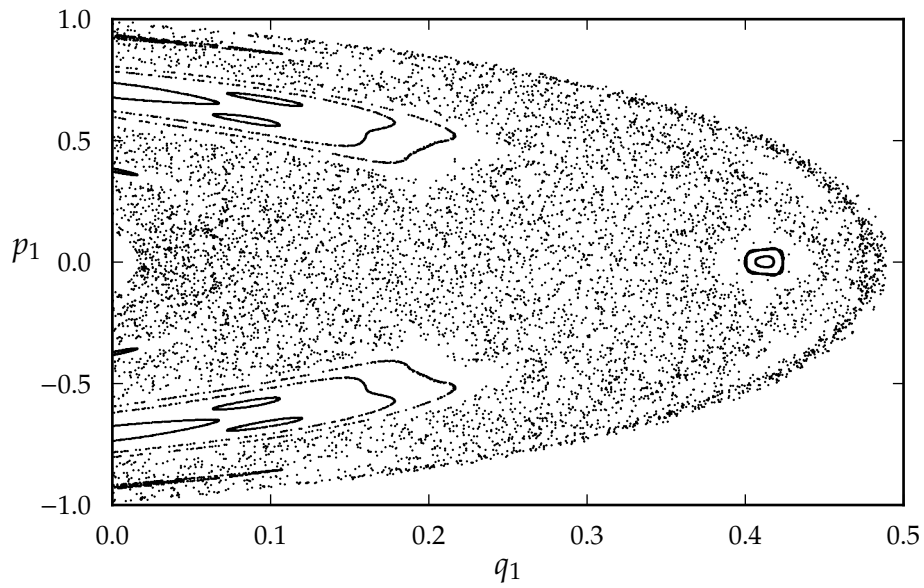
Figure 42: Poincaré section of one-dimensional two-particle Coulomb-interacting billiards with the total energy $H = 1$ and the interaction strength $\alpha = 0.5$.
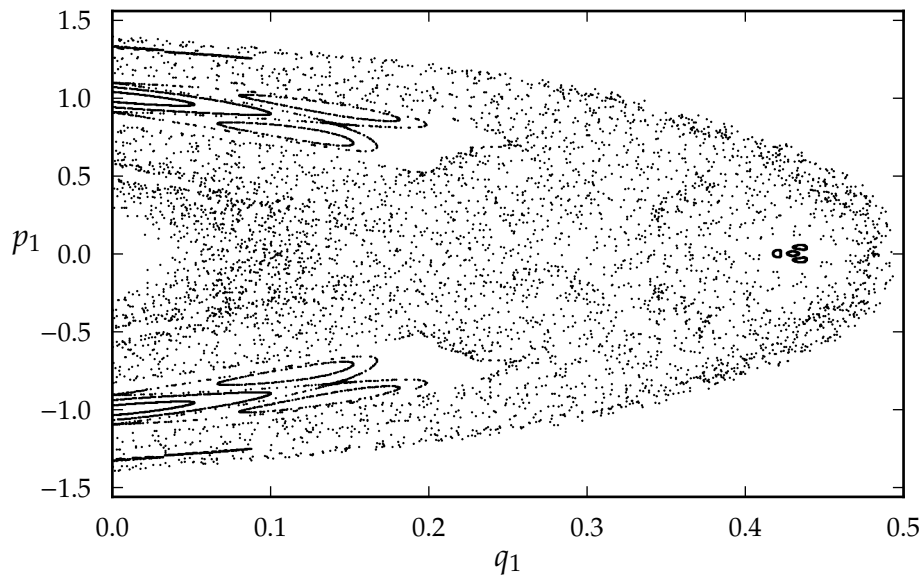

Figure 43: Poincaré section of one-dimensional two-particle Yukawa-interacting billiards with the total energy $H = 1.56$ and the screening parameter $\lambda = 0.6$. This was first calculated in Ref. [26].

B Scale transformations for equalization of geometrically similar Hamiltonian systems with magnetic and electric fields

The essential difference between different energy and length scales of a Coulomb-interacting many-body system is the effect of the Coulomb interaction on the dynamics. For example, the Coulomb interaction has little effect on the system if the total energy of the system is high compared to the (Coulomb) interaction energy.

To obtain a variable to describe the strength of the Coulomb interaction, we show in the following that every energy and length scale of a Coulomb-interacting many-body system can be reduced to a fixed energy and length scale of a geometrically similar system by (i) introducing a scale parameter in the Hamiltonian to describe the strength of the Coulomb interaction and (ii) rescaling the scalar and vector potentials, if present.

Note, however, that the theorem holds only for a specific form of the Hamiltonian. To motivate the form, we first calculate the Hamiltonian of a Coulomb-interacting many-body system of equally charged particles under stationary scalar and vector potentials. The Lagrangian of such system is

$$L = \sum_i \frac{1}{2} m_e \dot{r}_i^2 - \sum_{i<j} \frac{q_e^2}{4\pi\epsilon_0} \frac{1}{\left\| r_i - r_j \right\|} + \frac{q_e}{c} \sum_i \dot{r}_i \cdot A(r) - \sum_i q_e \phi(r_i), \qquad \text{(B.1)}$$

where r_i and $\dot{r}_i$ are the position and velocity of the ith particle, respectively; m_e and q_e the mass and the charge of the particles; c the speed of light; A the vector potential; and ϕ the scalar potential. In the sums, the indices i and j run over all the particles.

By introducing Hartree atomic units (a.u.), such that $q_e = m_e = \frac{1}{4\pi\epsilon_0} = 1$, the Lagrangian reduces to

$$L = \frac{1}{2} \sum_i \dot{r}_i^2 - \sum_{i<j} \frac{1}{\left\| r_i - r_j \right\|} + \sum_i \dot{r}_i \cdot A(r_i) - \sum_i \phi(r_i), \qquad \text{(B.2)}$$

where we have absorbed the speed of light in a.u., $c \approx 137.036$, into the vector potential A.

Next we transform into the Hamiltonian formalism. By choosing the generalized coordinates for the ith particle, q_i, as the cartesian coordinates r_i, we get the generalized momentum

$$p_i = \nabla_{\dot{r}_i} L = \dot{r}_i + A(r_i), \qquad \text{(B.3)}$$

i.e., the cartesian velocity corresponds to the generalized momentum minus the vector potential.

The Hamiltonian yielding the equations of motion is obtained from Eq. (2.14),

which gives

$$H = \frac{1}{2} \sum_i \left[p_i - A(r_i) \right]^2 + \sum_{i<j} \frac{1}{\|r_i - r_j\|} + \sum_i \phi(r_i). \tag{B.4}$$

Motivated by the form of the Hamiltonian in Eq. (B.4), we will next derive the following theorem.

Theorem 2
All systems with Hamiltonians of form

$$H(q, p, t) = \frac{1}{2} \sum_i \left[p_i - A(q_i) \right]^2 + \sum_{i<j} \frac{1}{\|q_i - q_j\|} + \sum_i \phi(q_i) \tag{B.5}$$

can be reduced to a fixed energy and length scale of a Hamiltonian system that is described by a new set of coordinates (Q, P, T) of the extended phase space and the Hamiltonian

$$K(Q, P, T) = \frac{1}{2} \sum_i \left[P_i - \tilde{A}(Q_i) \right]^2 + \sum_{i<j} \frac{\alpha}{\|Q_i - Q_j\|} + \sum_i \tilde{\phi}(Q_i), \tag{B.6}$$

where α is a scaling parameter called the *interaction strength* that depends on the length and energy scales, and $\tilde{A}$ and $\tilde{\phi}$ are rescaled vector and scalar potentials.

Proof. To prove the theorem, we derive the scale transformations that yield the desired form of the Hamiltonian. We begin by scale transformation of the phase space coordinates

$$(q_i, p_i, t) \rightarrow (Q_i = \gamma q_i, P_i = \beta^{1/2} p_i, t). \tag{B.7}$$

Here γ is defined by the desired length scale and β by the energy scale as we will see during the proof. The Hamiltonian that yields the equations of motion for the new coordinates (Q_i, P_i, t) is given by Eq. (2.41), which yields

$$K(Q_i, P_i, t) = \beta^{1/2} \gamma H(Q_i, P_i, t) = \frac{1}{2} \sum_i \beta^{-1/2} \gamma \left[P_i - \tilde{A}(Q_i) \right]^2$$

$$+ \sum_{i<j} \frac{\beta^{1/2} \gamma^2}{\|Q_i - Q_j\|} + \beta^{1/2} \gamma \sum_i \phi(Q_i), \tag{B.8}$$

where the vector potential has been rescaled by

$$A \rightarrow \tilde{A}(Q_i) = \beta^{1/2} A(Q_i). \tag{B.9}$$

Note the use of the notation $f(q_i(Q_i), p_i(P_i)) \doteq f(Q_i, P_i)$.

The equations of motion are obtained from Eqs. (2.17) and (2.18) yielding

$$\frac{d\boldsymbol{Q}_i}{dt} = \nabla_{P_i} K = \beta^{-1/2}\gamma\left[\boldsymbol{P}_i - \tilde{A}(\boldsymbol{Q}_i)\right] \tag{B.10}$$

$$\frac{d\boldsymbol{P}_i}{dt} = -\nabla_{Q_i} K = -\sum_{j\neq i}\frac{\beta^{1/2}\gamma^2}{\|\boldsymbol{Q}_i - \boldsymbol{Q}_j\|^3}\left(\boldsymbol{Q}_i - \boldsymbol{Q}_j\right)$$

$$+ \beta^{-1/2}\gamma\sum_i\left[\boldsymbol{P}_i - \tilde{A}(\boldsymbol{Q}_i)\right]\cdot\nabla_{Q_i}\tilde{A}(\boldsymbol{Q}_i) - \beta^{1/2}\gamma\nabla_{Q_i}\phi(\boldsymbol{Q}_i). \tag{B.11}$$

In order to further simplify these equations, we need to reparameterize time,

$$T(t) = \beta^{-1/2}\gamma t, \tag{B.12}$$

which gives us

$$\frac{d\boldsymbol{Q}_i}{dT} = \beta^{1/2}\gamma^{-1}\frac{d\boldsymbol{Q}_i}{dt} \overset{(4.9)}{=} \left[\boldsymbol{P}_i - \tilde{A}(\boldsymbol{Q}_i)\right] \tag{B.13}$$

$$\frac{d\boldsymbol{P}_i}{dT} = \beta^{1/2}\gamma^{-1}\frac{d\boldsymbol{P}_i}{dt} \overset{(4.10)}{=} -\sum_{j\neq i}\frac{\beta\gamma}{\|\boldsymbol{Q}_i - \boldsymbol{Q}_j\|^3}\left(\boldsymbol{Q}_i - \boldsymbol{Q}_j\right)$$

$$+ \sum_i\left[\boldsymbol{P}_i - \tilde{A}(\boldsymbol{Q}_i)\right]\cdot\nabla_{Q_i}\tilde{A}(\boldsymbol{Q}_i) - \nabla_{Q_i}\tilde{\phi}(\boldsymbol{Q}_i), \tag{B.14}$$

where we have absorbed β into the scalar potential ϕ by rescaling

$$\phi(\boldsymbol{Q}_i) \to \tilde{\phi}(\boldsymbol{Q}_i) = \beta\phi(\boldsymbol{Q}_i). \tag{B.15}$$

Denoting $\alpha = \beta\gamma$, the Hamiltonian corresponding to equations of motion (4.12) and (4.13) is

$$K(\boldsymbol{Q}, \boldsymbol{P}, T) = \frac{1}{2}\sum_i\left[\boldsymbol{P}_i - \tilde{A}(\boldsymbol{Q}_i)\right] + \sum_{i<j}\frac{\alpha}{\|\boldsymbol{Q}_i - \boldsymbol{Q}_j\|} + \sum_i\tilde{\phi}(\boldsymbol{Q}_i), \tag{B.16}$$

which can easily be checked with Eqs. (2.17) and (2.18).

In summary, to transform to the length and energy scale defined by γ and β, respectively, we make a transformation in the extended phase space,

$$(\boldsymbol{q}, \boldsymbol{p}, t) \to (\boldsymbol{P} = \beta^{1/2}\boldsymbol{p}, \boldsymbol{Q} = \gamma\boldsymbol{q}, T = \beta^{-1/2}\gamma t), \tag{B.17}$$

which must be accompanied by rescaling of the vector and scalar potentials as

$$A \to \tilde{A}(\boldsymbol{Q}_i) = \beta^{1/2}A(\boldsymbol{Q}_i) \tag{B.18}$$

$$\phi \to \tilde{\phi}(\boldsymbol{Q}_i) = \beta\phi(\boldsymbol{Q}_i t), \tag{B.19}$$

which give the Hamiltonian for the new variables $(\mathbf{Q}, \mathbf{P}, T)$,

$$
\begin{aligned}
K(\mathbf{Q}, \mathbf{P}, T) &= \beta H(\mathbf{Q}, \mathbf{P}, t) \\
&= \frac{1}{2} \sum_i \left[\mathbf{P}_i - \tilde{\mathbf{A}}(\mathbf{Q}_i) \right] + \sum_{i<j} \frac{\alpha}{\|\mathbf{Q}_i - \mathbf{Q}_j\|} + \sum_i \tilde{\phi}(\mathbf{Q}_i),
\end{aligned}
\tag{B.20}
$$

where $\alpha = \beta\gamma$. $\qquad\square$

To emphasize, all length and energy scales of geometrically similar systems can be reduced to a single constant energy surface, e.g. $K(\mathbf{Q}, \mathbf{P}, T) = 1$, of the system with the Hamiltonian $K(\mathbf{Q}, \mathbf{P}, T)$.

We conclude our discussion on the scale transformations by a short demonstration. The propagation scheme is the modified velocity Verlet algorithm for arbitrary magnetic fields described in Sec. 4.2 with the time-step $\Delta t = 10^{-5}$. As a reference system we take a square billiard table with the side length 2 under a magnetic field of strength $B = 3$ perpendicular to the table. Two Coulomb-interacting particles are given the total energy $E = 3$ (with $\alpha = 1$) and propagated up to $t = 15$. The resulting trajectory is shown in Fig. 44(a).

Next, we wish to calculate the same trajectory in a system where the length of the side of the table is 1 and the total energy of the system $E = 1$. These give us $\beta = 1/3$ and $\gamma = 1/2$, and thus $\alpha = \beta\gamma = 1/6$. Using the scaling transformations of Eq. (B.17), we obtain the propagation time $t \approx 13$. Finally, to get the value of the magnetic field, we remind that $\mathbf{B} = \nabla \times \mathbf{A}$, i.e., the strength of the rescaled magnetic field is $\tilde{B} = \gamma^{-1}\beta^{1/2}B = 6/\sqrt{3}$, where the factor γ^{-1} comes from the rescaling of length in the derivative and the factor $\beta^{1/2}$ from the rescaling of the vector potential according to Eq. (B.18).

The trajectory calculated in the rescaled system is shown in Fig. 44(b), and it is the equivalent of the trajectory in Fig. 44(a), as it should be. Minor differences near the end of the simulation are due to numerical errors in the simulation which are important in the long run due to hyperbolicity of the trajectory.
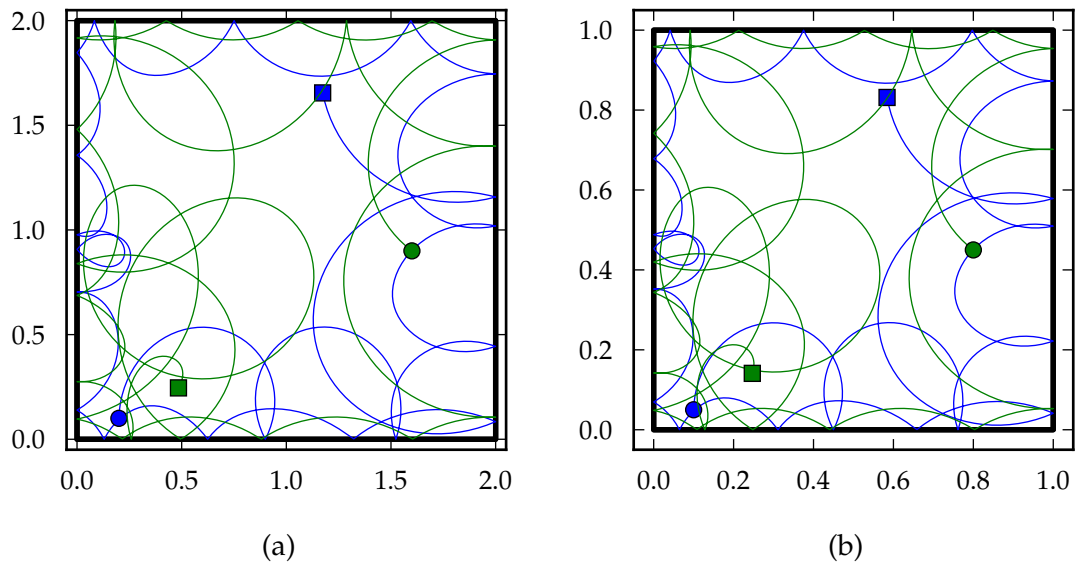
Figure 44: The same trajectories calculated by rescaling the length and energy scales of the system. The initial positions are marked with circles and the final positions with squares. The parameters are given in the text.

C Efficient propagation algorithm for magnetic single-particle rectangular billiards

We document here an efficient algorithm for the propagation of magnetic single particle billiards with a rectangular table. The algorithm was originally developed and implemented with *Python* by Visa Nummelin. For this thesis we have redone the implementation to make it faster by rewriting the algorithm as a Python module using C++ via the *Python API* defined in the C-header *Python.h*.

1. As an input the algorithm takes the initial point in phase space, $I = (x_0, y_0, \theta_0)$, where x_0 and y_0 are the cartesian coordinates and $\theta_0 \in [-\pi, \pi]$ is the oriented angle of the direction of velocity v as shown in Fig. 45(a). The lengths of the sides of the rectangle are denoted by L_x and L_y, the Larmor radius by r, and the speed of the particle by v.

Input: $I = (x_0, y_0, \theta_0)$, L_x, L_y, r, and v

---

2. The centerpoint C of the circular trajectory is calculated [see Fig. 45(b) for the geometry from which this step is calculated]. Notice that the traveling direction on the circular trajectory is chosen to be clockwise, i.e., we fix the direction of the magnetic field.

$C \leftarrow (x_0 + r\sin(\theta_0), y_0 - r\cos(\theta_0))$

---

3. All possible points of collision with the boundary are calculated. This is done by considering a circle of radius r centered at C and calculating all its crossings with the boundary. Due to fixing of the traveling direction, we can eliminate one crossing with each side from the calculation. In Fig. 45(c) we visualize this step of the algorithm. The possible collision points are marked with arrows, and the triangle, from which the coordinates of one of the possible collision points can be calculated by Pythagorean theorem, is shown.

If no crossings are found, the particle does not collide with the boundary.

if $|C_x| \leq r$ **then**

 possible_points_of_collision $\xleftarrow{\text{append}}$ $(0, C_y - \sqrt{r^2 - C_x^2})$

end if

if $|C_y| \leq r$ **then**

 possible_points_of_collision $\xleftarrow{\text{append}}$ $(C_x + \sqrt{r^2 - C_y^2}, 0)$

end if

if $|L_x - C_x| \leq r$ **then**

 possible_points_of_collision $\xleftarrow{\text{append}}$ $(L_x, C_y + \sqrt{r^2 - (L_x - C_x)^2})$

end if

if $|L_y - C_y| \leq r$ **then**

 possible_points_of_collision $\xleftarrow{\text{append}}$ $(C_x - \sqrt{r^2 - (L_y - C_y)^2}, L_y)$

end if

if possible_points_of_collision is empty **then**

 `End program:  no collisions`

end if

---

4. The correct point of collision is chosen from the list *possible_points_of_collision*. This is done by first calculating the distance s when traveling clockwise along the circular arc from the initial point I to each possible collision point P and then selecting the point corresponding to the shortest path.

$s = 2\pi r$

for P_i in possible_points_of_collision **do**

 $s_{\text{temp}} \leftarrow r \arccos\left[\frac{(I-C)\cdot(P_i - C)^2}{r^2}\right]$

 if $(I - C)_x (P_i - C)_y - (I - C)_y (P_i - C)_x > 0$ **then**

  $s_{\text{temp}} \leftarrow 2\pi r - s_{\text{temp}}$

 end if

 if $0 < s_{\text{temp}} \leq s$ **then**

  $s \leftarrow s_{\text{temp}}$

  $P \leftarrow P_i$

 end if

end for

We comment that s is first initialized to largest possible value so that it is always replaced in the loop. The first if-clause makes certain that the arc length we get is always positive, and the second if-clause finds the point to which the (clockwise) arc length is the shortest and eliminates the possibility to erroneously return the initial point as the collision point.

5. Once the point of collision P is obtained, we must calculate the oriented angle θ to obtain full knowledge of the point in the phase space. Simple trigonometric consideration gives us

---

$\theta \leftarrow \arccos\left(\frac{C_y - P_y}{r}\right)$

---

6. The time the particle has advanced is
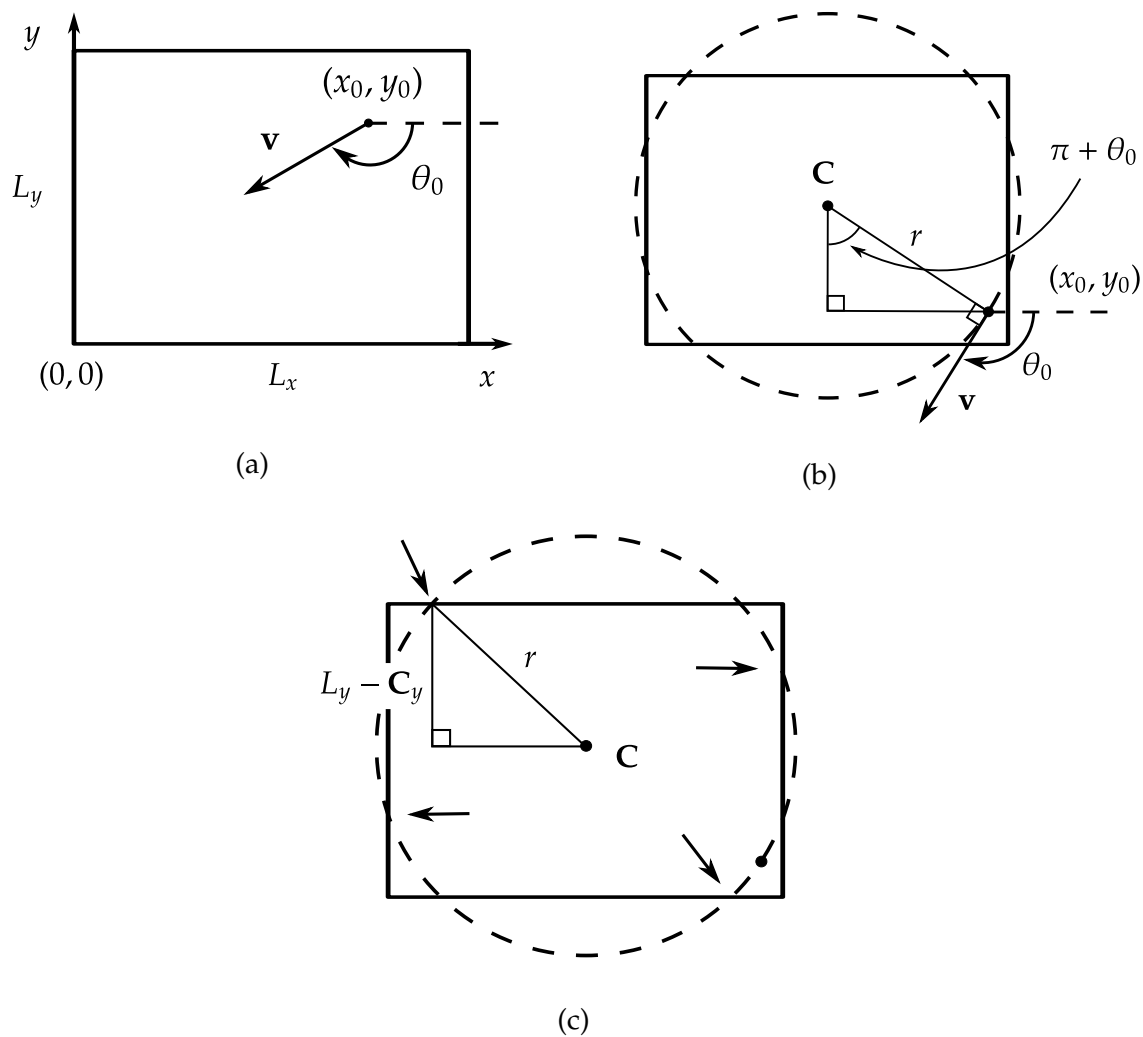

$t \leftarrow s/v$

(a)

(b)

(c)

Figure 45: Schematic figures explaining the steps of the algorithm. In (a) we define the coordinates used by the algorithm. In (b) we demonstrate the geometrical consideration used to calculate the centerpoint C. Finally, in (c) we show the geometry used to calculate the coordinates of one of the crossings of the circle centered at C with the boundary.

7. Finally, the output

Output: $(P_x, P_y, \theta), t$

The entire algorithm is shown on page 108. We note that when implementing the algorithm, one must look out for rounding errors and correct them.

Finally, to check that the algorithm works, we have calculated the Poincaré section of magnetic square billiards of unit length sides with the Larmor radius $r = 0.49$ both with the efficient algorithm in Fig. 46(a) and with molecular dynamics within the velocity Verlet scheme in Fig. 46(b). The Poincaré section is parameterized by the arc length s along one side of the table, e.g., the x-coordinate when colliding with the bottom of the square, and $\cos(\phi)$, cosine of collision angle. As seen from the figures, the calculated Poincaré sections are equivalent, i.e., the efficient algorithm works well.
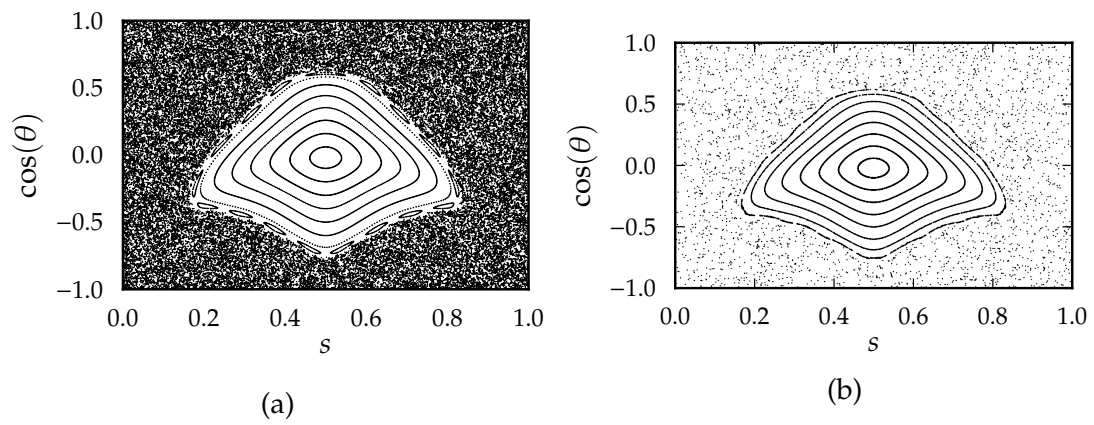
Figure 46: Poincaré sections for magnetic square billiards calculated with (a) the efficient propagation algorithm and (b) molecular dynamics with the velocity Verlet propagation algorithm.

Algorithm 1 Propagation algorithm for magnetic single-particle rectangular billiards

---

Input: I $= (x_0, y_0, \theta_0)$, L_x, L_y, and r

  #Centerpoint:
  $\mathbf{C} = (C_x, C_y) \leftarrow (x_0 + r\sin(\theta_0), y_0 - r\cos(\theta_0))$

  #Calculate all possible points of collision P with the boundary:
  if $|C_x| \leq r$ **then**

     possible_points_of_collision $\xleftarrow{\text{append}} (0, C_y - \sqrt{r^2 - C_x^2})$

  end if
  if $|C_y| \leq r$ **then**

     possible_points_of_collision $\xleftarrow{\text{append}} (C_x + \sqrt{r^2 - C_y^2}, 0)$

  end if
  if $|L_x - C_x| \leq r$ **then**

     possible_points_of_collision $\xleftarrow{\text{append}} (L_x, C_y + \sqrt{r^2 - (L_x - C_x)^2})$

  end if
  if $|L_y - C_y| \leq r$ **then**

     possible_points_of_collision $\xleftarrow{\text{append}} (C_x - \sqrt{r^2 - (L_y - C_y)^2}, L_y)$

  end if

  if possible_points_of_collision is empty **then**
    End program: no collisions
  end if

  #Select the point of collision:
  $s = 2\pi r$
  for $\mathbf{P}_i$ in possible_points_of_collision **do**

    $s_{\text{temp}} \leftarrow r\arccos\left[\frac{(\mathbf{I}-\mathbf{C})\cdot(\mathbf{P}_i-\mathbf{C})^2}{r^2}\right]$
    if $(\mathbf{I} - \mathbf{C})_x(\mathbf{P}_i - \mathbf{C})_y - (\mathbf{I} - \mathbf{C})_y(\mathbf{P}_i - \mathbf{C})_x > 0$ **then**
      $s_{\text{temp}} \leftarrow 2\pi r - s_{\text{temp}}$
    end if
    if $0 < s_{\text{temp}} \leq s$ **then**
      $s \leftarrow s_{\text{temp}}$
      $P \leftarrow P_i$
    end if
  end for

  $\theta \leftarrow \arccos\left(\frac{C_y - P_y}{r}\right)$
  $t \leftarrow s/v$
Output: $(P_x, P_y, \theta), t$

D *Bill2d* – A molecular dynamics approach to billiards

Our program, *Bill2d*, implements a molecular dynamics scheme for the study of chaos in two-dimensional many-body billiards. *Bill2d* is written following the object-oriented paradigm in C++ to offer speed, expandability, and flexibility. The code is modular, i.e., there are several different classes that implement a specific part of the program. This allows for an easy construction of stripped binaries, e.g., for the calculation of statistical properties of the systems. We note that *Bill2d* has been previously used to study, e.g., the dynamics of classical Wigner molecules [87] and two-particle circular billiards [88]; furthermore, *Bill2d* is currently used to study, e.g., the soft Lorentz gas.

The main propagation procedure was already described in Sec. 4.3, but we repeat it here for convenience. This is also illustrated as a flowchart in Fig. 47.

> First, we obtain the initial state of the system in the phase space by either manual user input or by randomly choosing the state. The energy of the initial state is always fixed. The random initial state is chosen by first randomizing the positions of the particles in the energetically allowed part of the configuration space. We then calculate the remaining energy and distribute it evenly among the particles. The directions of the velocities are randomized as well. Distributing the speeds evenly should not affect the results since the velocities are usually mixed shortly after the propagation has been started due to chaotic properties of many-particle billiards.

> Next, we propagate the particles one time-step forward with one of the algorithms described in Sec. 4.2. After each time-step, we check that the particles are inside the billiard table. If some of the particles have crossed the boundary, we (i) save the position, incoming velocity, and the collision angle if we are calculating Poincaré sections and (ii) apply the following scheme to calculate the effect of the collision with the boundary.

> 1. The collision point and the time of the collision are calculated by approximating the trajectory backwards as a straight line in the configuration space. The particle in question is then propagated backwards to the collision point, which corresponds to some time between the actual time-steps.

> 2. The velocity is changed according to the billiard reflection law in Eq. (2.79).

> 3. The particle is propagated with the new velocity linearly to the end of the time-step.

> As we see from the description, we do not use the main integration scheme when handling the boundary collisions. This results in increase in energy in interacting many-particle systems. This is the most promi-

nent approximation in the entire propagation scheme, and therefore, the propagation algorithm, i.e., the velocity Verlet algorithm, is only of second order in our code. Nevertheless, we have found that the method is sufficiently accurate for the purpose of our calculations.

After handling the boundary collisions of each particle, we check if the end criterion, e.g., the maximum simulation time, is fulfilled. If it is fulfilled, the simulation ends; otherwise we continue the propagation.
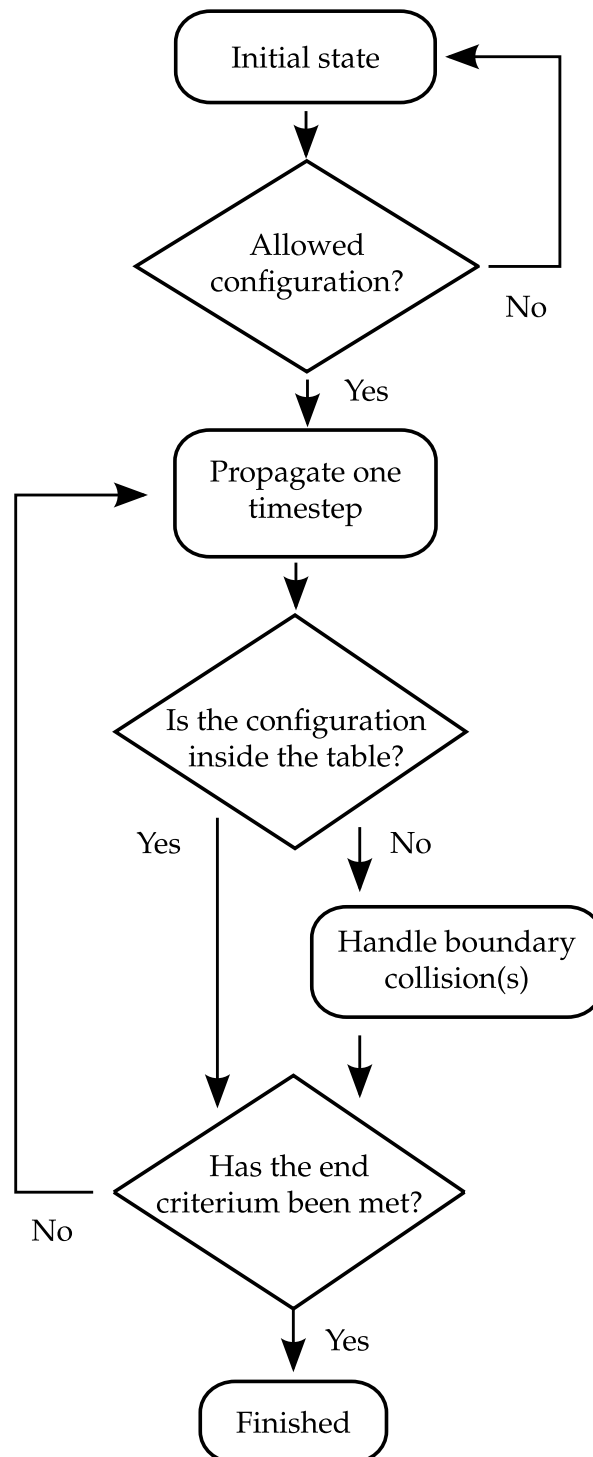

Figure 47: Flowchart of the propagation scheme in the *Bill2d* code

Next, we describe the structure of the actual implementation in detail. The structure is roughly visualized in Fig. 48. Notice that the chart shows both inheritance diagrams and relations of different classes in the same figure.

The user-interface of *Bill2d* has been constructed using the *Boost* C++-libraries to allow the use of both a command line and a configuration file to supply the user input. One can even use them simultaneously, but in case of conflicts between these two, the command-line arguments take precedence. The user-interface is complete, i.e., no recompilation of the program is required when changing systems or parameters. The user-interface is implemented within two classes:

Parser
> **Parser** handles the user-interface and stores the user input into an instance of **ParameterList**.

ParameterList
> **ParameterList** is a container for the user input. It contains *all* the variables needed to specify what to simulate, how to simulate, and what and how to save.

Propagation of the billiard system is implemented within several classes:

Billiard
> This is the base class for the time-evolution process: the propagation algorithm is implemented in Billiard. Classes derived from **Billiard** expand its functionality by replacing the propagation algorithm with ones suitable for magnetic fields (**MagneticBilliard**) and inter-particle interactions (**InteractingBilliards** and **InteractingMagneticBilliards**). Furthermore, **Billiard** class contains all the data buffers, such as trajectories and velocities of the particles.

Table
> **Table** is an interface class that defines how a billiard table should be implemented. It has several children, most through the class **CompoundShape**. **CompoundShape** implements methods to construct billiard tables from elemental structures, such as lines and semi-circles, to allow for easy construction of new tables. Boundary collisions and periodicity are handled by **Table**, which is used by the propagation procedures of **Billiard**.

Potential
> This class implements the interface for potential-particle interactions. Implementing new potentials is easy, and currently we have implemented the harmonic oscillator potential and a soft stadium.

Interaction
> This class implementes the interface for interparticle interactions. Currently, only Coulomb interaction is implemented, but also other interaction types can be implemented with ease.

The class **System** is used to initialize all the classes for the propagation according to the specifications of an instance of **ParameterList**.

During the simulation, *Bill2d* outputs some information, e.g., the simulation time, to the *stdout*-stream. After the simulation, the simulated data is saved to a *HDF5*-file according to user's specifications. The file-output is handled within the **Datafile**-class. One can ask to save trajectories; velocities; Poincaré sections; energies (as a function of time); number of particles (as a function of time); and position-, speed-, and velocity-histograms. The file-output routine is a C++-class that uses the C++-interface of the *HDF5*-library. Finally, the output can be analyzed with several *Python*-scripts that can be used to visualize all the saved data.

Furthermore, *Bill2d* is bundled with *GNU Autotools* to make compilation and installation easy. This means that the standard

```
./configure && make && make install
```

wizardry works. Furthermore, the software is supplemented with a few tests that compare a few simulations to reference data to ensure that the code works as expected.
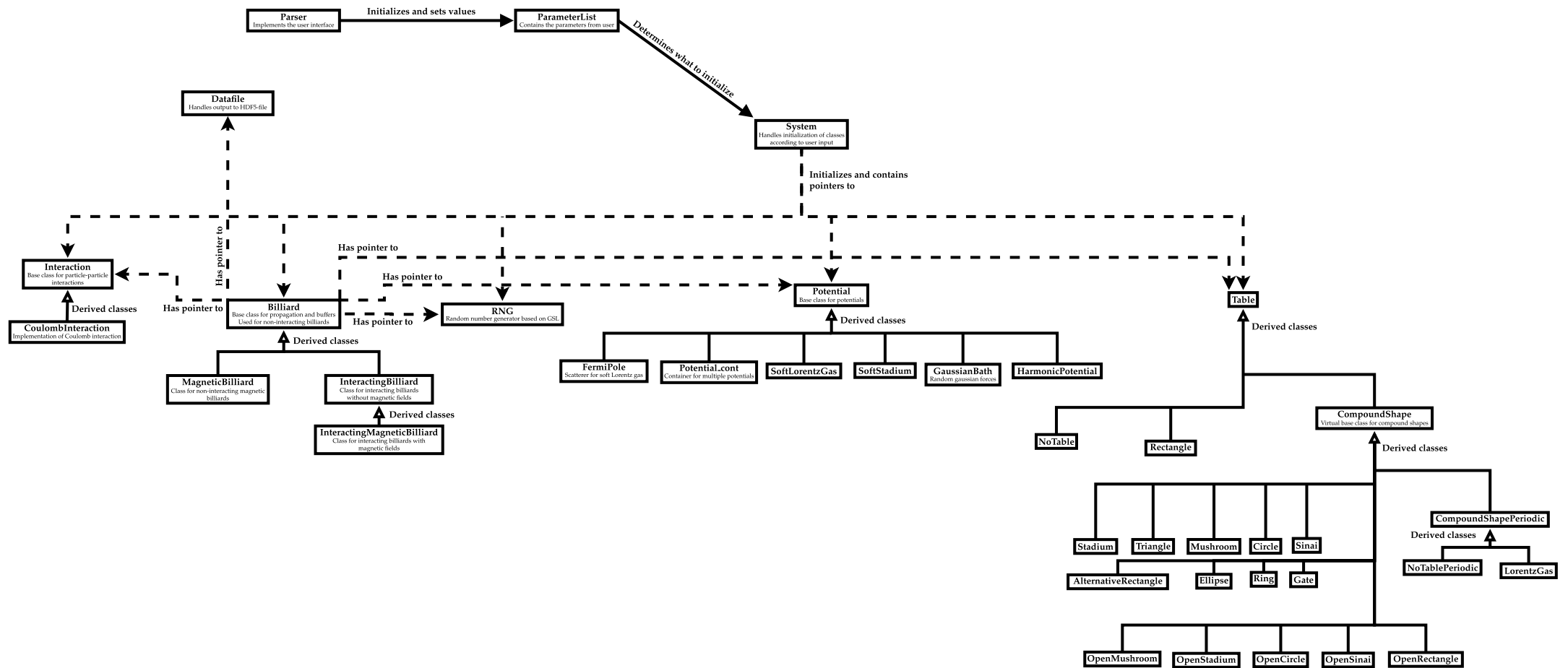
Figure 48: Structure of the *Bill2d* code. The chart shows (i) inheritance diagrams and (ii) relations of different classes.

Coulomb-interacting billiards in circular cavities

J Solanpää[1,2], J Nokelainen[2], P J J Luukko[2] and E Räsänen[1,2]

[1] Department of Physics, Tampere University of Technology, FI-33101 Tampere, Finland
[2] Nanoscience Center, Department of Physics, University of Jyväskylä FI-40014 Jyväskylä, Finland

E-mail: esa.rasanen@tut.fi

Abstract

We apply a molecular dynamics scheme to analyze classically chaotic properties of a two-dimensional circular billiard system containing two Coulomb-interacting electrons. As such, the system resembles a prototype model for a semiconductor quantum dot. The interaction strength is varied from the noninteracting limit with zero potential energy up to the strongly interacting regime where the relative kinetic energy approaches zero. At weak interactions the bouncing maps show jumps between quasi-regular orbits. In the strong-interaction limit we find an analytic expression for the bouncing map. Its validity in the general case is assessed by comparison with our numerical data. To obtain a more quantitative view on the dynamics as the interaction strength is varied, we compute and analyze the escape rates of the system. Apart from very weak or strong interactions, the escape rates show consistently exponential behavior, thus suggesting strongly chaotic dynamics and a phase space without significant sticky regions within the considered time scales.

PACS numbers: 05.45.Pq, 82.40.Bj, 73.21.La

(Some figures may appear in colour only in the online journal)

1. Introduction

Classical billiard systems have attracted continuous interest for several decades due to their applicability to demonstrate chaotic dynamics through (semi)analytic and numerical calculations [1–3]. On the other hand, laboratory experiments on, e.g., microwave billiards [2], quantum dots [3], and even more recently graphene [4] have rapidly extended the interest in chaos across different fields in physics. Along this development, billiard systems have become a key element in the studies of classical and quantum chaos both theoretically and experimentally.

Most billiard studies have focused on *single-particle* properties of systems ranging from regular (integrable) to chaotic (nonintegrable) systems, including also pseudointegrable billiards [5] such as regular billiards with singular scatterers inside the system. Two-particle

billiards have been studied with hard-sphere contact interactions in, e.g., circular [6, 7], rectangular [6, 8] and mushroom-shaped [6] cavities. Also, two-particle billiards with Yukawa interactions have been studied in one-dimensional [9–11] and two-dimensional (2D) systems— including a circular case within both a classical [12, 13] and quantum [14] treatment. The *quantum* circular billiard with two particles has also been studied with Coulomb interactions [15]. However, *classical* studies with Coulomb interactions have been restricted to 2D harmonic oscillators [16–19] including an anharmonic oscillator [20]. Exceptions to this class are periodic systems with focuses on ergodic and topological properties [21] and transport phenomena [22, 23], as well as rectangular billiards in magnetic fields [24] studied with molecular dynamics (MD).

The MD scheme is a computationally efficient approach to many-particle billiards that, in principle, can be extended to large systems without compromising the numerical complexity of the long-range Coulomb interaction. It is noteworthy that the Coulomb interaction is a physically meaningful choice when considering similar systems in, e.g., quantum-dot physics [3, 25, 26]. Experimentally, vertical or lateral semiconductor quantum dots can be tailored at will with respect to the system shape, size, and number of confined electrons. In this respect examination on the interaction effects in few-electron billiards have immediate relevance to physical applications.

Here we adopt the MD approach to analyze the classical chaoticity of a 2D circular hard-wall billiard with two Coulomb-interacting electrons. This particular system is chosen under examination as it represents, alongside a harmonic oscillator, the simplest prototype model for a quantum dot. Secondly, the *noninteracting* properties of the system are well known [1]. We may also expect to find analytic, approximate expressions for the bouncing map in the *strong-interaction limit*. In the intermediate regime, the system is expected to exhibit chaotic behavior. Due to these features the system provides a well-grounded path into examinations of both classical and quantum chaos in Coulomb-interacting billiard systems. We point out that soft billiards are better known in this respect; for example, the two-electron circular harmonic oscillator is regular and becomes mixed (partly regular, partly chaotic) if ellipticity is added in the external potential [19].

We can always introduce an open billiard corresponding to a given closed billiard by generating holes in the boundary via which the particle(s) can escape the table. The escape probability at some infinitesimal time interval (or at a certain number of collisions) is called the *escape rate*. The form of the escape-rate distribution is governed by the structure of the phase space [27] and the position(s) of the hole(s) [28]. If the phase space has sticky regions, i.e., regions where a (possibly chaotic) trajectory gets stuck for a long period of time, the escape rate and survival probability turn out to have an algebraic tail as time tends to infinity [29–35]. On the other hand, if the phase space is fully chaotic and non-sticky, the escape rate is asymptotically exponential. Sticky regions can result from several origins. For example, internal stickiness—not due to Kolmogorov–Arnold–Moser (KAM) tori—can be induced by marginally stable periodic orbits [36, 37]. External stickiness, on the other hand, is caused by sticky KAM tori [29, 38, 39], although not all KAM tori are sticky. Different types of stickiness have recently been reviewed by Bunimovich and Vela-Arevalo in [40].

The paper is organized as follows. In section 2 we briefly introduce the system and our time-propagation scheme. In section 3.1 we show bouncing maps that demonstrate clear signals of chaotic behavior through a large range of the interaction strength. At weak interactions, bouncing maps are found to jump between quasi-regular trajectories. In section 3.2 we analyze in detail the strong-interacting limit and find an approximate expression for the bouncing map. The expression agrees with the numerical results, and at weaker interactions it becomes only approximate. Finally, in section 3.3 we assess the degree of chaoticity by considering escape

rates out of the system. Apart from very weak interactions, we find exponential escape in a wide range of interaction strengths. This indicates strongly uncorrelated trajectories and thus chaotic behavior. The paper is summarized in section 4.

2. System and methodology

We consider two Coulomb-interacting electrons in a circular hard-wall potential. The collisions with the boundary are elastic and the system is described by the Hamiltonian

$$H = \frac{1}{2}(|\mathbf{v}_1|^2 + |\mathbf{v}_2|^2) + \frac{\alpha}{|\mathbf{r}_1 - \mathbf{r}_2|} \tag{1}$$

in Hartree atomic units (a.u.) ($\hbar = e = m_e = (4\pi\epsilon_0)^{-1} = 1$). Here $\mathbf{r}_i$ is the position vector of the ith electron from the center of the system, and α is a parameter that determines the interaction strength. In all our simulations the total energy of the system is fixed to $E = 1$ and the radius of the circle to $R = 1/2$. The interaction strength is restricted to $0 \leqslant \alpha \leqslant 1$, where $\alpha = 0$ corresponds to noninteracting electrons, and $\alpha = 1$ corresponds to electrons localized at opposite sides of the circle with zero motion. We note that all Coulomb-interacting two-particle circular billiards with different length and energy scales can be reduced to our system by a suitable scaling of coordinates $\mathbf{r}' = \gamma\mathbf{r}$, velocities $\mathbf{v}' = \beta^{1/2}\mathbf{v}$, and time $t' = \beta^{-1/2}\gamma t$. The resulting Hamiltonian is similar to that in equation (1) with $\alpha = \beta\gamma$ (for detailed analysis see [41]).

  To propagate the electrons we use MD with the velocity Verlet [42] algorithm which, as a symplectic and time-reversible algorithm is suitable for the study of (possibly chaotic) Hamiltonian systems. A higher order integrator is not necessary for the system under consideration: the numerical uncertainty resulting from a finite time step is dominated by collisions with the boundary instead of the integration of Hamilton's equations of motion. In the velocity Verlet algorithm the positions and velocities of each electron are calculated from

$$\mathbf{r}(t + \Delta t) = \mathbf{r}(t) + \mathbf{v}(t)\Delta t + \tfrac{1}{2}\mathbf{a}(t)\Delta t^2; \tag{2}$$

$$\mathbf{v}(t + \Delta t/2) = \mathbf{v}(t) + \tfrac{1}{2}\mathbf{a}(t)\Delta t; \tag{3}$$

$$\mathbf{a}(t + \Delta t) = \sum_i \mathbf{F}_i[\mathbf{r}(t + \Delta t)]; \tag{4}$$

$$\mathbf{v}(t + \Delta t) = \mathbf{v}(t + \Delta t/2) + \tfrac{1}{2}\mathbf{a}(t + \Delta t)\Delta t. \tag{5}$$

We define $\cos\theta$ and s as the generalized coordinates describing the collisions with the boundary. θ is the angle between the velocity vector of the incoming electron and the tangent of the boundary, so that $\theta < \pi/2$ and $\theta > \pi/2$ correspond to counterclockwise and clockwise traveling directions, respectively. Here $s \in]-\pi/2, \pi/2[$ is the oriented arc length from the chosen origin.

3. Results

3.1. Bouncing maps

In figure 1 we show examples of bouncing maps and electron trajectories for a two-electron circular billiard with different interaction strengths α. In this case the bouncing maps consist of 14 000 ($\alpha = 10^{-5}$) and 5500 ($\alpha = 0.2$ and 0.7) collisions with the boundary. The noninteracting circular system with $\alpha = 0$ is a well-known example of regular billiards [1] represented by straight lines on the map (constant bouncing angle) and straight trajectories forming a
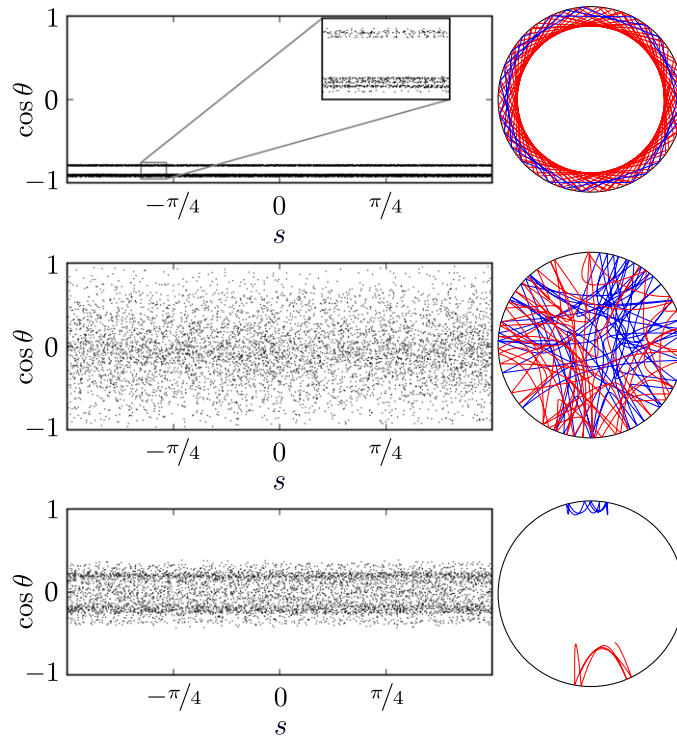
Figure 1. Examples of bouncing maps (of one of the electrons) and trajectories for a two-electron circular billiards with different interaction strengths: $\alpha = 10^{-5}$ (up), $\alpha = 0.2$ (middle), $\alpha = 0.7$ (bottom). Only a small section of the trajectories corresponding to the bouncing maps are shown.

star-shaped pattern, where the inner part of the circle remains empty. When $\alpha = 10^{-5}$ we find emerging deviations from this limit as visualized in the inset of the upper panel of figure 1. When the electrons pass each other the interaction is pronounced and we may find 'jumps' from one quasi-regular trajectory to another one (close-lying parallel lines in the inset).

In the intermediate-interaction range (middle panel of figure 1) the bouncing map shows clear chaotic characteristics. As expected, the distribution of the bouncing map is centered at $\theta = \pi/2$, so that, *on average*, the electrons hit the boundary along the normal vector. If α is increased above $\alpha \sim 0.5$ we find that for some trajectories the maximum of the probability distribution for θ splits into two. This is visible in the bottom panel in figure 1 for $\alpha = 0.7$. The splitting is due to the fact that the particles are bouncing on the *opposite sides* of the circle (in a collective circulating motion), so that the dominant collision angles (for a large class of trajectories) are $\pi/2 \pm \delta$, where δ is a small deviation. However, the splitting is smoothed out when a large ensemble of trajectories is taken into account. When α is increased further, the system gradually becomes (quasi)regular and eventually the bouncing map reduces into a one-dimensional curve. In the following we carry out analytic calculations in the strong-interaction limit.

3.2. Strong-interaction limit

In the strong-interaction limit $\alpha \to 1$, the two-electron dynamics shows regular characteristics. The electrons are confined at opposite sides of the circle as visualized in figure 2. Here we
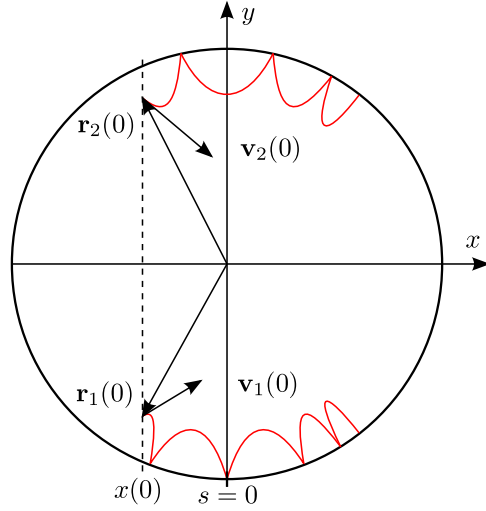
Figure 2. Two electrons oscillating at the opposite sides of the circle when the interaction is strong ($\alpha \gtrsim 0.9$). The initial positions and velocities are shown.

focus on the special case with total angular momentum $L = 0$ which is conserved due to the rotational symmetry. Hence, according to the choice of coordinate axes in figure 2 we may approximate $x \equiv r_{1,x} \approx r_{2,x}$. We point out, however, that the y coordinate does not usually have mirror-symmetry. Note also the position of $s = 0$ at $x = 0$ in figure 2, so that $s \in [-s_{\max}, s_{\max}]$.

As the second approximation, the electron velocity perpendicular to the edge when a collision takes place, $v_\perp$, can be taken as a constant, i.e., it is approximately the same for all possible values of s at all times. After a straightforward geometrical analysis, taking into account the conservation of E and L, we can calculate $v_\perp$ and also $v_\parallel(s)$, the tangential velocity during the collision. Finally by using $\cos\theta = v_\parallel / \sqrt{v_\perp^2 + v_\parallel^2}$ we obtain the following strong-interaction approximation for the bouncing map of electron 1:

$$\cos\theta_1(s) = \pm \left(1 + \frac{2K + 2U_0 - 2U_a - L^2/R^2}{U_b - U_c(s) + L^2/R^2} \right)^{-1/2}, \tag{6}$$

where $K = [v_{1,x}^2(0) + v_{1,y}^2(0)]/2$ is the initial kinetic energy of the electron, $L = x(0)v_{1,y}(0) - y_1(0)v_{1,x}(0)$ is its initial angular momentum (note that $x = x_1 \approx x_2$ according to our approximation above), $U_0 = \alpha/[|y_1(0)| + |y_2(0)|]$ is the initial potential energy, and $R = 1/2$ is the radius of the circle. Furthermore, equation (6) has three potential energy components that have the expressions

$$U_a = \frac{\alpha}{|y_2(0)| + \sqrt{R^2 - x(0)^2}}, \tag{7}$$

$$U_b = \frac{\alpha}{2\sqrt{R^2 - x(0)^2}}, \tag{8}$$

$$U_c(s) = \frac{\alpha}{2R\cos(s/R)}. \tag{9}$$

They correspond to the following situations where both E and L are conserved and $x_1 = x_2$. Firstly, U_a is the potential energy corresponding to a situation where electron 1 touches the boundary at $t = 0$ and electron 2 has its initial position and velocity. Secondly, U_b corresponds
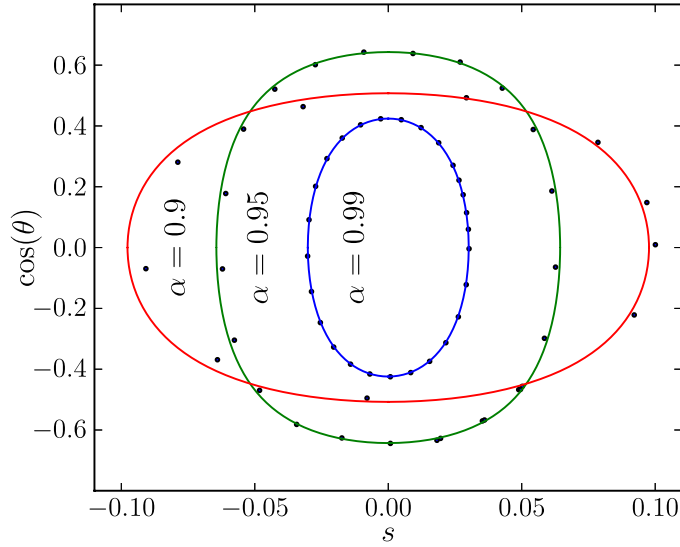
5

Figure 3. Analytic result for the large-α limit (equation (6)) of the bouncing map (solid lines) for $\alpha = 0.99$, 0.95, and 0.9. The corresponding simulated, i.e., numerically exact values are shown by points.

to a situation where both electrons touch the boundary at $t = 0$, and v_1 is the same as in the previous (first) case. Finally, U_c corresponds to a situation where both electrons touch the boundary at s at unknown time, having the same $v_\perp$ as in the previous (second) case. We point out that an alternative approximate formula for the full phase-space trajectory can be obtained by using polar coordinates (within certain approximations) and by assuming a constant Coulomb force. This simpler analytic scheme—explained in detail in [41]—leads to a reasonable *temporal* agreement for several bounces at $\alpha \geqslant 0.99$.

Figure 3 shows the results from equation (6) for $\alpha = 0.99$, 0.95, and 0.9 (solid lines). The *simulated*, i.e., the numerically exact values, are shown by points for comparison. As α is decreased we find gradual deviation from the simulated data. At $\alpha = 0.9$ the deviation is already clearly visible. We may thus state that equation (6) provides a reasonable approximation for the bouncing map at $\alpha \gtrsim 0.9$. This threshold slightly depends on the initial conditions; the examples in figure 3 are chosen such that the deviations between the analytic expression and the numerical data are relatively large. However, we point out that for longer times the deviations between the applied strong-α approximation and the electron–electron interaction effects will increase. As a result, we may expect that in large time scales the simulated points in figure 2 will form a curve of a finite width.

3.3. Escape rates

Next we examine how the dynamics of the system changes as we move from the noninteracting ($\alpha = 0$) to the strongly interacting ($\alpha \to 1$) limit. A full description of the seven-dimensional phase space, for example by means of a Poincaré section, would be difficult. Therefore, we consider escape rates of the system by placing holes in the boundary. As already discussed in the introduction, systems with sticky regions in phase space have power-law asymptotics of the escape-rate distribution, whereas in fully chaotic systems without stickiness the escape-rate distribution is exponential as $t \to \infty$. We remind the reader that escape rates are commonly
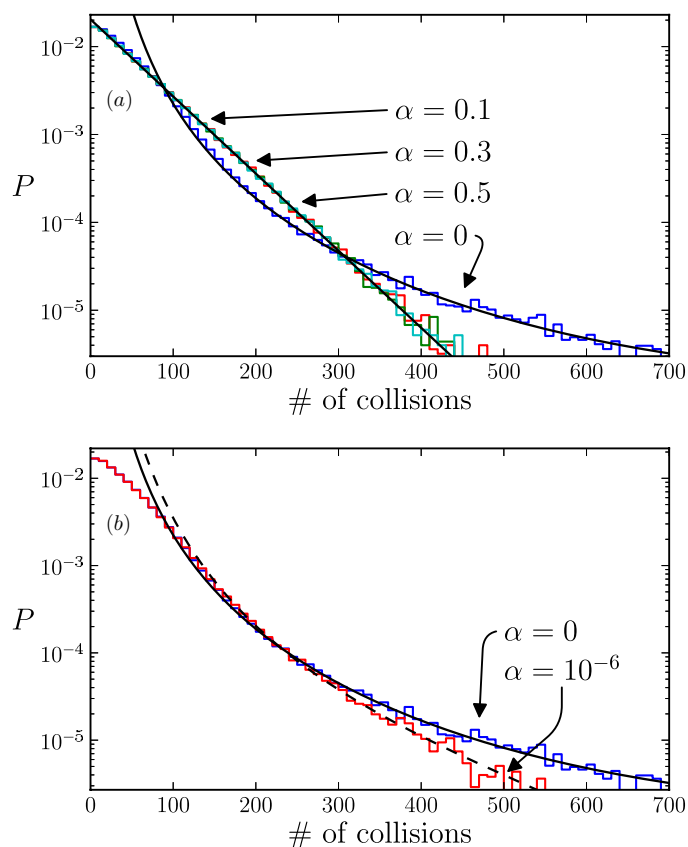
Figure 4. (*a*) Histograms of the escape rates in a two-electron circular billiard. The noninteracting case shows power-law behavior in the tail (curved solid line), whereas at $0.1 \leqslant \alpha \leqslant 0.5$ the escape rate is exponential (straight solid line). (*b*) At very weak interactions $\alpha = 10^{-6}$ we find a mixture of these tendencies due to quasi-regular trajectories in the system.

governed by stickiness rather than regular/chaotic components of the phase space. Therefore, we cannot make a complete assessment of the structure of the phase space, especially not close to the limits $\alpha = 0$ and $\alpha \rightarrow 1$.

We set ten holes in the boundary covering together 1/50 of the boundary length—the same fraction as in [43]. The escape rates are considered as a function of the total number of collisions n, i.e., the sum of collisions of both particles, rather than the propagation time, since the characteristic time scale strongly depends on the interaction strength α. For each α we compute $2.5 \ldots 6 \times 10^5$ respective trajectories with random initial conditions and store the number of boundary collisions before the escape. Initial conditions are randomized in the following way. First we pick random initial conditions for the particles in the energetically allowed ($E_{\text{total}} = 1$) part of the configuration space. The remaining energy is then evenly distributed as a kinetic energy for the particles. The directions of the initial velocity vectors are randomized. The escape rate $P(n)$ is defined as the ratio between the number of trajectories escaping at the nth collision and the number of trajectories in the initial ensemble. Presenting the escape rate as a function of the number of collisions instead of time might change the form of the escape-rate distribution [44]. In our case, however, we have numerically checked that the form of the escape-rate distribution is the same in both cases. The time steps are chosen

in the range $\Delta t = 10^{-8} \ldots 10^{-7}$, so that the convergence is ensured in every calculation, while the numerical efficiency is maximized.

Figure 4(*a*) shows the resulting histograms of the escape-rate calculations. First, the noninteracting situation ($\alpha = 0$) has a clear power-law tail with $P(n) \propto n^{-\gamma} + \text{const}$, where $\gamma \approx 3.46$. In contrast, when $0.1 \leqslant \alpha \leqslant 0.5$ an excellent fit to the exponential behavior with $P(n) = 49^{n-1}/50^n$ (straight line) can be found. This relation results from the system geometry: each collision has an escape probability of $1/50$, and thus for the nth collision to lead to escape we find $P(n) = (49/50)^{n-1}(1/50)$. This essentially means that the correlation with two successive bounces is completely lost, and hence the system can be classified as chaotic.

In figure 4(*b*) we take a closer look at the weak-interaction limit with $\alpha = 10^{-6}$. A good fit to the computed data is obtained with a power-law curve having $\gamma \approx 4.08$, i.e., the escape is slightly faster than in the noninteracting limit. However, at small time scales the behavior is very similar to $\alpha = 0$ as the trajectories essentially follow the same (quasi-)regular patterns. These quasi-stable trajectories also give rise to a power-law tail in the escape-rate distributions for weak interactions. However, the interaction reduces the lengths of the quasi-regular parts of the electron trajectories and thus decreases the survival probability (and escape rates) at longer time scales.

In conclusion, our results on the escape probabilities show that the transition to exponential escape rates is (i) smooth (not abrupt as a function of α), (ii) occurs first at large times (large number of collisions) in the histogram, and (iii) generally appears at relatively small values for α. Our tests indicate that at $\alpha \sim 10^{-3}$ the most part of the calculated escape-rate histogram is closer to an exponential behavior than to the power-law one. We point out that these numerical experiments do not exclude the possibility of power-law escape rates with intermediate interaction strengths as n tends to infinity. Also, the large-α regime is excluded in this analysis due to numerical reasons: at $\alpha > 0.5$ we would need to decrease the size of the holes due to small-scale motion close to the boundary, and thus the time step should also be decreased. Hence, for the consistency of results we have focused here only on the range $0 \leqslant \alpha \leqslant 0.5$.

4. Summary

To summarize, we have looked thoroughly at the chaotic dynamics of circular billiards containing two Coulomb-interacting electrons with the full range of interaction strengths ($0 \leqslant \alpha \leqslant 1$). Close to both weak- and strong-interaction limits the bouncing maps show traces of quasi-regular behavior, although the dynamics generally appears as chaotic. In the strong-interaction limit we are able to find an analytic expression for the bouncing map that agrees very well with the calculated data at $\alpha \to 1$. At smaller α the predictive power of the expression reduces, although the agreement is reasonable down to $\alpha \sim 0.9$. To assess the change in dynamics as the interaction is increased we have calculated the escape rates as a function of α and found similar exponential behavior through a wide range of interaction strengths. Thus, within the examined time scales our results suggest universally chaotic behavior in Coulomb-interacting hard-wall billiards apart from the noninteracting and possibly strong-interacting limits.

Acknowledgments

References

[1] Gutzwiller M C 1990 *Chaos in Classical and Quantum Mechanics* (New York: Springer)
[2] Stöckmann H-J 1999 *Quantum Chaos: An Introduction* (Cambridge: Cambridge University Press)
[3] Nakamura K and Harayama T 2004 *Quantum Chaos and Quantum Dots* (Oxford: Oxford University Press)
[4] Miao F, Wijeratne S, Zhang Y, Coskun U C, Bao W and Lau C N 2007 *Science* **317** 1530
[5] Cheon T and Cohen T D 1989 *Phys. Rev. Lett.* **62** 2769
[6] Lansel S, Porter M A and Bunimovich L A 2006 *Chaos* **16** 013129
[7] Ranković S and Porter M A 2013 *Chaos* **23** 013123
[8] Awazu A 2001 *Phys. Rev.* E **63** 032102
[9] Manchein C and Beims M W 2007 *Chaos Solitons Fractals* **39** 2041
[10] Oliveira H A, Manchein C and Beims M W 2008 *Phys. Rev.* E **78** 046208
[11] Meza-Montes L and Ulloa S E 1997 *Phys. Rev.* E **55** R6319
[12] Toporowicz L A and Beims M W 2006 *Physica* A **371** 5
[13] Beims M W, Manchein C and Rost J M 2007 *Phys. Rev.* E **76** 056203
[14] Xavier E P S, Santos M C, Dias da Silva L G G V, da Luz M G E and Beims M W 2004 *Physica* A **342** 377
[15] Sawada S, Terai A and Nakamura K 2009 *Chaos Solitons Fractals* **40** 862
[16] Nazmitdinov R G, Simonovic N S and Rost J-M 2002 *Phys. Rev.* B **65** 155307
[17] Radionov S, Åberg S and Guhr T 2004 *Phys. Rev.* E **70** 036207
[18] Drouvelis P S, Schmelcher P and Diakonos F K 2003 *Europhys. Lett.* **64** 232
[19] Drouvelis P S, Schmelcher P and Diakonos F K 2004 *Phys. Rev.* B **69** 035333
[20] Schröter S, Hervieux P-A, Manfredi G, Eiglsperger J and Madroñero J 2013 *Phys. Rev.* B **87** 155413
[21] Knauf A 1987 *Commun. Math. Phys.* **110** 89
[22] Liebchen B, Diakonos F K and Schmelcher P 2012 *New J. Phys.* **14** 103032
[23] Denisov S I, Denisova E S and Hänggi Peter 2005 *Phys. Rev.* E **71** 016104
[24] Aichinger M, Janecek S and Räsänen E 2010 *Phys. Rev.* E **81** 016703
[25] Kouwenhoven L P, Austing D G and Tarucha S 2001 *Rep. Prog. Phys.* **64** 701
[26] Reimann S M and Manninen M 2002 *Rev. Mod. Phys.* **74** 1283
[27] Zaslavsky G M 2005 *Hamiltonian Chaos and Fractional Dynamics* (Oxford: Oxford University Press)
[28] Bunimovich L A and Yurchenko A 2011 *Isr. J. Math.* **182** 229
[29] Chirikov B V and Shepelyansky D L 1984 *Physica* D **13** 395
[30] Hillermeier C F, Blümel R and Smilansky U 1992 *Phys. Rev.* A **45** 3486
[31] Karney C F F 1983 *Physica* D **8** 360
[32] Meiss J D and Ott E 1985 *Phys. Rev. Lett.* **55** 2741
[33] Meiss J D and Ott E 1986 *Physica* D **20** 387
[34] Hanson J D, Cary J R and Meiss J D 1985 *J. Stat. Phys.* **39** 327
[35] Fendrik A J, Rivas A M F and Sánchez M J 1994 *Phys. Rev.* E **50** 1948
[36] Alt H, Gräf H-D, Harney H L, Hofferbert R, Rehfeld H, Richter A and Schardt P 1996 *Phys. Rev.* E **53** 2217
[37] Altmann E G, Friedrich T, Motter A E, Kantz H and Richter A 2008 *Phys. Rev.* E **77** 016205
[38] Karney C F F 1983 *Physica* D **8** 360
[39] Altmann E G, Motter A E and Kantz H 2006 *Phys. Rev.* E **73** 026207
[40] Bunimovich L A and Vela-Arevalo L V 2012 *Chaos* **22** 026103
[41] Solanpää J 2013 *Master's Thesis* University of Jyväskylä
[42] Allen M P and Tildesley D J 1987 *Computer Simulation of Liquids* (Oxford: Oxford University Press)
[43] Bauer W and Bertsch G F 1990 *Phys. Rev. Lett.* **65** 2213
[44] Kaufmann Z and Lustfeld H 2001 *Phys. Rev.* E **64** 055206